Development of beam diagnostics and studies of transverse beam dynamics towards high-intensity operations in the beamlines of the C70XP cyclotron at ARRONAX

Atul Sengar

DOCTORAT MATIERE BRETAGNE MOLECULES LOIRE ET MATERIAUX

UNIVERSITÉ DE NANTES

THESE DE DOCTORAT DE

L'UNIVERSITE DE NANTES

ECOLE DOCTORALE N° 596
Matière, Molécules, Matériaux
Spécialité : *Physique des Particules et Accélérateur*

Par

Sengar Atul

Development of beam diagnostics and studies of transverse beam dynamics towards high-intensity operations in the beamlines of the C70XP cyclotron at ARRONAX.

Thèse présentée et soutenue à Nantes, 30/03/2021
Unité de recherche : Laboratoire SUBATECH UMR 6457

Rapporteurs avant soutenance :

Delerue Nicolas	Chargé de Recherche, Université Paris-Sud
Gilles Ban	Professeur, Laboratoire Physique Corpusculaire de CAEN (LPC, Caen)

Composition du Jury :

Président :		
Examinateurs :	Delerue Nicolas	Chargé de Recherche, Université Paris-Sud
	Gilles Ban	Professeur, Laboratoire Physique Corpusculaire de CAEN
Dir. de thèse :	Haddad Ferid	Professeur, Université de Nantes, Subatech, GIP ARRONAX
Co-dir. de thèse :	Poirier Freddy	Ingénieur de Recherche / CNRS, GIPARRONAX

ACKNOWLEDGEMENTS

Throughout the writing of this dissertation, I have received a great deal of support and assistance.

I would first like to express my deepest gratitude to my guide, Dr. Freddy Poirier his valuable guidance, consistent engagement, personal caring, timely help and providing me with an excellent atmosphere for doing research. All through the work, in spite of his busy schedule, he has extended cheerful and cordial support to me for completing this research work. Your expertise was invaluable in formulating the research questions and methodology. Your insightful feedback pushed me to sharpen my thinking and brought my work to a higher level.

I would like to thank my thesis director, Dr. Ferid Haddad who always supported me for taking the essential technical courses. This not only enhanced my knowledge but also, helped me to think broader on the subject of my thesis. Your support allowed me to show my work in the international conferences and also, got chance to interact with highly experienced professionals in this field.

I would also like to thank my external guides, Dr. Delerue Nicolas and Dr. Cussooneau jean-pierre whose yearly feedback on my work helped me to understand where I should focus more in the following year.

I would also like to thank my colleagues from my office. Charbel Koumeir who helped me during my experimental work with low intensity beamline. Arnaud Cadiou who gave me geometrical information of few instruments. Teddy Durant who taught me the concept of 'makefile' for faster quadrupole scans in the simulations. Xavier Goiziou and Francois Bulteau who helped in the BLM's electrical work. A special thanks to GAMO for operating the beam during my various experimients.

I would also like to thank my colleagues from iThemba labs, Garrett, William, Amien, Justin and Dr. Lowry who assisted me in all means during my stay and BPM work carried out in South Africa.

I would like to acknowledge thesis funding agencies. This work has been, in part, supported by a grant from the French National Agency for Research called "Investissements d'Avenir", Equipex ARRONAX-Plus noANR-11-EQPX-0004 and Labex IRON noANR-11-LABX-18-01. This work has been supported in part by a PhD scholarship from the Institute of Nuclear and Particle Physics (IN2P3) from the National Scientific Research center (CNRS) and the Regional Council of Pays de la Loire, France.

In addition, I would like to thank my parents and girlfriend for their cooperation and understanding my busy schedule. Due to their support, I was always at mental peace and focused in my work. Last but not the least, thanks to my friends who reminded me how social I was which I almost forgot at some point of time during PHD.

Atul Sengar

Contents

List of Tables

List of Figures

Chapter 1

INTRODUCTION

A large number of accelerators in the domain of medical application or medical related research have started operation since 2010. This number will increase in the next five years with, for example, more than 50 accelerators are planned for radiotherapy usage (as of November 2020, PTCOG 20 [1]).

A similar trend, at a smaller scale, is observed for commercial accelerators delivering protons with expected maximum beam power above 10 kW. The "conference Cyclotron and Applications 2019" [2, 3] is giving several examples of these type of machines. With such capacity, these accelerators are mostly foreseen for production of new radioisotopes with sufficient quantities for usage in medical research or delivery to hospital for cancer imaging or therapy.

The cyclotron at the ARRONAX Public Interest Group (GIP) embodies this trend, being the first, fully commercial cyclotron to run at 70 MeV with a power capacity above 50 kW. It has been designed subsequently to the experience of previous 30 MeV cyclotrons built by the company IBA (Ion Beam Applications) and in consideration of the development to be adapted for this machine. It resulted in the commissioning in 2010 of two 70 MeV proton beams, each at 375 µA for 24 h on beam dumps. By so, in regard of the power, the cyclotron C70XP "cyclone", is regarded as a high intensity high energy cyclotron for radioisotope production. The acronym ARRONAX stems from the facility usage, meaning "Accelerator for Research in Radiochimistry and Oncology in Nantes Atlantique", indicating the main initial goal of the GIP. In practice, this translates in production of radioisotopes and activities on research for radiobiology, radiochemistry, and contribution to medical and basic physics research.

For irradiation of targets pertaining production of radioisotopes, the intensity has been, since the commissioning, increased to reach a beam intensity of 150 µA at the end of the beamlines in 2017. This intensity increase holds for the future: it is part of a continuous goal for the beam, as it enables radioisotopes to be potentially produced in more quantity within a specific time scale. Beyond the suitability of the targets regarding the delivered power, this goal can be pursued taking into account that a maximum of high energy (70 MeV) particles can be

transported appropriately to the target. For examples, particle losses have to be kept relatively low or controlled in dedicated area, and beam dimensions and position have to be adequate for the beamlines and the target at the same time.

With the increase of intensity and irradiation over several days, operation configuration (mis-steering, large envelop at sensitive location, in-adapted emittance, etc) affects significantly the transport of particles and thus several locations along the beam path can pile up portion of the beam leading to activation or potential damages. An example of a particularly sensitive location, is the rubber-based sealing that is used at the junction of beamlines upstream the quadrupoles and close to the wall of the vaults. These can not be exchanged without deposition of the entire beamlines and reposition of the quadrupoles. Manipulation that would impact drastically the operation schedule of the machine. Another example is the activation of the beam pipes close to the maximum transverse beam dimension at the quadrupole location. Additionally at the target location, the knowledge of the focusing transverse dimension of the beam can help safer target irradiation (high-density energy deposit and consequently accentuating possible damages to the targets). Part of these effects can be mitigated by applying a strategy based on the following approaches: comprehension of the beam, diagnostics and protection . As an example of the last approach, for the beamlines at ARRONAX, carbon rings have been installed to protect sensitive locations such as the one described above. Thus, there is a clear need for beam diagnostics like beam loss monitor (BLM) to safeguard sensitive locations and beam characteristics studies to improve the overall performance of the machine.

In the present thesis, to pursue the strategy on the comprehension of the beam, transverse beam dynamics studies have been applied for the transport of particles in the beamlines, including the effect of operational tuning that have a major impact on the beam. Also for this strategy diagnostics have been devised: the priority goals of these latter are both to tackle potential particle losses measurements with diagnostics such as Beam Loss Monitors (BLM) and to contribute to the effort on future apparatus usage to steer the beam with the development of Beam Position Monitors (BPM) in collaboration with iThemba Labs. By conception, these diagnostics can be scaled up for use on similar high-intensity beamlines.

The beam dynamics studies are used to study several transverse beam characteristics. One of the objectives of these studies is to optimize the beam size according to the acceptance criteria and minimization of the beam losses in the high-intensity beamlines. It is also essential

to understand the beam loss mechanism and the procedure to minimize beam losses. Some experiments and simulation work have been performed prior to the studies in this thesis. These studies indicated few operational parameter dependencies such as stripper foil azimuth setting to improve beam alignment in the beamlines. These studies also indicated a change in the beam quality parameter called transverse beam emittance over time by a factor of 4 where theoretical model-dependent studies were implemented. But in all these studies, there was a need of better explanation from the physics point of view.

In this context, this thesis is devoted to the experimental and theoretical studies of transverse beam dynamics for the high-intensity beamlines of ARRONAX C70 cyclotron. This also includes the development of new beam diagnostics such as BLM and BPM which provide extra tools for beamline tuning to the operators. These studies provide insight for transverse beam dynamics studies of such machines.

This thesis is organized as follows. The chapter 2 is a bibliographic summary of theoretical background on the work performed and presented here. In section 2.1, the beam transport scheme is briefly described from the ion sources to the beam extraction system. Section 2.2 includes the theoretical background on transverse beam dynamics related to the studies performed in this thesis. Section 2.3 describes the theoretical framework of beam loss monitors (BLM) and types of BLMs in use at various accelerator facilities.

The chapter 3 describes the global setup of the experiments, the simulation tools, data acquisition and monitoring system at ARRONAX. Here, low and high-intensity beamlines at ARRONAX cyclotron are briefly discussed. This chapter also talks about the instrumentation for experimental data analysis and methodology widely used in the experiments. The purpose of this chapter is to outline general working and experimental environment at ARRONAX.

Chapter 4, 5, and 6 exposes all the results obtained during this work. Chapter 4 is discussing the experimental work performed and results obtained on the BLMs. The installation of the BLMs in high-intensity beamline and its response during operations are also described. Chapter 5 is discussing the experimental and theoretical work to study the transverse beam dynamics of high-intensity beamlines. Chapter 6 is exposing the results of the new BPM prototype (based on the principle of RF coupling) calibration work performed at iThemba Labs, South Africa. This BPM is foreseen to be tested with the proton beam and is planned to be installed on ARRONAX beamlines.

Chapter 2

CONTEXT

ARRONAX [4] is a multi-particle high-energy high-intensity industrial accelerator (see figure 2.1) and here studies are based on a 70 MeV proton beam alone. Industrial accelerators [5], by construction rely on a few limited numbers of standard diagnostics [6] to perform their duties and generally, this limitation does not cover precisely the knowledge of the beam hitting the target after various upstream events. This is a constraint for the facility's capacity in making the desired beam characteristics but also to deal with new necessary beam developments. The ARRONAX machine, a high power industrial accelerator, faces both these limitations (desired beam characteristics and new necessary beam developments) in terms of diagnostics and in regards to its present and future use for applications. Depending on the applications, the duration of operation can be from a few seconds to several days and some of the applications ask for a fixed beam envelope while other applications require precise beam characteristics. The facility runs throughout the year and it necessitates stable and regular operation. The intention of the facility for the future usage of the machine is to go beyond the present operation and expertise.

In order to support present operation, the transition towards higher intensities, and prepare developments of beamlines and experiments, it is essential to study beam characteristics. Indeed, Beam which hits the target is deeply affected by upstream beamline elements like a dipole, steering, quadrupoles, etc. The impact of all these events on the beam have been studied here to improve beam dynamics in high-intensity beamlines. Development of new instrumentation such as Beam loss monitor (BLM) for high-intensity beamline has also been studied and implemented.

In this context, we will discuss the theoretical framework of the work presented in this thesis. At first, we introduce the C70XP (XP is the acronym used for multi-particle) cyclotron and ARRONAX activities. Also, the theoretical background on transverse beam dynamics and beam loss monitors which are in the scope of the work presented in this thesis will be discussed briefly.

2.1 ARRONAX C70 Cyclotron

2.1.1 Introduction

ARRONAX C70 cyclotron can be classified as a high-power, high-energy and high-intensity cyclotron for proton beam. ARRONAX is well positioned among high power cyclotron around the globe as highlighted in figure 2.1 in green color. The X and Y axis are showing the energy of the proton beam (MeV) and average integrated intensity (µA), respectively. As one can see, the majority of existing machines are below 10 KW power (black line) and a few machines are above this limit including ARRONAX machine.

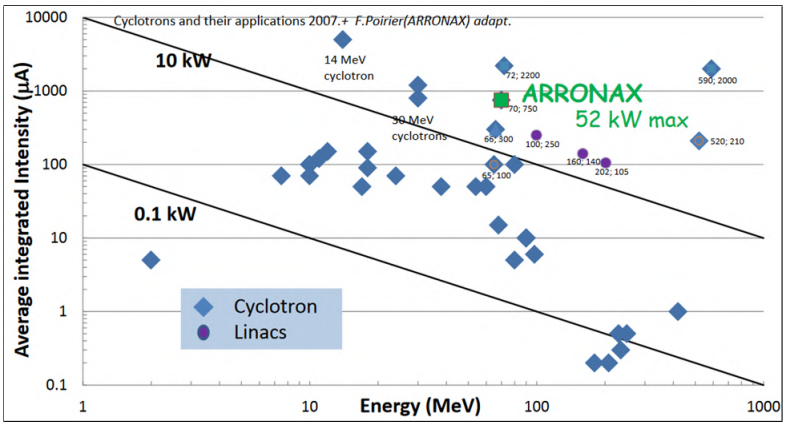

Figure 2.1: ARRONAX C70 cyclotron among high energy and high intensity accelerators around the globe [88].

The C70 cyclotron at ARRONAX is designed and constructed by IBA. It can accelerate particles H^-, D^-, HH^+ and He^{2+}. The positively charged ions (HH^+ and He^{2+}) can be extracted by an electrostatic deflector (ESD) and negatively charged ions (H^- and D^-) with a stripper foil. The extraction energy for H^- and D^- can be varied from 30-70 MeV and 15-35 MeV, respectively. The extraction energy for HH^+ and He^{2+} is 35 MeV and 70 MeV, respectively. The main characteristics of the C70 cyclotron are listed in Table 2.1.

Accelerated Beam	Extracted Beam	Extracted Energy (MeV)	Beam Intensity ($e\mu A$)
H^-	H^+	30-70	375
D^-	D^+	15-35	50
He^{2+}	He^{2+}	70	70
HH^+	HH^+	35	50

Table 2.1: Characteristics of ARRONAX C70 cyclotron [7]

The cyclotron is equipped with two external ion sources, an electron cyclotron resonance

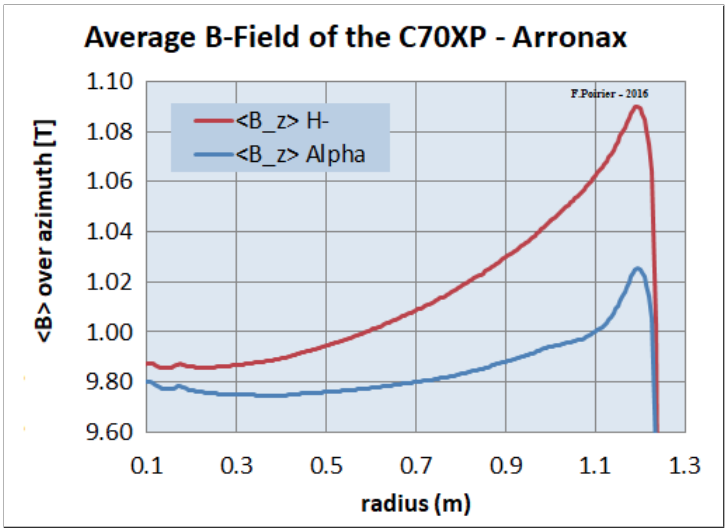

Figure 2.2: Average magnetic field in the C70 cyclotron for H^- and Alpha particles [4].

(ECR) [9] for positive ions and a multi-cusp ion source [10] for negative ions. The ion sources are mounted on the source bench which include the injection line. An axial injection system is installed in the central region to deliver the beam into the cyclotron dees using a spiral inflector. The cyclotron is at a fixed frequency and fixed electromagnetic field for a single type of ion (see figure 2.2). After acceleration, the beam is extracted and sent to any of the 6 available Vaults (see figure 2.3).

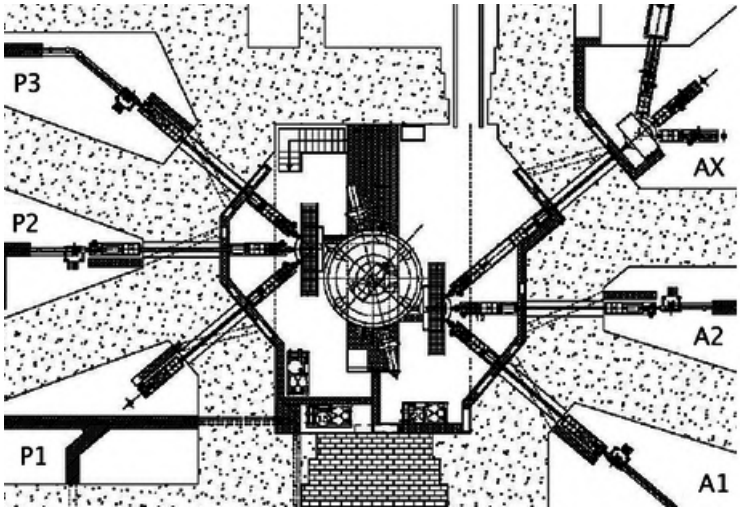

Figure 2.3: ARRONAX C70 cyclotron schematic diagram [7].

Five vaults each has a single end-station which is used for radioisotope production and one vault has three end-stations which is used for detector development and radiobiological experiments. Radio-isotope production beamlines are high-intensity (100's of μA) and another one is low-intensity beam current line (AX).

2.1.2 ARRONAX activities

ARRONAX means "Accelerator for Research in Radiochemistry and Oncology in Nantes Atlantique". ARRONAX is legally a Public Interest Grouping which means it is a group of several public members, established by convention, approved by the State. The members of GIP ARRONAX are the MSRI, the Pays de la Loire Region, national research organizations (CNRS and INSERM), higher education institutions (Nantes University and IMT Atlantique), and hospitals (ICO and CHU Nantes). The members are brought together in a General Assembly which elects its president and vice president. ARRONAX facility is mainly dedicated to the production of radioisotopes for medicine both for diagnostic purposes (Positron-emission tomography - PET and single photon emission tomography - SPECT) and for therapeutic applications (internal radiotherapy). Other activities at ARRONAX include research in radiochemistry, radiobiology and nuclear physics.

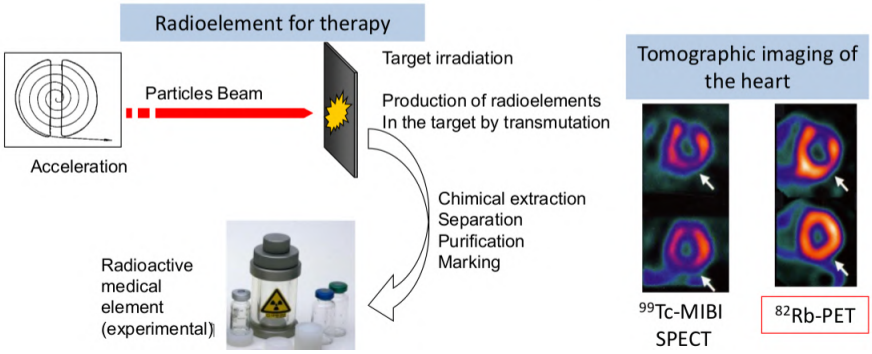

Figure 2.4: The example of radionuclide production and activities at GIPARRONAX.

A list of priorities (radionuclide production) has been established in close collaboration with the International Scientific Council, which has followed ARRONAX's activities since inception. ARRONAX produce radioisotopes for PET (ex: ^{82}Sr, ^{44}Sc, ^{64}Cu) and targeted for radio therapy (ex: ^{211}At, ^{67}Cu, ^{47}Sc). The detailed description is summarized in table 2.2.

Radio-isotope	Target	Nuclear reaction	Reaction cross-section ($mbarns$)	Beam energy required (MeV)	Required beam intensities (µAe)
^{82}Sr	^{nat}Rb	$^{nat}Rb(p,xn)$	≈ 100	70	>130
^{211}At	^{nat}Bi	$^{nat}Bi(a,2n)$		28	>15
^{64}Cu	^{64}Ni	$^{64}Ni(d,2n)$	≈ 675	16	around 80
^{44}Sc	$^{44}CaCO_3$	$^{44}Ca(d,2n)$		16	
^{68}Ge	^{nat}Ga	$^{69}Ga(p,2n)$	≈ 550	30	>200
^{67}Cu	^{68}Zn	$^{68}Zn(p,2n)$	$\approx 10-15$	70	>100

Table 2.2: Radio-isotopes production at ARRONAX C70 cyclotron [4].

2.1.3 Ion Source

C70 cyclotron is equipped with two external ion sources as discussed in section 2.1.1. "The external ion source is more complex solution than an internal ion source since that asks for an injection line with equipment such as vacuum equipment, Faraday cup or other beam diagnostics, electrostatic or magnetic beam guiding, and focusing elements, etc. But it has several advantages over internal ion sources like PIG (Penning Ionization Gauge) source [8]". External ion source allows higher beam intensities and better machine vacuum which is needed for H^- ion acceleration. It also allows heavy and highly stripped ions. An electron cyclotron resonance (ECR) ion source is used for He^{2+} and HH^+ where Multi-cusp is for H^- and D^- ions. A basic introduction of both ion sources is described below:

ECR ion source: Its operational principle is shown in figure 2.5. Due to Lorentz force, electrons rapidly revolve around the magnetic field lines when they move in a magnetic field. The frequency of revolution or gyration frequency is called the cyclotron frequency ω_{cyc} (see equation 2.1). These electrons are accelerated or decelerated resonantly when radiation (microwave) of the same frequency (2.45 GHz at C70 ARRONAX) propagates into such a region. This depends on their transversal velocity component with respect to (w.r.t.) the electric field vector, when the condition of 'electron cyclotron resonance' [17] is fulfilled:

$$\omega_{cyc} = (e/m) * B \tag{2.1}$$

where, e and m are the charge and mass of the electron, respectively. The electrons in the plasma are confined in a superposition of magnetic field's axial component which is produced by permanent magnets and the radial magnetic field of a multi-pole magnet. The magnetic field at the center of the structure is minimum so this results in so called 'minimum-B-structure'. Therefore, a closed surface is created where the electron cyclotron resonance condition is fulfilled. Electrons passing through that closed surface can be resonantly accelerated. These electrons can gain sufficient energy to pass the resonance region so often and in this way, they ionize plasma atoms and ions into high charge states via successive single ionization. The ions in the plasma are still thermal energy (not accelerated) due to their relatively heavier mass. Therefore, they are confined by the space charge potential of the electrons and not by the magnetic field. This magnetic confinement is not perfect and electrons can still escape from the plasma. Since

the plasma is still neutral so positively charged ions will follow the electrons. Then by applying a high voltage and by using a suitable extraction geometry, those ions following the escaped electrons can be extracted from the ion source [20].

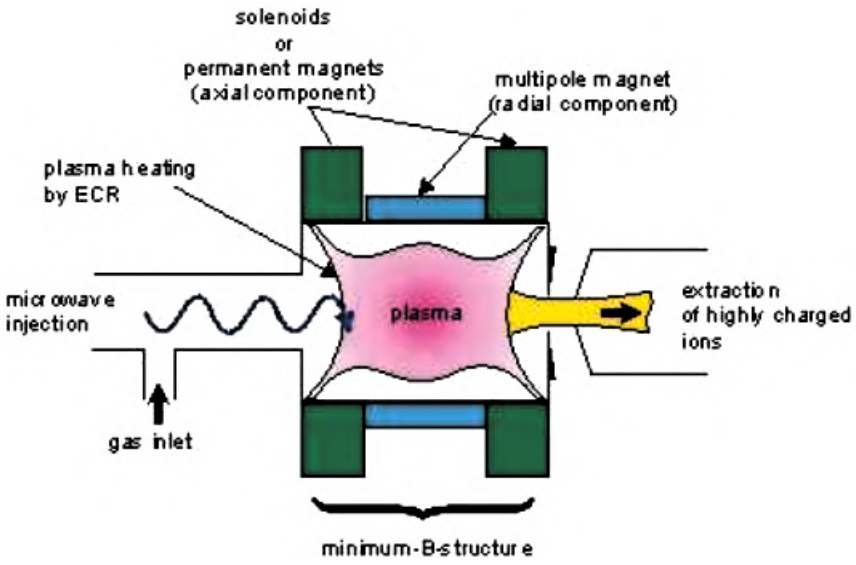

Figure 2.5: Operation principle of an ECR ion source [9].

Multi-cusp ion source: In the multi-cusp ion source, the primary ionizing electrons are emitted from tungsten filament cathode and chamber walls form the anode for the discharge. The surface magnetic field is generated by rows of permanent magnets to confine the primary electrons very efficiently. Therefore, the extraction efficiency of this source type is very high. As shown in figure 2.6, the filament (cathode), the chamber (anode), and plasma are three main components in this ion source. The magnets shown generate multi-cusp magnetic fields for primary ionizing electrons and plasma confinement. The open end of the source consists of a set of extraction electrodes. The gas is introduced into the chamber through a valve. The plasma is generated by primary ionizing electrons from the filament. Therefore, the extracted beam current depends on the magnetic field, the discharge voltage, and current, the voltage on the extraction electrode, and the length of the source chamber [10].

At ARRONAX, multicusp source chamber is divided into two parts. In the first chamber, electron from filament excites H_2 (D_2) molecules by collision, and in the second chamber, excited H_2 (D_2) molecules capture slow electrons from the plasma to give away H^- ions (D)[67].

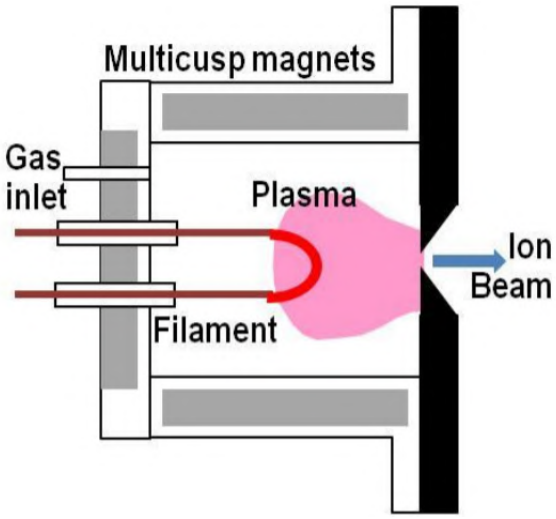

Figure 2.6: Operation principle of a multicusp ion source [10].

2.1.4 Injection system

The cyclotron C70 ARRONAX is equipped with an axial injection type system [11] to inject the beam into the cyclotron. The main goal of the injection line is to deliver or inject the beam into the cyclotron according to its acceptance criteria. The direction of the beam in the injection line is along the vertical axis towards the cyclotron center. At the end, just before the beam injection into the cyclotron, the beam is bent by 90 degrees angle from vertical to horizontal into the median plane of cyclotron dees. This is achieved by a spiral electrostatic inflector at ARRONAX. The spiral inflector (see figure 2.7) is basically a cylindrical capacitor gradually twisted taking into account the spiraling of the trajectory which is induced by the cyclotron's vertical magnetic field. It is designed in such a way that the velocity vector of the central particle is always perpendicular to its electric field. Therefore, the orbit is always positioned on an equipotential surface [21].

The magnetic elements in the injection line of the cyclotron are as shown in figure 2.7. They are constituted as follows 1-source glaser, 2-source steerer, 3-switching or dipole magnet, 4,5,6-three quadrupole magnets, 7-injection steerer, 8-injection glaser, 9-buncher, 10-cyclo glaser and 11-spiral inflector.

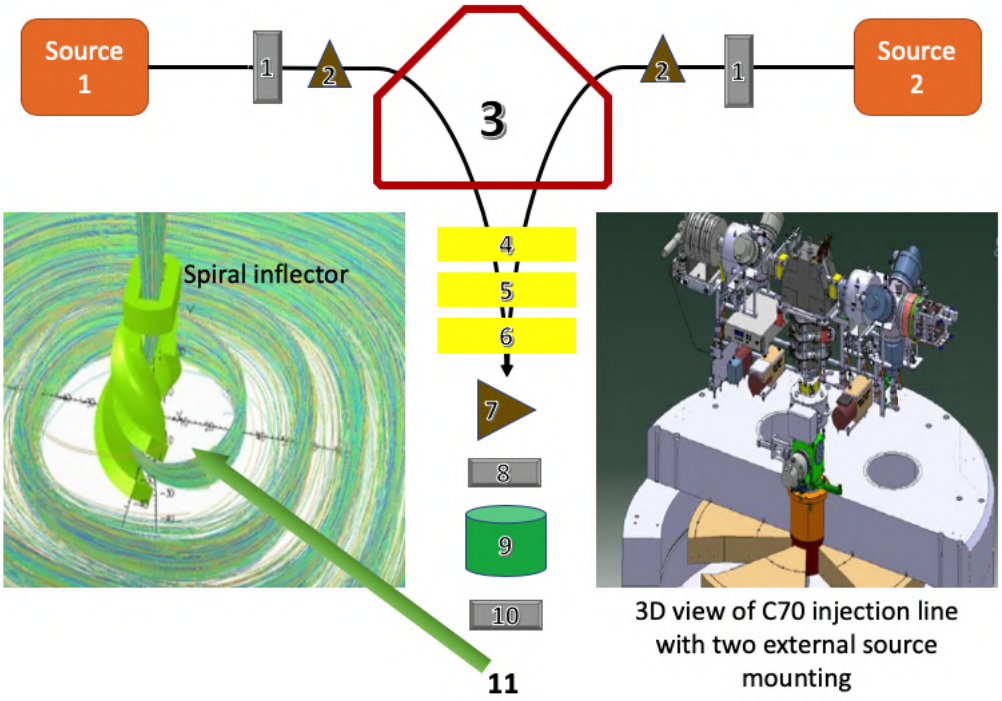

Figure 2.7: Various components of injection line at ARRONAX C70 cyclotron [18].

2.1.5 Cyclotron dees

General Principle: Injected particles from the injection line into the cyclotron dees center accelerate outwards from the center along a spiral path. These charged particles follow a spiral trajectory through a static magnetic field and gain acceleration through a rapidly varying electric field. It accelerates a charged particle beam using a high-frequency alternating voltage which is applied between two "D"-shaped hollow metallic electrodes called "dees" inside a vacuum chamber. In a classical cyclotron, the dees are facing each other and the gap between them creates a space where the particles move and accelerate. The magnetic field bends the particles in a circular path due to the Lorentz force which is acting perpendicular to the beam's direction of motion. This is illustrated in figure 2.8. The Lorentz force (F) equation is given by

$$F = qE + q(v \times B) \tag{2.2}$$

Where q, E, v, and B are charge of the particle, electric field, velocity of the particle and magnetic field, respectively.

C70XP Cyclotron: ARRONAX is an isochronous cyclotron with 4 high hill sectors (see

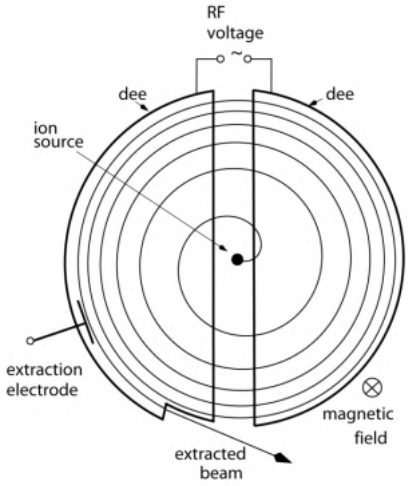

Figure 2.8: Example of cyclotron dees and its operation principle [12].

figure 2.10). The overall size of the cyclotron is of the order of 4 m and RF cavities with a frequency of 30.45 MHz and an acceleration voltage of 65 kV. The maximum radius for the accelerated particles is of the order of 1.2 m with the maximum hill magnetic field of approximately 1.09 Tesla for H^- beam (see figure 2.2). The arrangement of yoke or iron over the cyclotron dees is shown in figure 2.9. This arrangement of hill and valley sector magnets creates an azimuthally varying field in the cyclotron dees. The magnetic field at the valley and hill region is lower and higher, respectively (see figure 2.10). Due to such arrangement, a resource of vertical focusing is introduced by allowing the magnetic field to vary with azimuth along a circle [13]. For better understanding of this vertical focusing, consider the vertical component of the Lorentz force, F_y:

$$F_y = q(\vec{v} \times \vec{B})_y = -q(v_\theta B_r - v_r B_\theta) \tag{2.3}$$

where, $v_\theta B_r$, is obtained in a radially decreasing and rotationally symmetric magnetic field, and $v_r B_\theta$, requires an azimuthal modulation of the magnetic field. This modulation also generates a radial component of the velocity by itself.

This additional focusing is so strong that it dominates the vertical defocusing effect arising from a radially increasing field. The radial increase of magnetic field can be made such that the particle's revolution frequency remains constant in the machine, even for relativistic energies. C70 ARRONAX can basically accelerates two beam types described by charge (q) by mass (m) ratio:

1. **q/m=1/1:** H^- ion beam, accelerated in harmonic mode h = 2 [7].
2. **q/m=1/2:** He^{2+}, D^-, and HH^+ ion beams, accelerated in harmonic mode h = 4 [7].

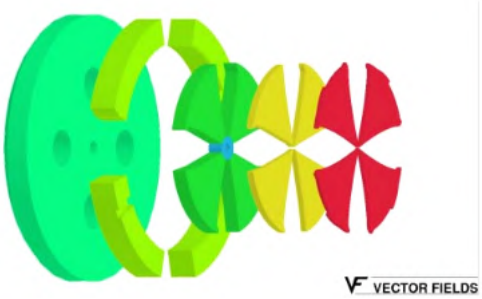

Figure 2.9: "Blown view of the C70 cyclotron iron. From left to right: the upper return yoke, the lateral return yokes, the sectors and the central plug, the poles and the covers" [15].

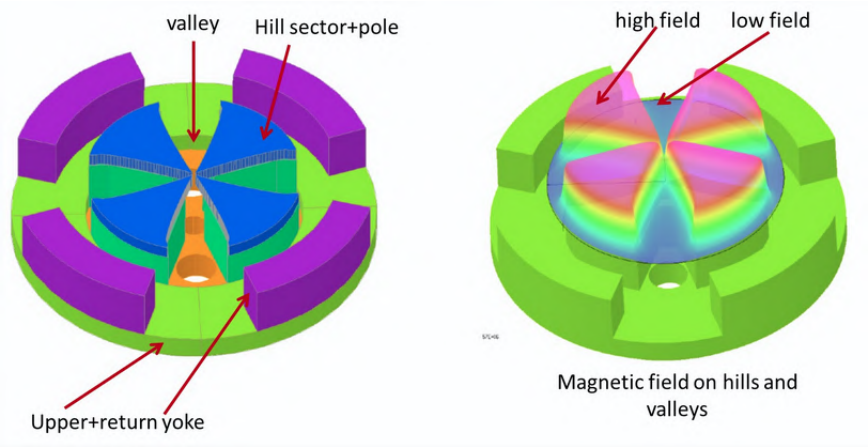

Figure 2.10: "Magnet of a compact azimuthally varying field cyclotron. Left: the hill sectors and poles, the valleys, and the different parts of the yoke. Right: histogram of the magnetic field" [13].

It is necessary to have the isochronous magnetic field for all ions beam type. The transformation from isochronous magnetic fields for both types of particles based on q/m ratio is performed by using correction coils that are wrapped around the poles. A gradient from these coils superimposes to the main field. These coils create inward and outward radial fields in the lower and upper poles, respectively (see figure 2.11(B)). That extra field created by compensation coils adds up to or subtracts itself from, the magnetic field by the main cyclotron coils. So the effective field can be adapted for the different types of ions (q/m=1/1 and 1/2). This is illustrated in figure 2.11(A).

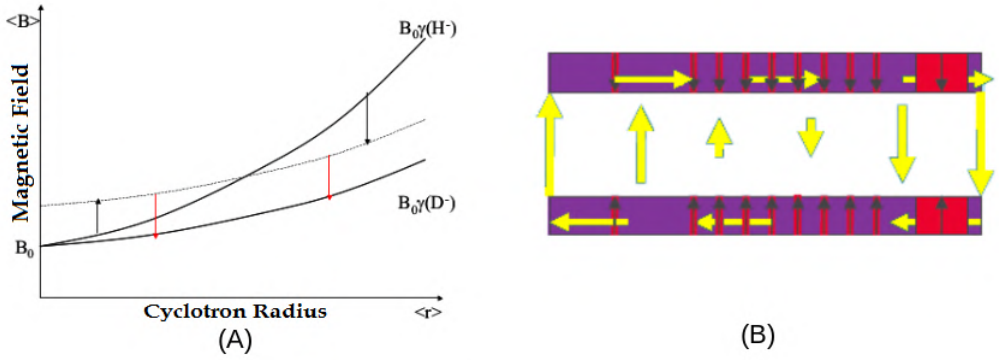

Figure 2.11: (A) Schematics of the transition from q/m=1 to q/m=1/2 isochronous field [19]. (B) Magnetic circuit schematics of the correction coil. Right side shows larger radii in the drawing. The main field is not shown. Black arrows and yellow arrows indicating the flow of current in the coils and the magnetic flux from the coils, respectively [19].

2.1.6 Beam extraction system

Extraction is the process to transfer the beam from cyclotron orbit to a beamline where the target station is located at the end. The beam extraction is the most complex process because, in a cyclotron, the turn separation is inversely proportional to beam orbit radius [21]. Due to this, the beam orbits come closer to each other near the extraction radius. Therefore, it is very difficult to deflect the last orbit of the beam without disturbing inner orbits and without losing beam particles. Also, the beam passes through the fringe fields of cyclotron magnets at the extraction radius. In this region, there are significantly large gradients and non-linearities in the magnetic field which makes the extraction process even more difficult. It is essential to avoid beam blow-ups or losses which degrade beam quality. There are two extraction systems at ARRONAX C70 cyclotron: stripper foil is used for negative ions and an electrostatic deflector is used for positive ions. Both processes are briefly described below:

Extraction by stripper foil: In this process of beam extraction, the particles pass through a thin metallic (diamond-like carbon foils at ARRONAX) stripper foil by which electrons get stripped off from the ion (see figure 2.12).

Due to this, the ion goes from negative to positive and an immediate change occurs in the local beam orbital radius of curvature. The relation between the local radius after (ρ_a) and

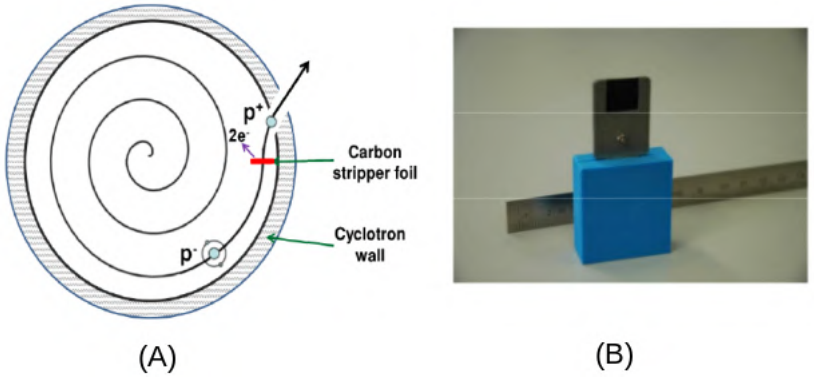

Figure 2.12: (A)Extraction by stripper foil [22]. (B)Example of diamond like carbon foil [21].

before (ρ_b) stripping is given by:

$$\rho_a = (Z_b m_a / Z_a m_b)\rho_b \tag{2.4}$$

where Z_a (stripping atom) and Z_b are the atomic numbers, m_a and m_b are the particle mass after (stripping atom) and before stripping, respectively. At C70 ARRONAX, H^- beam is being extracted by stripper foil where electrons strip off (H^- —> H^+ + $2e^-$) and H^+ beam is being transferred in a beamline. So the sign of local radius of curvature changes (ρ_a=–ρ_b). Due to which, the stripped particles are instantaneously deflected outward away from the cyclotron centre by the magnetic field. This is illustrated in figure 2.12(A).The most important advantages of using stripper foil extraction system are as given below:

- It is a very simple device for beam extraction.
- Extraction efficiency of 99.99% is possible [23].
- It is possible to extract variable beam energy by moving the stripper foil probe radially.
- Simultaneous dual beam extraction is possible [24].
- Quality beam with good beam optics can be achieved [25].

ARRONAX uses a self-supporting diamond-like carbon stripper foil with 10% boron-doped ("MicroMatter" the manufacturer). It has a thickness of 800 nm with 160 µg/cm^2 areal density.

Electrostatic deflector: In this method of extraction, two electrodes are used and between them, there is a DC electric field directing outside of cyclotron. The idea is to give an initial angular deflection to the beam which directs the beam outward. The inner electrode, which is

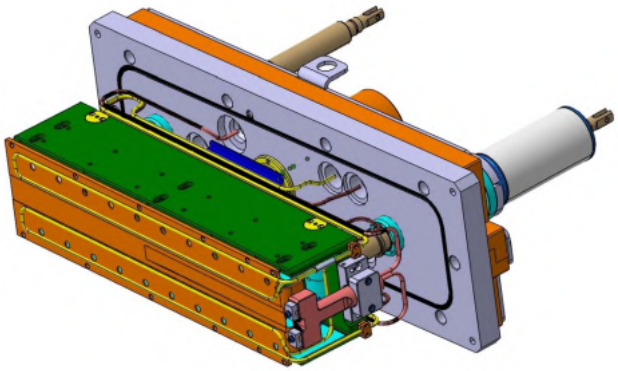

Figure 2.13: General view of the C70 electrostatic deflector [26].

often called a septum, is placed at the last beam orbit radius. It is always grounded in order to avoid any interference of its electric field with the inner orbits of the beam. It can heat up due to beam losses so generally, the septum is water-cooled. This type of extraction system is commonly used for stripped ions or positively charged ion beams so the outer electrode is of negative potential. The angle of that electrode guide the extracted orbit and extract the beam efficiently.

This thesis is based on a proton beam which uses a stripper foil extraction system to extract protons from H^- beam in the beamlines. Therefore, the thesis work is more focused on stripper extraction rather than electrostatic deflectors.

2.2 Transverse Beam Dynamics

2.2.1 Introduction

Accelerator physics can be described as a description of charged particle beam dynamics and their interactions under the influence of an external electromagnetic field. All acceleration and beam trajectories are derived from the Lorentz force equation (2.2) in accelerator physics. The force due to magnetic field is mostly used to guide the particle beams along desired or designed trajectory whereas electric force is used to increase the particle energy. In all particle accelerators, the charged particle beam is designed to follow its pre-designed path which is called design orbit [13]. The same applies to beam trajectory in a beamline. In principle, one can calculate the trajectory of each particle in the accelerator by applying Maxwell's equations [27, 28, 29, 30]. As mentioned earlier at ARRONAX C70 cyclotron, we have several beamlines.

A beamline is used to guide the beam to the target station and there is no beam acceleration involved. There are several electromagnetic elements in a beamline which provide bending and focusing to the beam to keep it and hold them close on the designed trajectory. Thus, the beam dynamics of a beamline is studied.

Here, we discuss transverse beam dynamics in a beamline and will focus mainly on the linear beam dynamics which is based on linearly dependent forces. At ARRONAX, beamline elements include dipole and quadrupole magnets. Linear beam dynamics based on dipole and quadrupole magnet are described below:

Dipole or bending magnet: Bending magnet (see figure 2.14) is used to bend the beam along a predefined trajectory or path by introducing a perpendicular magnetic field to the path of the beam. This deflects the particles according to below equations:

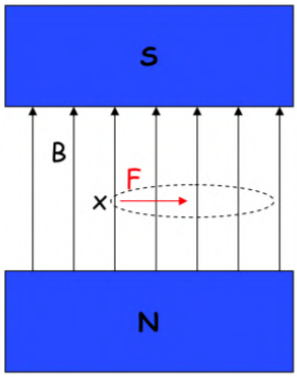

Figure 2.14: Dipole magnetic field. x-beam direction into the paper and force F.

$$mv^2/r = qvB/c \quad \text{and} \quad p = qBr/c \tag{2.5}$$

where r is the bending radius, v is the speed of particle, relativistic mass m=γm$_o$ (where $\gamma = 1/\sqrt{1 - v^2/c^2}$ and c is the speed of light in a vacuum) and p is the momentum of the particle. Bending magnet creates a dipole field. A magnet with flat poles generate homogeneous magnetic field and the dipole bending strength ($1/\rho$) is defined as:

$$1/\rho = qB_o/p \tag{2.6}$$

Here fringe fields have been neglected and B$_o$=μ_oNI/h where NI is the number of ampere-turns, μ_o is permeability of vacuum ($4\pi{\cdot}10^{-7}$ Henry/m) and h is the gap height. The N turns of

current I generate a small magnetic flux H=B/μ in the iron where μ is the magnetic permeability.

Quadrupole magnet: Particle beam is diverging by nature, which means it has a tendency to spread out. The Focusing devices are then required to keep the particle beam focused. An ideal quadrupole magnet has four symmetrical iron poles (see figure 2.15). Quadrupole magnets serve that purpose but they provide a focusing effect in a plane. It is described by the equations below:

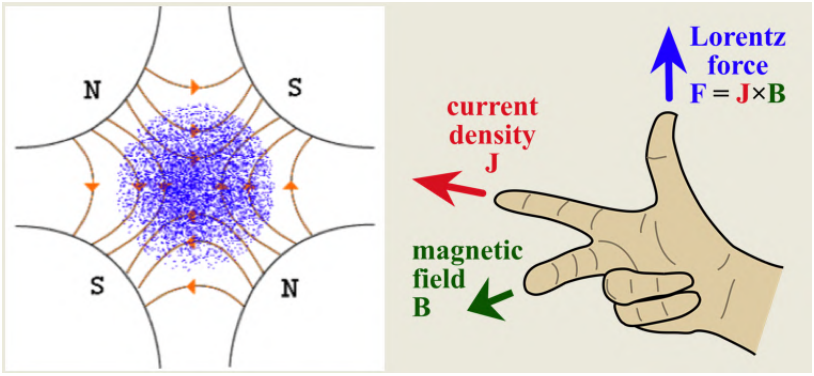

Figure 2.15: Quadrupole magnetic field (left side) and Right hand rule to deduce the lorentz force acting on positively charged particle (right side).

$$B_x = -gy \quad \text{and} \quad B_y = -gx \tag{2.7}$$

where g is the field gradient and given by $g = -\frac{\partial B_y}{\partial x} = 2\mu_o NI/R^2$, R is the distance between pole tip from the center and NI is the number of ampere-turns per pole. Generally, the gradient g is normalized to particle momentum p by defining a term called quadrupole strength $k = qg/p$. A quadrupole magnets focalize in one plane and defocalize in another plane. According to the right hand rule (see figure 2.15), the force on a particle can be deduced. Therefore quadrupole doublet (pair of quadrupole magnet - focusing and defocusing) is used to achieve net focusing effect in both planes (one focusing on the x plane and de-focusing in the y plane, and the other doing the opposite).

2.2.2 Beam transport

Four coordinates are commonly used to describe the beam properties in a transverse direction. These are beam displacements and divergence in x and y planes. There are two more coordinates considering longitudinal direction (longitudinal displacement and energy spread). The

longitudinal beam dynamics is not in the scope of this thesis so we will talk about the transverse part of it. Transverse beam coordinates are summarized in the table 2.3.

Symbol	Dimension	Description
x	mm	horizontal displacement
$x^{'}$	$mrad$	horizontal divergence
y	mm	vertical displacement
$y^{'}$	$mrad$	vertical divergence

Table 2.3: Description of transverse phase space beam coordinates.

In a linear approximation, we can assume that the transition or transformation of the initial particle state to the final state within a beamline can be described by a matrix. The transverse phase space vector $\vec{x}(s)$ of an arbitrary particle at the position 's' can then be written as:

$$\vec{x}(s) = R(s)\vec{x}(0) \tag{2.8}$$

where $\vec{x}(0)$ and $\vec{x}(s)$ represents the initial and final beam coordinates, respectively. R(s) is the transfer matrix of the element from where the beam has transitioned to the final position. Similarly, If the particle is transitioning through N sections in a beamline and each section having a designated transport matrix R_i, with i=1 till i=N, the final phase space vector of the particle is given by:

$$\vec{x}(s) = R(N)R(N-1).....R(1)\vec{x}(0) \tag{2.9}$$

For example, let's say, the trajectory of a particle without any forces acting on it, the final transverse phase space in x-plane (beam displacement x and divergence $x^{'}$), is discussed for this simple case. The transfer matrix for a free drift of the distance L is given by:

$$R = \begin{pmatrix} 1 & L \\ 0 & 1 \end{pmatrix} \tag{2.10}$$

Now insert this matrix into equation (2.8), to get:

$$\begin{pmatrix} x \\ x^{'} \end{pmatrix} = \begin{pmatrix} 1 & L \\ 0 & 1 \end{pmatrix} \begin{pmatrix} x_0 \\ x_0^{'} \end{pmatrix} = \begin{pmatrix} x_0 + Lx_0^{'} \\ x_0^{'} \end{pmatrix} \tag{2.11}$$

As one can clearly see, the particle's divergence is still the same but it has displaced by $Lx_0^{'}$ which one would have already expected. This calculation is for x and will remain the same for y. For dipole and quadrupole magnets effect in x and y will be different for obvious reasons.

- Dipole magnet: For an ideal dipole magnet k=0. For horizontal motion |K|=1/ρ^2. For arc length equals to 'd' in the magnet, we have $\phi = d/\rho$ and the corresponding transfer matrices will be given by:

$$M_y = \begin{pmatrix} 1 & d \\ 0 & 1 \end{pmatrix} \quad \text{and} \quad M_x = \begin{pmatrix} cos\phi & \rho sin\phi \\ -sin\phi/\rho & cos\phi \end{pmatrix} \tag{2.12}$$

- Quadrupole magnet: For quadrupole magnet |K|=k and $\rho = \infty$ if s=d is the length of the quadrupole then $\phi = d\sqrt{k}$. Let's say, the quadrupole is focusing in y-plane and defocusing in x-plane for k>0. The transfer matrix will be:

$$M_y = \begin{pmatrix} cos\phi & sin\phi/\sqrt{|k|} \\ -\sqrt{|k|}sin\phi & cos\phi \end{pmatrix}, M_x = \begin{pmatrix} cosh\phi & sinh\phi/\sqrt{|k|} \\ \sqrt{|k|}sinh\phi & cosh\phi \end{pmatrix} \tag{2.13}$$

  In many practical cases thin lens approximation ($d <<<< \sqrt{k}$) are used for quadrupoles so focal length $f = 1/kd$. In this case transfer matrices are reduced to:

$$M_y = \begin{pmatrix} 1 & 0 \\ -1/f & 1 \end{pmatrix} \quad \text{and} \quad M_x = \begin{pmatrix} 1 & 0 \\ 1/f & 1 \end{pmatrix} \tag{2.14}$$

  For k<0 the above equations will get interchanged and quadrupole becomes focusing in x-plane and defocusing in y-plane.

2.2.3 Transverse beam emittance

In the "beam transport" section above, we have only discussed "single-particle dynamics". In this section, we are going to discuss "multi-particle dynamics". Beam dynamics of multi-particle can be considered as a superposition of various single-particle tracks if we neglect all possible interactions between beam particles. The transverse momentum (p_x, p_y) is much smaller than the longitudinal momentum (p_z). So it is possible to write this useful approximate expressions of transverse beam divergences, $x' = p_x/p_z = v_x/v_z$ (horizontal plane x, v is the velocity of particle) and vice versa for vertical plane. Particles in a beam have a random distribution of velocities (transverse) at the same location and a spread in various directions. Focusing elements like quadrupole, can only influence the average motion of the particles. To understand and put all single-particle tracks on a coordinate system, we can assume that all

particles are distributed around the origin then the transverse shape of a beam can be easily studied by defining an ellipse within phase space that contains the distribution of the particles in a beam. This is illustrated in figure 2.16. The General equation of an ellipse in the Cartesian coordinate system can be described by:

$$\frac{x^2}{a} + \frac{y^2}{b} = 1 \tag{2.15}$$

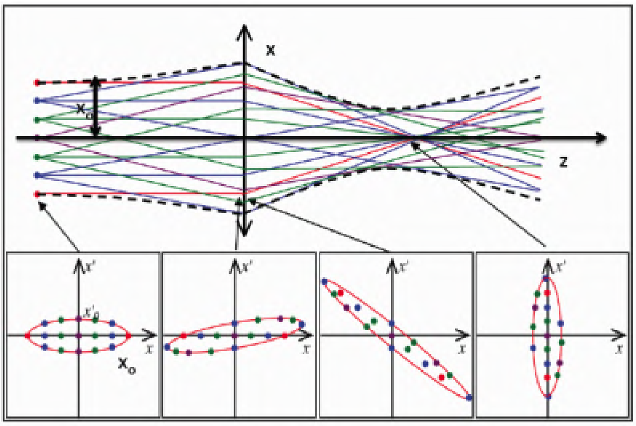

Figure 2.16: Particle trajectories and phase space evolution of a beam [93].

For a tilted ellipse, one has to add an additional term $2xy/c$ to equation (2.15). This equation can be re-written as a matrix product where σ_x (a matrix) is multiplied from both sides by ellipse's position vectors. The parameters a and b represent diagonal elements of matrix σ_x, while c represents its off-diagonal elements. With vector $\vec{x}$ pointing onto the edge of the ellipse, one can define an ellipse matrix σ_x such that its inverse matrix σ_x^{-1} satisfies the equation of the ellipse (2.16).

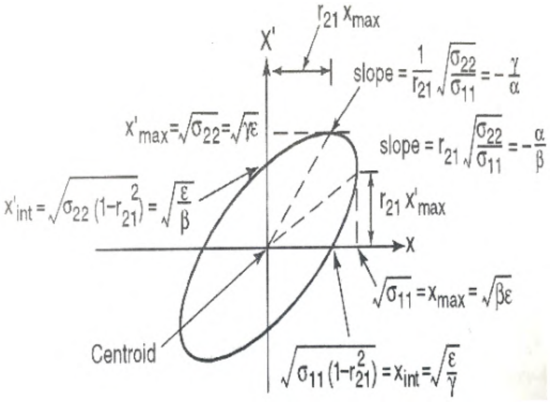

Figure 2.17: Representation of beam emittance ellipse [90].

$$\vec{x}^T \sigma_x \vec{x} = 1 \tag{2.16}$$

where $\sigma_x = \begin{pmatrix} \sigma_{11} & \sigma_{21} \\ \sigma_{21} & \sigma_{22} \end{pmatrix}$ and $\sigma_x^{-1} = \frac{1}{det(\sigma_x)} \begin{pmatrix} \sigma_{22} & -\sigma_{21} \\ -\sigma_{21} & \sigma_{11} \end{pmatrix}$. The descriptive meaning of these matrix elements for the phase space ellipse is illustrated in figure 2.17, using the correlation parameter $r_{21} = \frac{\sigma_{21}}{\sqrt{\sigma_{11}\sigma_{22}}}$. It is also clear that the extension of the ellipse in x only depends on σ_{22} and in $x^{'}$ on σ_{11}. The three independent parameter α, β, and γ are called "Twiss parameters". One dependent parameter ε (depends on α and β) is termed as the beam "Emittance". Emittance is an important property of a charged particle beam in an accelerator. It is a measure of average particle distribution in a phase space. For the best representation of all particles, the emittance ellipse is fitted on the phase space distribution then the emittance ($\varepsilon_x = det(\sigma_X)$) can be written as:

$$\varepsilon_x = n^2 \sqrt{< x^2 > . < x'^2 > - < x.x' >^2} \quad [32] \tag{2.17}$$

where $< x^2 >= \sigma_{11}$, $< x^{'2} >= \sigma_{22}$ and $< x.x^{'} >= \sigma_{21}$. "n" is the parameter which provides means to expand the emittance ellipse such that it includes more particles in the distribution. For example: 2σ-emittance refers to n=2, with σ is the RMS size of the distribution. The quantity defined in the equation (2.23) is termed as RMS-emittance since it considers the RMS values of the distribution in x and $x^{'}$.
According to Liouville's theorem, the normalized emittance (relativistic emittance which is independent of beam energy) of any beam distribution remains constant in the ideal conditions (no interaction between particles) under the influence of any electromagnetic fields. In simple words, it means the shape of the ellipse may change but its area will remain always constant under the effect of any conservative forces.

We have discussed phase space ellipse or the concept of transverse beam emittance. Now, we discuss how particles are distributed within that ellipse. We can assume a constant density but this is a very crude assumption far from reality. A closer model might be to assume the phase space particle distribution following a Gaussian distribution. In this case, the density of

the particles in the phase space distribution can be written as:

$$\rho(\vec{x}) = \rho_0 exp^{-(\frac{1}{2}\vec{x}^T\sigma_x^{-1}\vec{x})} \tag{2.18}$$

We have already discussed in the previous section (2.2.2) about transfer matrix to derive the dynamics of single particle in the phase space. Similarly, emittance matrix can be used to derive dynamics of multi-particle. In this multi-particle formalism, equation (2.8) becomes:

$$\sigma_x(s) = R_x(s)\sigma_x(0)R_x^T(s) \tag{2.19}$$

Now, Let's discuss the transition of the particle beam in the case of free drift space and a quadrupole (thin lens approximation) for multi-particle dynamics. Here just to simplify calculations, an assumption has been made that the off-diagonal elements (σ_{21}) of the emittance matrix are considered to be zero.

$$\sigma_x(L) = \begin{pmatrix} 1 & L \\ 0 & 1 \end{pmatrix} \begin{pmatrix} \sigma_{11}(0) & 0 \\ 0 & \sigma_{22}(0) \end{pmatrix} \begin{pmatrix} 1 & 0 \\ L & 1 \end{pmatrix} \tag{2.20}$$

$$= \begin{pmatrix} \sigma_{11}(0) + L^2\sigma_{22}(0) & L\sigma_{22}(0) \\ L\sigma_{22}(0) & \sigma_{22}(0) \end{pmatrix}$$

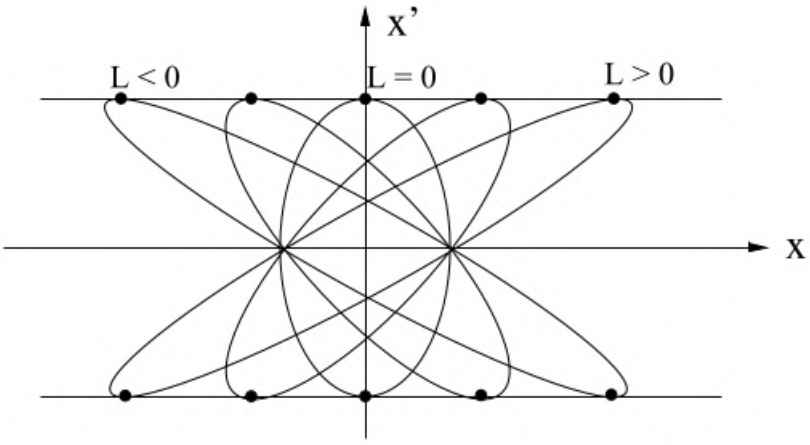

Figure 2.18: Illustration of phase space ellipse during a free drift [31].

From the result above, one can conclude that the shape of the ellipse will change but area remains constant as it is expected for a free drift space of length L. This is illustrated in the figure 2.18.

Similarly, for focusing quadrupole in the thin lens approximation:

$$\sigma_x(1/f) = \begin{pmatrix} 1 & 1/f \\ 0 & 1 \end{pmatrix} \begin{pmatrix} \sigma_{11}(0) & 0 \\ 0 & \sigma_{22}(0) \end{pmatrix} \begin{pmatrix} 1 & 1/f \\ 0 & 1 \end{pmatrix} \tag{2.21}$$

$$= \begin{pmatrix} \sigma_{11}(0)) & \sigma_{22}(0)/f \\ \sigma_{22}(0)/f & \sigma_{22}(0) + \sigma_{11}/f^2 \end{pmatrix}$$

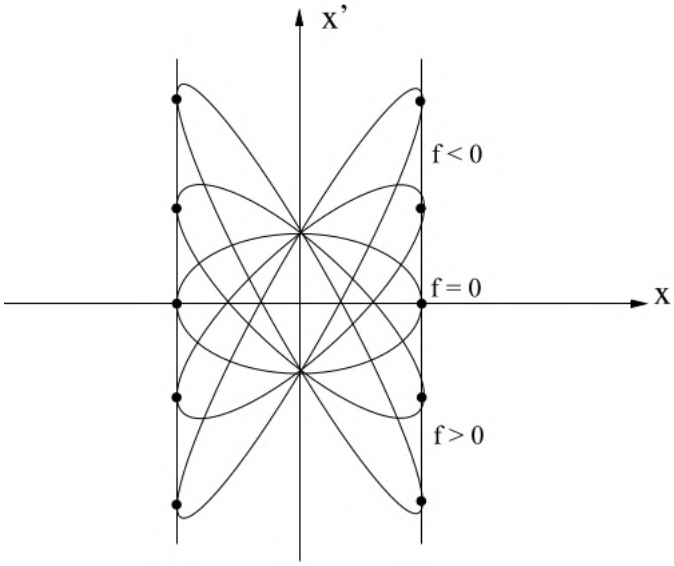

Figure 2.19: Illustration of phase space ellipse during a focusing quadrupole (thin lens approximation) [31].

In this case, the particles receive a kick, induced by the Lorentz force which changes their velocity but their position remains the same. The variation in the shape of an ellipse with respect to focal length 'f' is illustrated in figure 2.19.

These two sections (2.2.2 and 2.2.3) give an insight into understanding the terms used in accelerator physics and explained the idea of beam emittance. It is also introduced here how beam transfer matrices work in single and multi-particle beam dynamics. In the next section, we will continue discussion on transverse beam emittance and its measurement techniques.

2.2.4 Emittance measurement technique

Emittance is one of the beam property that has to be studied for evaluating any accelerator's performance. It is important to have a measure of the quality of such beams to interpret their ability to be transported over long distances and maintain it to be focused into a small space with minimum divergence. Beam emittance should remain the same as designed in ideal conditions, but there are several sources of emittance growth in the real world. Thus emittance measurements should be performed from time to time. So before heading towards emittance measurement techniques, briefly discuss two most common sources of emittance growth in a cyclotron.

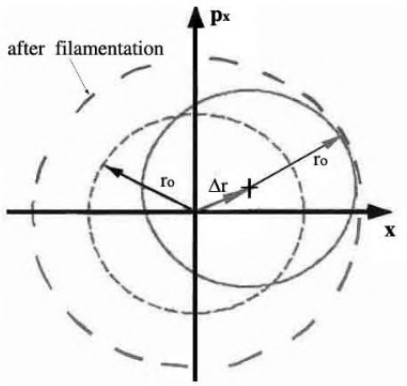

Figure 2.20: Increase of emittance due to mismatch at beam injection into the cyclotron [33].

Emittance growth due to mismatch at transfer: Let's take an example of beam transfer from an injection line to cyclotron dees similar to ARRONAX C70 cyclotron. Now assume an injected beam with an error in position (Δx) and angle ($\Delta x^{'}$) with respect to the design orbit. Then in the normalized beam displacement (x) and momentum (p_x) in the x-direction from the phase space, the emittance designed circles of the beam are no longer concentric with the Eigen ellipse or acceptance circle of the machine. The acceptance circle defines the maximum emittance that can be transmitted and is given by $A = a^2/\beta$ where, A is the acceptance circle, a is the half-aperture and β function of a beam channel. The minimum of this "A" defines the acceptance circle. If these circles are radially displaced by an amount (Δr) as shown in figure 2.20. This can happen due to misaligned beam during injection. Due to which an emittance dilution mechanism called filamentation [34] takes place.

This mechanism is illustrated in figure 2.21. The β function and its derivative β' at the injection position in a circular machine define phase ellipse or acceptance circle or eigen ellipse

(see figure 2.21(a)). When the injection line (transfer line) has different β parameters at the injection point, then the emittance ellipses of the incoming beam have a distinct shape and different orientation from the machine phase space (2.21(b)). As the beam circulates in circular machines like cyclotron, each particle will turn around in transverse phase space on the ellipse relative to its initial injection conditions (x,x') with an angular frequency. Thus, particles start to move with different speed on different phase space ellipses. The beam changes its initial form first into an S-shaped area (2.21(c)). Later, this beam diluted into a distribution that fills the machine phase space ellipse (2.21(d)). Clearly, the phase space area after filamentation is going to be larger than the injected beam.

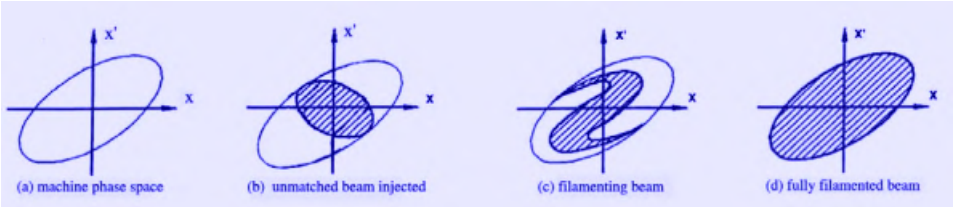

Figure 2.21: Filamentation of a mismatched beam [34].

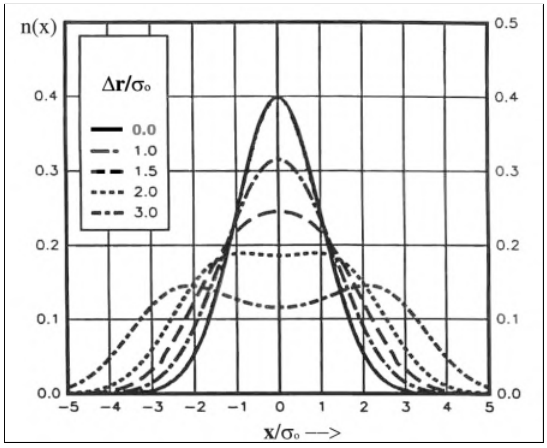

Figure 2.22: Projected distribution of an originally Gaussian beam after filamentation of a position error Δx at injection [34].

After filamentation, the beam area will increase from (r_0^2) to $((r_0 + \Delta r)^2)$ which ultimately results in the growth of geometrical emittance. The shape of the final distribution greatly depends on the magnitude of error or displacement. Double humps are a sign of a marginal mismatch errors at transfer (see figure 2.22). Similarly, these mismatches can come from focusing errors in the injection line or from space charge effect [36, 37, 38] which leads mainly to a widening of the distribution or emittance growth.

Emittance growth due to scattering on obstacles: As explained earlier, at ARRONAX

C70 cyclotron, we use stripper foils to strip off negative ions from H^- beam. This mechanism also leads to emittance growth. The transition through such obstacle or foil leads to an increased angular divergence of the beam due to coulomb scattering. The blow-up of RMS emittance can be estimated by using classic multiple scattering formula:

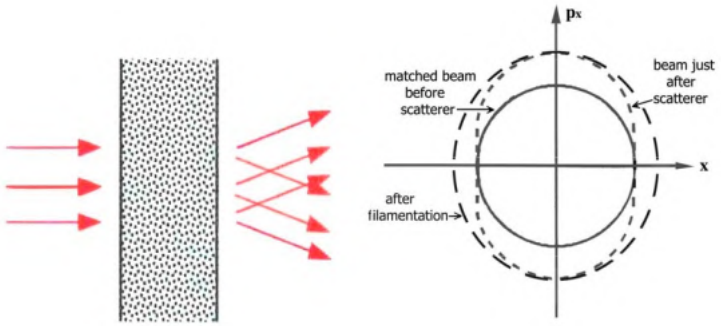

Figure 2.23: Left side shows Scattering through a foil and on the right side, the representation of beam before and after filamentation [33].

$$\theta_{rms} = \frac{13.6MeV/c}{p\beta_p} q_p \sqrt{\frac{t}{L_{rad}}} \quad [35] \tag{2.22}$$

where θ_{rms} is RMS scattering angle for a particle charge q_p, momentum p [MeV/c], $\beta_p = v_p/c$, radiation length of the foil L_{rad} and thickness t. The increase in RMS emittance after foil can be calculated by:

$$\Delta\varepsilon_{n\sigma} = \frac{1}{2}(n\theta_{rms})^2\beta_x \tag{2.23}$$

Stripper foils have several advantages as explained earlier but emittance growth can not be avoided. So proper handling of stripper foil is very important for controlled emittance growth at such accelerators.

Up to now, we have discussed the importance of emittance measurement and few sources of its growth. So let's discuss transverse emittance measurement techniques and devices which are often used by accelerator physicists.

Emittance measurement techniques -

1. Wire scanner technique: Beam emittance can not be measured directly. It is always inferred from measured beam properties in transverse plane (x, y). In wire scanner technique, a wire beam profile monitor is used which is an intercepting or destructive emittance measur-

ing device which when placed in the beam's trajectory measures the beam flux as a function of transverse position. It samples the beam in transverse planes and in order to extract information about transverse beam divergence, the beam must be sampled under different transport conditions. The quadrupole current variation method (explained in chapter 3.3) is used to sample the beam in several transport conditions. By integrating all these measurements, one can calculate RMS emittance. For better measurements, one can use multiple profilers, each placed at some fixed drift length. For more details on this method [39, 40].

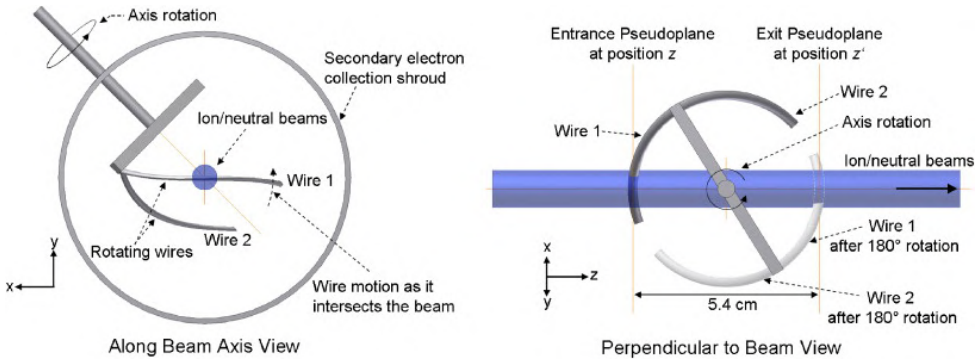

Figure 2.24: Operation principle of a multi wire scanner [94].

As shown in the figure 2.24, a thin wire scans the beam very rapidly at about 20 m/s for fast scanners. Generally, the rotational mechanism is used to do the wire scan. The beam-wire interaction produces secondary emission current which is detected by using inorganic scintillator and photo-multiplier tube technology which is explained in section 2.3.2. At ARRONAX, a low-intensity beamline is also equipped with such a device (single wire scanner).

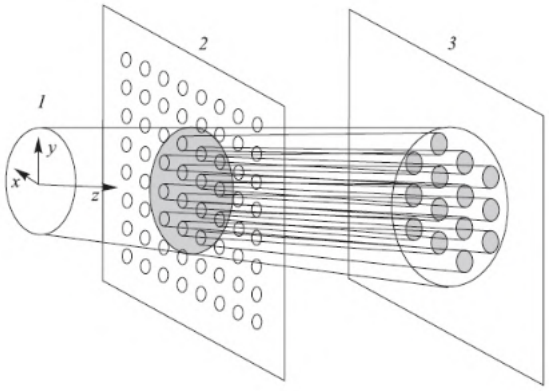

Figure 2.25: Pepper-pot technique for emittance measurement. Here 1,2, and 3 are the beam, the pepper-pot mask or plate, and the profile measuring screen, respectively [42].

2. Pepper-pot technique: In the wire scanner technique, one has to sample the beam under several transport conditions but emittance measurement can be done in a single shot by

using the pepper-pot technique. In pepper-pot diagnostics [42], the beam is collimated into several small 'beamlets' by a circular opening of known dimension, the divergence of these collimated beamlets can be detected after they propagate some sufficient distance where the profile measuring screen is installed to sample these small beamlets. This is illustrated in figure 2.25.

The profile monitor is placed downstream from where the beam is screened by a pepper-pot plate. A pepper-pot plate contains an array of equispaced holes. This plate stops the beam, allowing a collimated beam through those holes which incident on the profile monitor. The total intensity of the beam passing through the holes still provides information about the spatial profile of the beam, then these profiles can be used to extract information on the divergence or angular distribution of the beam at the position where the pepper-pot plate is placed.

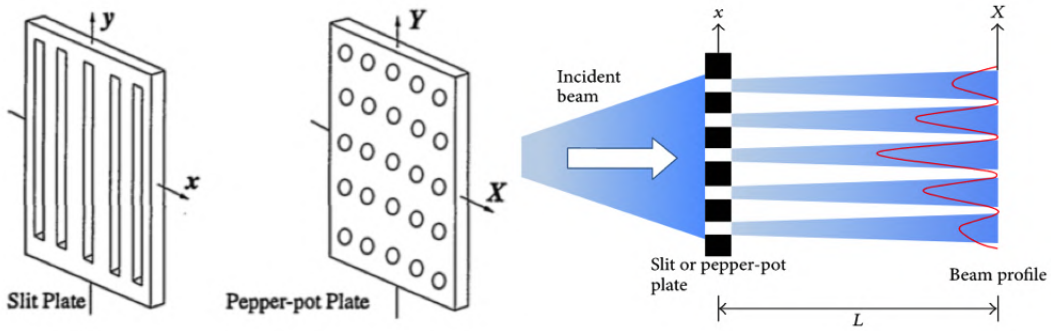

Figure 2.26: Comparison of slit and pepper-pot techniques [42].

There is a 'slit scanner' method to measure beam emittance which uses the same principle as a pepper-pot technique, but the pepper-pot technique is more evolved. In the Slit scanner technique [41, 42], one can make a measuremen in a single shot but with lesser precision than the pepper-pot plate because of more defined pepper-pot plate geometry (see figure 2.26). Moreover, pepper-pot technique samples the beam in 2D where slit scanner in 1D. An image processing algorithm is being used in the pepper-pot technique, which measures the pixels of the image to create a beam profile for emittance measurement. However, the generalization of the slit emittance formula [42] to the pepper-pot case can be used straightforward. Instead of projecting slit image lines to the x-axis, we sum up all pepper-pot images in x direction to calculate ε_y and in y for ε_x.

The methods discussed here are very basic and highly used in industrial accelerators. There are several other methods to measure transverse beam emittance. For more information, readers

may be referred to this document [95] by CERN Accelerator School (CAS) where detailed information on other techniques can be found.

2.3 Beam Loss Monitor (BLM)

2.3.1 Introduction

The beam loss monitor is a commonly used beam diagnostic tool at particle accelerator facilities. It measures particles lost by the beam. It can also be used as a beam tuning device because it protects beamline elements from radiation damage and long term activation due to beam losses. Ionizing radiation can come from both beam and non-beam sources such as beam halo, focusing and steering errors, residual gas scattering, foreign objects in the beam, etc. These losses may be distributed around the accelerator. They are very often the result of improper focusing or bending, or misaligned beam. Losses should be minimized to keep activation level low enough for hands-on maintenance, and to protect machine parts from beam related damage. So a beam loss monitor system should define the threshold level of those losses.

2.3.2 Detection of ionizing radiation

The most widely used BLMs [49] in industrial accelerators can be subdivided into two categories: gas ionization chamber based and scintillation or fluorescence based detectors. Both represent an energy transfer from the incoming charged particle to the atomic electrons, exciting them. Usually the Bethe-Bloch formula is used to describe this given below:

$$dE/dx = -4\pi N_A r_e^2 m_e c^2 z^2 (Z/A)(1/\beta^2)[1/2 \ln(2m_e c^2 \gamma^2 \beta^2 / I^2) T^{max} - \beta^2 - \delta/2] \quad (2.24)$$

where β=v/c, v is velocity of the particle, $\gamma = 1/\sqrt{(1-\beta^2)}$, E is the energy of the particle, x is the distance travelled by the particle, z is the charge of the incident particle in units of e, $m_e c^2$ is the rest mass of electron, N_A is Avogadro's number, Z/A is the ratio of atomic number and atomic weight of absorbing material, I is the mean excitation potential, ρ is the density correction, T^{max} is the maximum energy transfer in a single collision. For detailed discussion on Bethe-Bloch formula [45].

Let's discuss briefly about scintillation or fluorescence based detectors and ionization chamber based detectors.

Scintillation detectors: Scintillation detectors utilize a material which fluoresce, i.e., produce flashes of light when struck by incident radiation. The scintillator detects the radiation being emitted (higher the energy loss, brighter the scintillation). Then the scintillation event is converted into an electric signal. The pulse height analyzer sorts the energy which is being recorded. It can measure energy spectra with high counting rate capabilities. Scintillation detectors can be sub-divided into two categories i.e., inorganic and organic scintillators. Inorganic scintillators work at crystal level where organic at molecular level. Organic scintillators [46] are best suited for the detection of low energy particles ($< 10MeV$) due to its lower atomic number Z than inorganic scintillators. Inorganic scintillators are commonly used in high particle energy detection studies so let's briefly discuss about it.

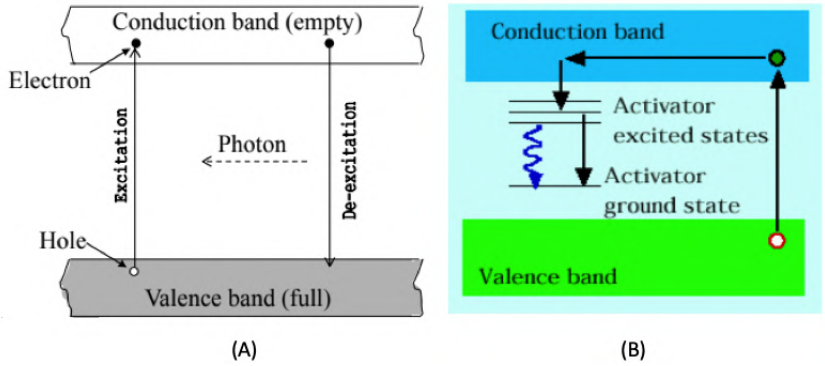

Figure 2.27: (A) Pure crystal band [98]. (B) Crystal band with activator[98].

- **Inorganic Scintillators** – In the pure crystal, absorption of certain amount of energy excites an electron from the valence band to the conduction band leaving a gap in the valence band. When this electron returns to the valence band, emits a photon. But in pure crystals, bandgap widths are such that the emitted photon is too high to fall within the visible range. Therefore a small amount of impurities are added to the crystal called as 'activators'. This is illustrated in figure 2.27. For example, "Thallium is added to NaI in trace amounts (10^{-3} per mole)" [48]. Activators create special sites in the lattice. The energy levels created by the presence of activator within the crystal are narrower than in the pure crystal so the emitted photon energy tends to decrease and falls within the visible range. Thallium activated sodium iodide NaI(TI) and cesium iodide CsI(TI) are highly used inorganic scintillator detectors due to their high light output. However, these are used with an amplifier tube termed as a photo-multiplier tube' (PMT). PMTs basically perform two functions.

  First is the conversion of visible light photons into an electrical signal and second is the amplification of signals. As shown in figure 2.28, photons hit the photo-cathode (made of alkali metals like Cs, Na, K) which liberates photo-electrons. Photo-cathode should

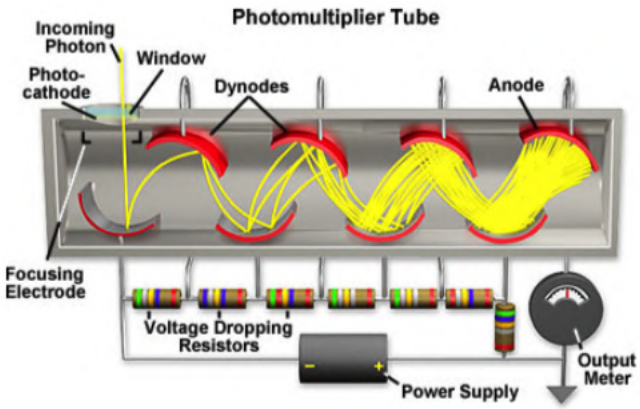

Figure 2.28: Operation principle of photo-multiplier tube [41].

be thin enough, so photo-electrons can escape. This photo-electron amplification is done by a series of dynodes and the amplification depends on these dynodes potentials. All these amplified photo-electrons are collected at the anode and we can measure that in the form of an electrical signal.

Gas ionization detectors: Mechanism of gas detector [51] is simpler than scintillation detector. In gas detectors as shown in figure 2.29, radiation is sensed by detecting the electrons or ions produced by the deposition of energy of ionizing radiation passing through the gas-filled detector. Thanks to an applied high voltage on the detector, the positive anode attracts free electrons and the negative cathode attracts the positive counter from the ion pairs.

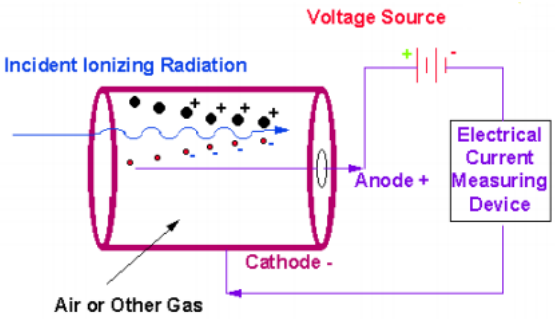

Figure 2.29: Operation principle of gas ionization detectors [50].

The electric field E = V/D (applied voltage V and drift space D) causes electrons and positive ions to drift in opposite directions toward the anode and cathode, respectively. The gas used may be air, helium, neon, argon, hydrogen or mixtures.

Operating regions of gas-filled detectors as shown in figure 2.30. The drift time and the fraction of the created electrons by ionizing radiation reaching the anode depend on the applied voltage. If the applied voltage is small (<100 volts), ion pairs recombine rather than move

towards electrodes. If the applied voltage is larger and is sufficiently high in this region so that only a negligible amount of recombination occurs.

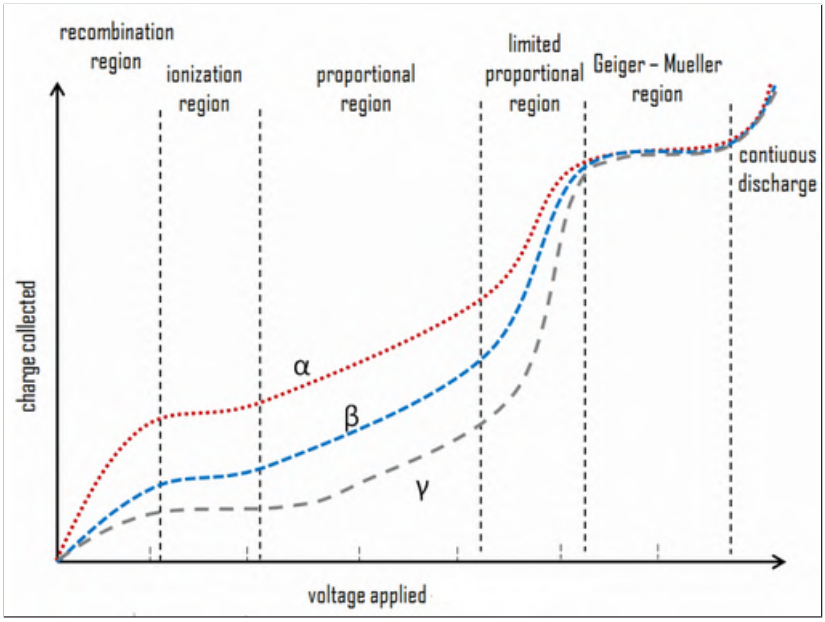

Figure 2.30: Regions of gas ionization detector [48].

The number of ions collected is directly related to the amount of energy deposited in the gas by the ionization event and the region is called the ionization chamber. In this ionization region, the created charges do not depend on the applied voltage. At ARRONAX, BLMs work in this ionization region and details are given in chapter 4. At higher applied voltage, the electrons gain sufficient kinetic energy to produce additional charge carriers by ionization of the gas in their path. This is called the proportional region. In the Geiger-Muller region, free electrons gain enough energy to cause an avalanche of ionization reaching saturation point.

2.3.3 Examples of BLM

These examples are discussed based on the principle (gas ionization chamber) without investigating the beam energy, they are adapted for. There are several factors that must be taken into account before selecting a beam loss monitor design or type. Some factors are related to the type of radiation, expected dose rates, etc. and other factors related to reliability, physical space available, cost, etc. Another consideration is based on its output type i.e. current integration and pulse count. There are a few more factors that are required to check before using any type of BLM. These factors are BLM's sensitivity towards the magnetic field, background radiation, etc. Therefore, type of BLM at different accelerator facilities is going to be different consider-

ing all discussed factors. Let's discuss a few examples of ionization chamber-based BLMs at different accelerator facilities.

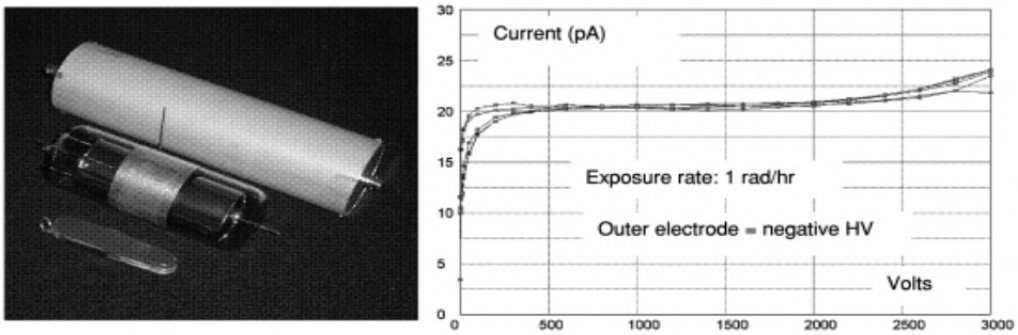

Figure 2.31: Argon ionization chamber and its container at FNAL on the left side and right side shows a saturation curve for five identical ion chambers taken with a radioactive source [52].

As an example of ionization chamber based BLMs, the Fermilab (FNAL) argon ionization chamber [52] is a conventional ion chamber developed for use around accelerators (see figure 2.31). It is a sealed-glass cylindrical chamber with 10 cm long nickel electrodes. Its volume is about 110 cm^3 which is filled with argon gas at 725 mm Hg pressure. The electron attachment rate to form negative ions for Argon gas is very small and about 0.5 $cm/\mu s$ is the electron drift velocity, thus giving a large prompt signal. The Ionization region of this detector ranges from 200 volts to 2000 volts.

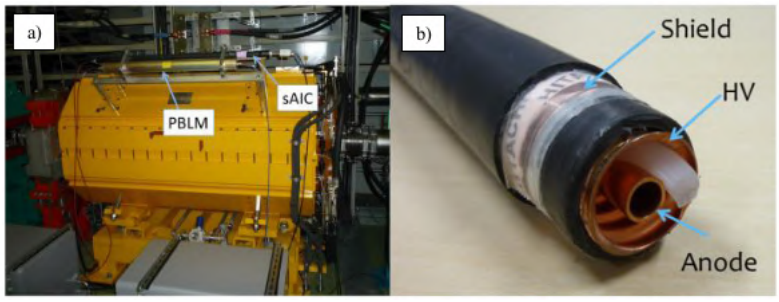

Figure 2.32: a) Installed PBLM and sAIC at J-parc. b) Cable structure used for air ionization chamber [53].

At J-parc ring [53], three types of BLMs have been installed (see figure 2.32) i.e. a cylindrical proportional gas chamber (PBLM), a 1 m long short-type air ionization chamber (sAIC), and a long-type air ionization chamber (longAIC) where PBLM is used as their main detector. PBLM offers a wide range in terms of gas gain and a very fast impulse response of approximately 0.1 μsec. For more details on PBLM [54]. sAIC and longAIC use a double-shielded 20D coaxial cable. A grooved Cu pipe acts as an inner shield core while spiral polyethylene

acts as an insulator as shown in figure 2.32. The center Cu tube picks up the charge, while the bias voltage is applied on the grooved pipe tube and the outermost Cu tape shield is grounded. sAIC and longAIC is 1 m and 84 m long, respectively. As sAIC sensitivity is higher so it is used in a high radiation environment where longAIC is to measure average beam power loss to ensure that the beam loss is lower than the threshold [53].

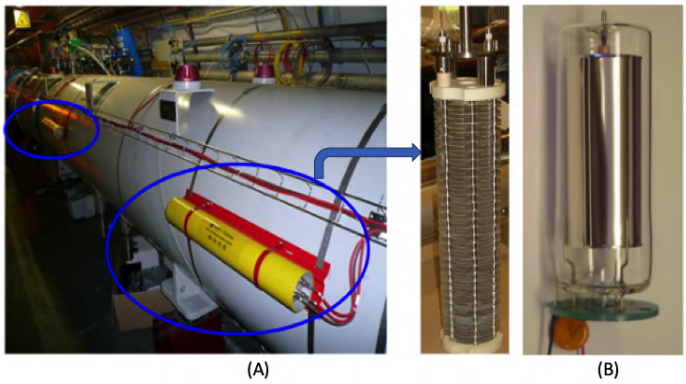

Figure 2.33: (A) Ionization chamber at CERN [55]. (B) Ionization chamber at SNS [56].

Parameters	CERN/GSI/IHEP/ESS	TEVATRON/RHIC/SNS
Time resolution (μs)	0.3	10
Gas	1.5 ltr N_2 at 1.1 bar	0.11 ltr Ar at 1 bar
Supply voltage (volts)	800−1800	500−3500
Dynamics range (A)	$10^{-12} - 10^{-3}$	$10^{-10} - 10^{-4}$
Leakage current (pA)	< 1	< 10
Collection efficiency (%)	90	77−92

Table 2.4: Comparison of ionization chamber performance at different facilities [56].

At LHC CERN, there are several types of BLMs that have been installed. Most of them are mainly based on ionization gas chambers. Nitrogen is used as a gas here. These ionization chambers have been developed at the Institute for High Energy Physics, Protvino, Russia, in 2006-2008, and currently are widely used in almost all accelerators at CERN, IHEP, ESS, and GSI. There are different types of beam loss monitors produced in CERN-IHEP collaboration.

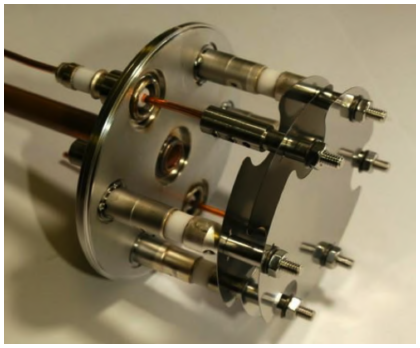

Figure 2.34: Secondary emission monitors at LHC [55].

These BLMs can be divided into four categories based on their purpose. The first category is parallel plate gas ionization chambers (see figure 2.33), which are installed at local aperture minimum and loss locations. The detector's active zone consists of 61 parallel electrodes with a 5.71 mm distance between them in the ionization chamber. As shown in figure 2.33, the ionization chamber at Tevatron, RHIC, and SNS accelerator facility is compared and their performance is summarized in table 2.4.

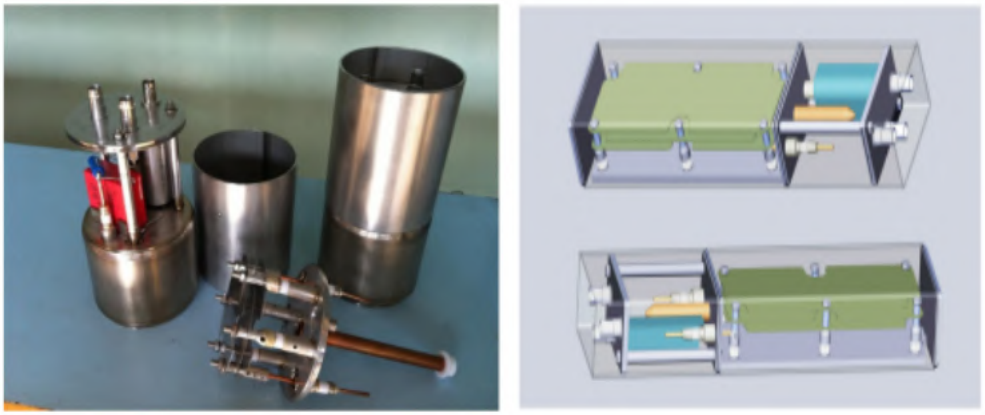

Figure 2.35: Left and right shows little and flat ionization chambers respectively at LHC [55].

The second category is secondary emission monitor [55] (see figure 2.34) installed at very high dose rates locations. The secondary emission monitor is characterized by fast response, low sensitivity, high radiation tolerance, high linearity and accuracy. The bias electrodes are made of Ti to make use of "Secondary Emission" yield stability. The sensitivity is about a factor of 3×10^{-4} smaller than in the ionization chamber.

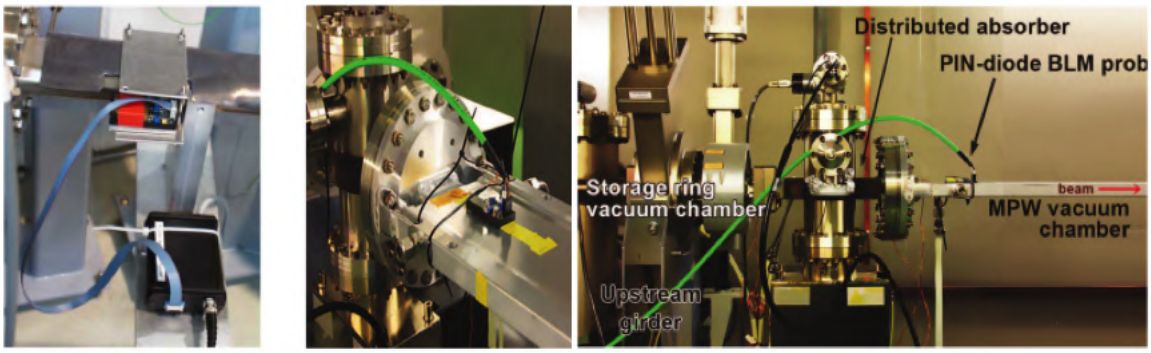

Figure 2.36: (A) Pin diode BLM at ALBA [57] . (B) Pin diode BLM at ANKA [58] .

Third and fourth categories (see figure 2.35) are little (LIC) and flat (FIC) ionization chambers, respectively. LIC [55] is designed to reduce the sensitivity to saturate for higher losses where FIC [55] is designed to geometry considerations. LIC and FIC active zone consists of

3 parallel aluminum electrodes and nitrogen filled with ceramics insulator secondary emission type. Another example of ionization chamber based BLM is the "Pin diode" solid-state or semi-conductor ionization chamber (see figure 2.36). These are mostly used in count mode. These BLM can easily fit in limited space due to their compact size. These BLMs are in operation in many accelerator facilities like SSRF [59], ANKA [58], ALBA [57] and HERA (DESY) [60].

These BLMs are developed and adapted based on requirements. In current integration output mode, BLMs based on very fast response, long ionization chambers for detection over certain longitudinal range, and utilization capabilities in very high dose rate region are discussed. In pulse count output mode, solid-state or semi-conductor based "Pin diode" BLMs are discussed that are very compact in size yet relatively expensive.

The choice of the BLMs within the first phase of usage, for the ARRONAX beamlines is based on several main reasons e.g. they have to:

- Be compact and adaptable to the various z-location along the beampipe. Due to tight location, the BLM footprint has to be limited to this few cm and should adjust easily and without modification to the existing beampipes.
- Also in case of major maintenance and due to the removal of some of the beampipes section, they have to be taken out and repositioned in a manner compatible with the radioprotection ALARA (As Low As Reasonably Achievable) principles.
- Be simple, robust and relatively light by design and materials. The BLM can be handled by one person and should require minimal maintenance once installed. Additionally, they can be manufactured by a mechanical workshop
- Be able to provide diagnostics capabilities such as transverse beam positioning.
- No fast response from the BLM is required i.e. they do not require to be PIN diode or even argon based sealed monitors.
- Need to be radiation resistant as some will be placed in production vaults.

Thus, the BLMs at ARRONAX have been chosen to be air-filled plane parallel ionization chamber built such that each quarter plate is automatically in place with respect to one another. For this the chamber is divided in two half “jaws” connected by a threaded shaft (see figure 3.5). The BLMs are designed such that the positioning can be done quickly and a single scroll wheel can be used to lock the BLM on the beampipe. Due to limited access possibility to irradiation vaults, robust BLMs are required that can be easily maintained. The design and dimension (3 cm longitudinal width of BLM) are chosen as it can be easily installed outside of a beam pipe

in the limited tight spaces when needed. In addition, it is designed to potentially indicate beam positioning as no beam position monitor is installed in the beamlines. These BLMs are adapted to ARRONAX high-intensity beamlines during the course of this work.

In this chapter, we have covered bibliographical background of the work mainly focused in this thesis. The experimental environment, simulation tools used, methodology, and data acquisition system is described in the next chapter.

Chapter 3

EXPERIMENTAL ENVIRONMENT AND METHODOLOGY

The thesis is focusing on studies related to beamlines and on their preparation for the future developments of beams (at higher intensities). The beamlines are equipped with several electromagnetic elements that form the beamline lattice, to guide the beam from the cyclotron to the target. Beamline lattice design depends on the need of focusing and bending elements to transport or transfer the beam with quality or desired beam optics. A beamline element design depends on the characteristics of the beam. Beam's size and divergence are very important factor to decide focusing requirements. Accordingly, focusing elements are being designed to accommodate the beam in the limited space of the vacuum chamber or beam pipe. Beam diagnostics chambers are always installed in a beamline. In these beam diagnostics chambers, one can put instrumentations to diagnose the beam such as Faraday cup, beam profiler, beam loss monitor, etc. All mentioned instrumentations have been discussed in the previous chapter except the Faraday cup. Faraday cup serves mainly three purposes listed below:

1. It measures beam current at a location along the beamline. It is designed to measure currents of low energy beam. So, it can also be used as a beam tuning device by comparing beam current measurements at several Faraday cup locations. One can tune the electromagnetic elements to attain maximum transmission.

2. It safeguards machine during any emergency, Faraday cups are often used as a beam dump to stop the beam. Some facilities along with ARRONAX use an alarm system to trigger the Faraday cup automatically.

The diagnostic chambers have limited space to house specific instrumentation. The diagnostics installed on or outside the beam pipe have been considered: External (to the beam pipe) air ionization chamber based BLM has been developed, based on the initial iThemba labs BLM design. The base for the initial design was the chambers located in the vacuum of the beam pipe. Several question arised following the new design for Arronax such as their mechanical adaptation to the beam pipe, their abilities to measure current behind the Aluminum pipes. In this chapter, we will discuss BLM's geometry and the BLM tests are detailed in the following chapter 4. Later on, Experimental measurements, as discussed in chapter 5, have been done

with this BLM and the instrumented end-line collimator. The experimental physics and industrial control system (EPICS) is used for data monitoring and acquisition of several hundreds of parameters from the cyclotron. For the present work, BLMs are also being integrated within EPICS network and will be discussed below.

To study beam dynamics at ARRONAX high-intensity beamlines, the quadrupole current variation technique has been used to study ways to reduce beam losses, transverse beam emittance, and off-centered beam. Quadrupole scans have been performed with several beamline settings, including modifications of the settings of stripper foil azimuthal position, of the injection, cyclotron and, dipole strength to study the impact on the beam at the end-line instrumented collimator.

G4Beamline simulations have been implemented for better interpretation of the experimental results and to study transverse beam dynamics behind it. In this Chapter, we will be discussing the general experimental environment, quadrupole scan technique, and G4Beamline simulations.

3.1 Beamlines and Beam Tuning at ARRONAX

ARRONAX C70 cyclotron has in effect two types of beamlines, depending on their usage and the termination at the end-of-line. The first type is with an irradiation station that can house a rabbit, encapsulating a target, and is used at intensity above 1 μA. This type of beamline is mainly used for production of radioisotopes. The geometry of the BLMs is specifically suited for this line and will be used for the final experiments. The other type, such as the AX beamline, with a kapton foil at the end-of-line is used for irradiation below an average intensity of 1 μA. This operational restriction is mainly due to the heat load limit of the kapton foil and the need to keep the vault with a minimal activation level.

The second type (AX) have been used for the preliminary tests of the BLM and checks, with an already installed wire profiler, on the quadrupole intensity variation techniques described later on. Both types of beamlines are presented below.

3.1.1 High intensity beamline

As shown in figure 3.1, high-intensity beamlines is approximately 10 m long and consists of first a bending magnet (or switching magnet), close to the cyclotron which is used to curve the beam in the selected beamline. It is followed by a x-y steerer, e.g. a 490 mm long dual plates horizontal/vertical magnet. The steerer can be used to readjust the centering of the beam on the collimator described below. One pair of 256 mm long (effective length) quadrupoles is located in the cyclotron vault and upstream the 3.7 m thick wall. The 110 mm of diameter beampipe passes through the wall up to the irradiation station vault. There, 100 mm away from the wall, it is connected to another 105 mm of diameter Aluminum beampipe. 30 mm away (see chapter 4) a first BLM is installed and one meter away of the last quadrupole a second BLM is fixed around the beampipe. Upstream the irradiation station, a four fingers instrumented collimator (described later on) is used to limit the beam dimension. Multi-layer tantalum faraday cups are also installed along the beamline and serves as beam intensity measurement checkpoints as discussed in the machine tuning section.

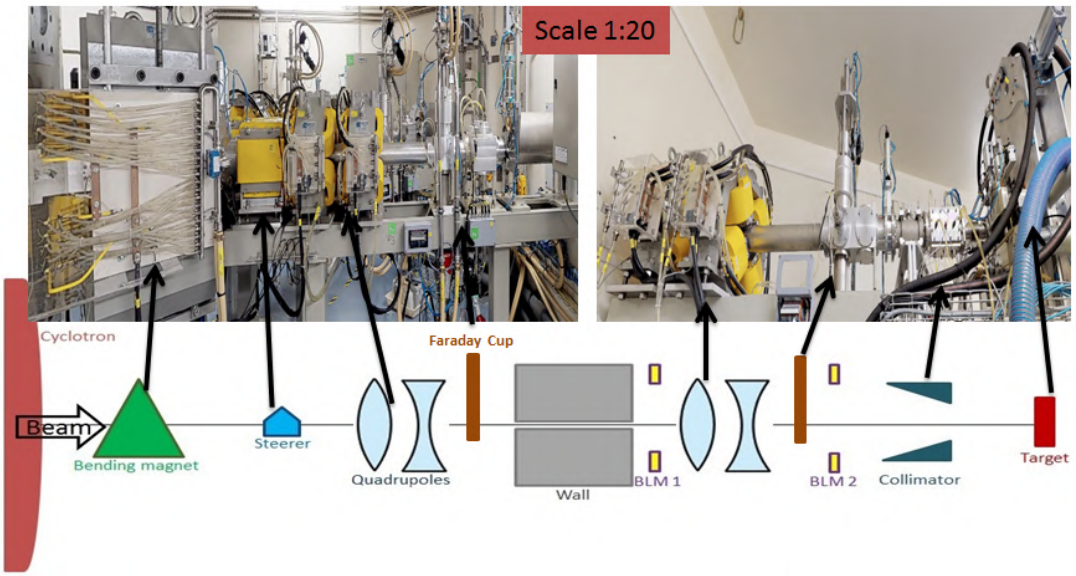

Figure 3.1: High-intensity beamline layout.

3.1.2 Low intensity beamline AX

The low-intensity beamline differ to the previous one as they are ended by a 20 mm of diameter and 75 μm thick kapton foil. The beam passes through the vacuum to the air and downstream various experiments that are being aligned in front of the beamline. This beamline has been

used at low intensity for the preliminary test on the BLM and with the wire profiler. As shown in figure 3.2, it consists of three pair of quadrupole (similar to the one of the high-intensity beamlines), a steerer, and a first bending magnet. A second bending magnet is used to guide the beam in each final beamline non-concurrently. A single wire Profiler is located upstream the 10 mm aperture four fingers instrumented collimator.

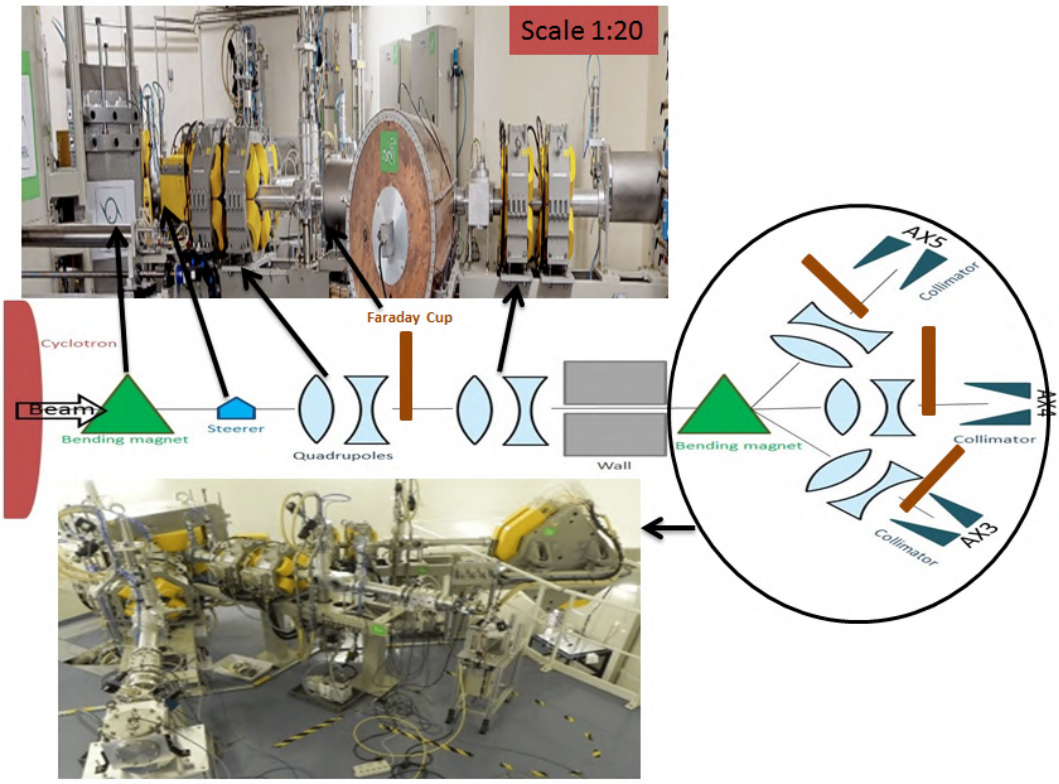

Figure 3.2: Low intenisity beamline layout.

3.1.3 Machine Tuning

For machine tuning, ARRONAX has developed various libraries with injection, cyclotron, and beamline settings. These libraries are optimized for different isotope production and also for different ion beam. Operators upload these libraries and further optimize machine settings based on the transmission rate which is measured by Faraday cups installed at different locations. There is one Faraday cup in the injection line and a radial probe inside the cyclotron dees to measure beam current. Operators compare injection Faraday cup and radial probe measurement and optimize injection settings to have a better transmission rate. Beam extraction and beamline setting optimization is being done using two Faraday cups in beamlines. One is placed downstream of the extraction section which can be used to optimize extraction and

switching magnet settings. A second Faraday cup is installed upstream of the collimator which can be used to optimize other beamline settings. But to optimize beamline parameters like focusing elements, Faraday cups are not enough. At ARRONAX to optimise the last pair of quadrupole (see figure 3.1) special instrumented collimator is implemented which will be discussed in section 3.2. There is a drift space of approximately 3.5 meters between the first and second pairs of quadrupole (see figure 3.1). Due to large drift length, high beam envelop size is highly possible. A large beam envelope can cause huge losses and can damage sensitive locations at the junction upstream of the last pair of quadrupoles. The junction is an o-ring type sealing (rubber-based) so high losses can damage the sealing. It can create an issue from vacuum's (order of $10^{-6}\ mbar$ at ARRONAX) point of view. Therefore it is essential to put some beam diagnostics in order to optimize the first pair of quadrupole settings. For that purpose, BLM is built which will be discussed in section 3.2.

3.2 Instrumentation

Initially, ARRONAX beamlines were equipped with an instrumented collimator only installed at the end line. A Collimator has a dynamic graphic user interface (GUI), as depicted in figure 3.3, which shows online particle deposition. This GUI is used by operators to tune the last pair of quadrupole and to center the beam. After testing BLMs, two BLMs have been installed on high-intensity beamlines.

Figure 3.3: Dynamic operator interface of particle depositions on each fingers of the collimator.

3.2.1 Collimator

The four fingers collimator of Arronax are used to limit the size of the beam upstream the target. Several type of collimators are in use at Arronax: Their aperture, material, ending is adapted to the beamline needs. The collimators are approximately 222 mm long and made of Aluminum or copper as shown in figure 3.4(A). In the photograph, a terminating tungsten nose serves as support for the rabbit containing the target. Their inner aperture, as shown in figure 3.4(B), is tapered over 150 mm with an angle of 11° such that power deposition is diffused longitudinally. Electrical deposition on each fingers are individually measured.

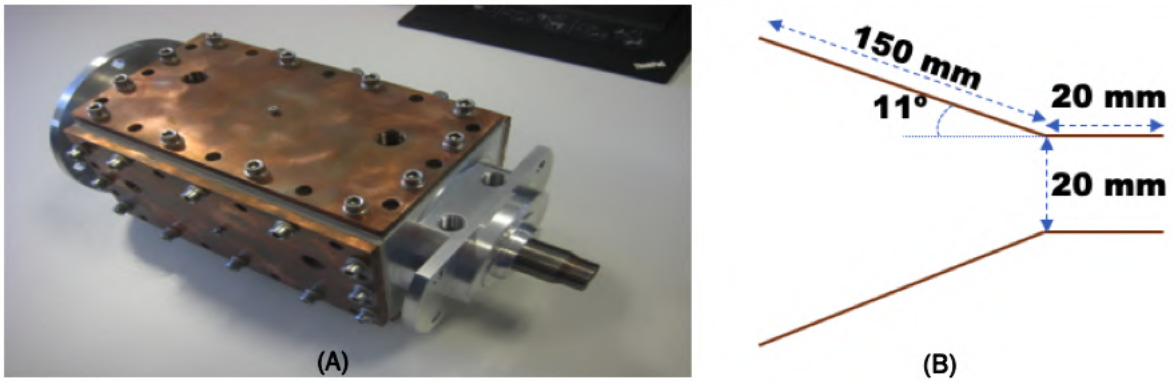

Figure 3.4: (A) Physical appearance of a copper collimator (B) The inner geometry of the collimator at ARRONAX.

The electric deposition of each finger is recorded and archived in the data processing of EPICS that is described in section 3.5.

3.2.2 Beam loss monitor

We have discussed BLM with different physical appearances and working principles in chapter 2.3. It has four active plates in all four directions similar to the collimator. It works on the principle of "gas ionization detectors" which is already discussed in section 2.3.2. It can be installed in the limited space around a vacuum tube (see figure 3.5) as the hollow circular section of the BLM fits over the beam pipe in high-intensity beamlines. The system consists of a total of five channels: four channels are connected to the active plates and one is for the supply voltage. A kapton foil is placed, acting as an isolator between BLM and beam pipe.

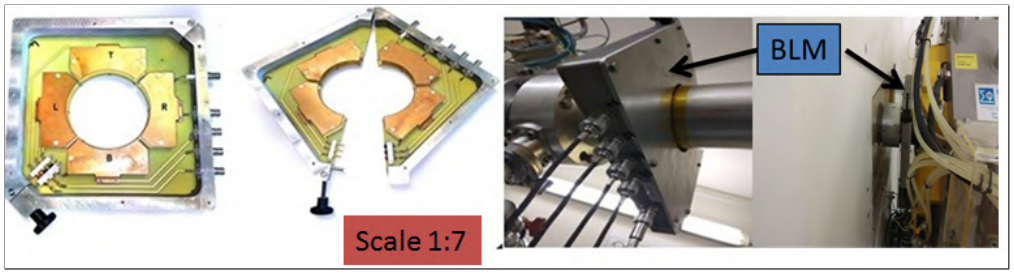

Figure 3.5: Physical shape of BLM at ARRONAX.

3.3 Quadrupole Current Variation Technique

If the beam centroid is not matching with the quadrupole's magnetic center, the resulting dipole component kicks the beam. If the gradient of this quadrupole is varied, this kick causes a change in the beam trajectory. It is a very useful technique to study beam dynamics in such industrial accelerators. As mentioned earlier, experimental results are at BLM and collimator level. So let's discuss quadrupole scan results and the method implemented to calculate local beam size and beam positioning.

By varying the quadrupole strength, the outcome of the transfer matrix will change as given by equation 2.13 for the y-focusing quadrupole. This change in the outcome of the transfer matrix can be translated into beam envelop size or focal point (see figure 3.6). Therefore, the proton deposition at the collimator will also vary during a quadrupole scan. The same applies to beam loss measurements at BLM.

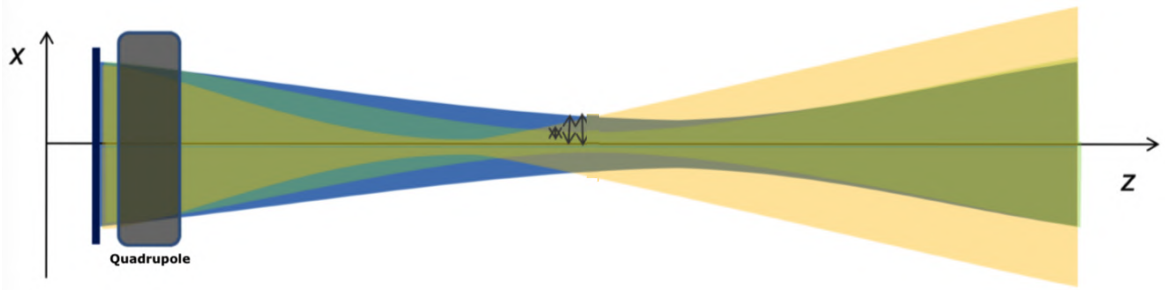

Figure 3.6: Beam envelop during a quadrupole scan in horizontal plane (X-axis) and the beam is moving along Z-axis.

Local beam size and positioning: By definition, it is the beam size and positioning at the location of BLM or collimator. Beam positioning measurements have been performed at the collimator level. The local beam size is a sum of electrodes response (measured current) of a BLM or collimator in horizontal or vertical plane. As shown in figure 3.7, the result of a

quadrupole scan is of parabolic shape (explanation is detailed in section 5.3.1). A beamline should be tuned and stable for a quadrupole scan to reduce kicks. Besides, a reference is also required to normalize experimental results for comparison. Therefore, a stable response of the "total beam current or intensity" and low difference of collimator depositions (positioning) in a plane are being considered as a valid and a better quadrupole scan. The total beam current is the sum of the total response of collimator and target. The stable response of "total beam current" ($\pm 5\%$) is considered as an indication of a tuned beamline with stable beam. This total response is being used to normalize the experimental results performed at different beam currents or time. If the experiment is being performed at two different beam intensities then the response will be higher at higher beam intensity compared to the lower one. So, the normalization factor should be greater than 1 to scale up the data of the experiment done at lower beam intensity. It has been done to normalize both results at the same level. Thus, the total beam current of both results is being divided depending on the need to scale up or scale down data. This factor is then multiplied by local beam size data for comparison. The other option to normalize quadrupole scan results is to divide "total beam current" with local beam size or local beam positioning data in a plane. This will normalize results at 1 μA level.

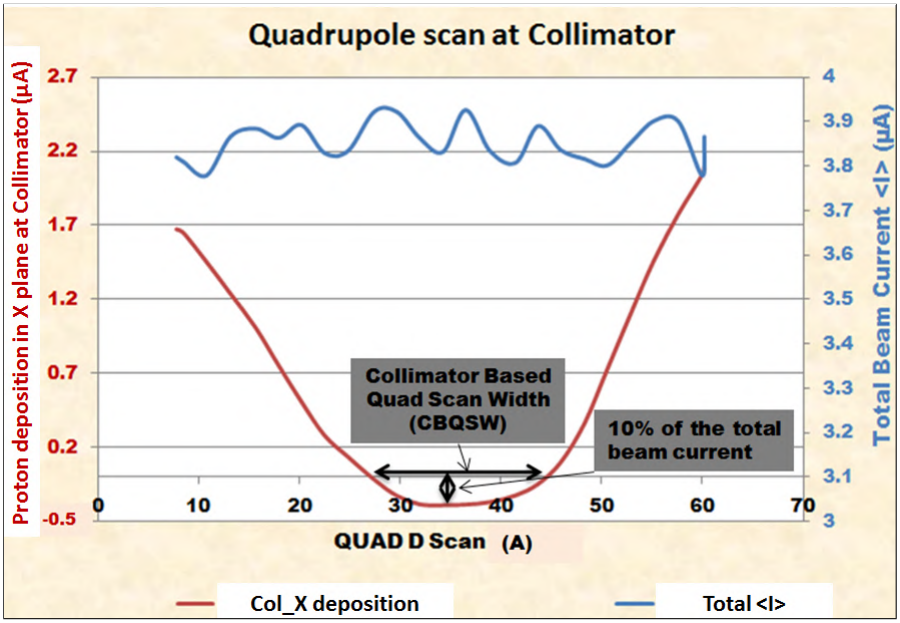

Figure 3.7: An example of a quadrupole scan result of a local beam size at collimator (for detailed explanation, see section 5.3.1).

One can see the negative current at the collimator during a quadrupole scan. This is a calibration offset and ideally, this is approximately 10% of the total beam current (experimental observation). In a tuned machine, it has been observed that the offset varies from 8% to 10% in

time. But "Collimator Based Quad Scan Width" (CBQSW) is always measured at 10% of the total beam current offset level. This is illustrated in figure 3.7. The significance of "CBQSW" is detailed in chapter 5. It is measured in terms of Amperes. From experimental observations, it has been found that CBQSW in horizontal plane depends on vertical positioning but does not depend on horizontal positioning. A variation of $\pm$ 0.4 A in CBQSW has been observed under $\pm$10% change in the vertical positioning displacement (see figure 3.8) when compared on the same day. Also, there is an uncertainty of $\pm$ 0.5 A in the measurements of CBQSW due to hysteresis effect of scanned quadrupole magnetic field. To counter this uncertainty, CBQSW is always measured for descending quadrupole settings.

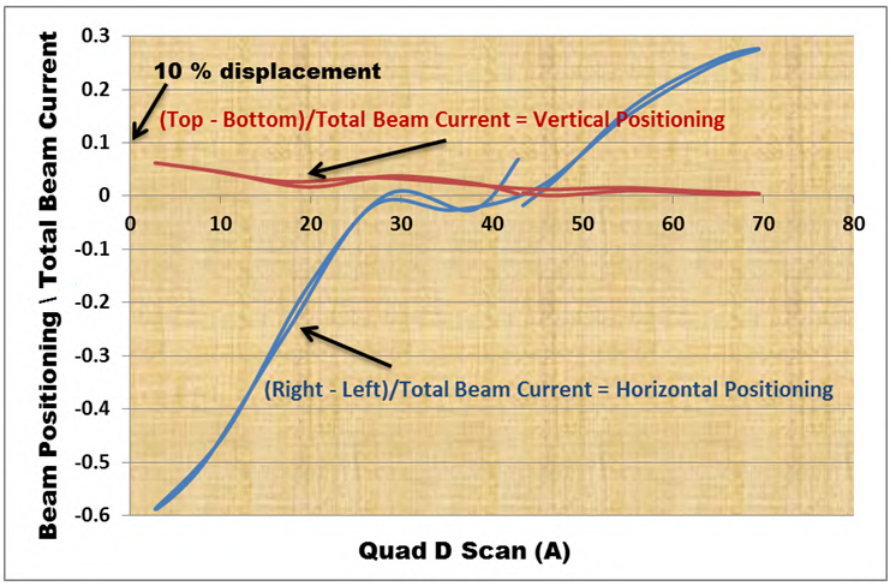

Figure 3.8: An example of a quadrupole scan result of beam positioning at collimator.

At ARRONAX beamlines, the vertical positioning is very stable and close to y=0 line (less than 5% displacement) during a quadrupole scan. For beam positioning, the response of two facing electrodes at collimator is being subtracted and divided by total beam current. The negative sign shows the beam is towards left in the X plane and bottom in the Y plane. This is illustrated in figure 3.8. In this figure, one can see hysteresis loop as this scan starts and finishes at 43 A quadrupole setting. At first, the quadrupole is scanned in the ascending order till 70 A then, is descended to 2 A and is brought back to initial setting i.e. 43 A.

A scintillator sheet or scintillator based halo detectors [97] can be used to validate BLM's transverse beam positioning indication, by placing them at the end-of-line. These sheets can deliver informations on the centre-of-mass, the width and the intensity of the beam. However, this solution can not be used as collimator is placed at the end-of-line. Thus, BLM's potential

(by geometry) to indicate beam positioning can be studied experimentally with beam position monitors (BPM) installed in lines. But BPM is not installed at the time of writing. Therefore, this has been studied in simulations where BLM beam positioning is compared with collimator's and is detailed in chapter 5.

3.4 G4Beamline Simulations

G4Beamline [63, 64] is a single particle tracking simulation tool that is based on Geant4. It is optimized for simulating beamlines. It is a very user-friendly tool and does not demand C++ programming skills. Its simulation code can be described in a single ASCII file or text file. Code language is self-explanatory which can be understood by anyone experienced with beamline simulations. It is also integrated with advanced visualization capabilities. By using external programs like HistoRoot or Gnuplot, histogram of the data under close observations can be done.

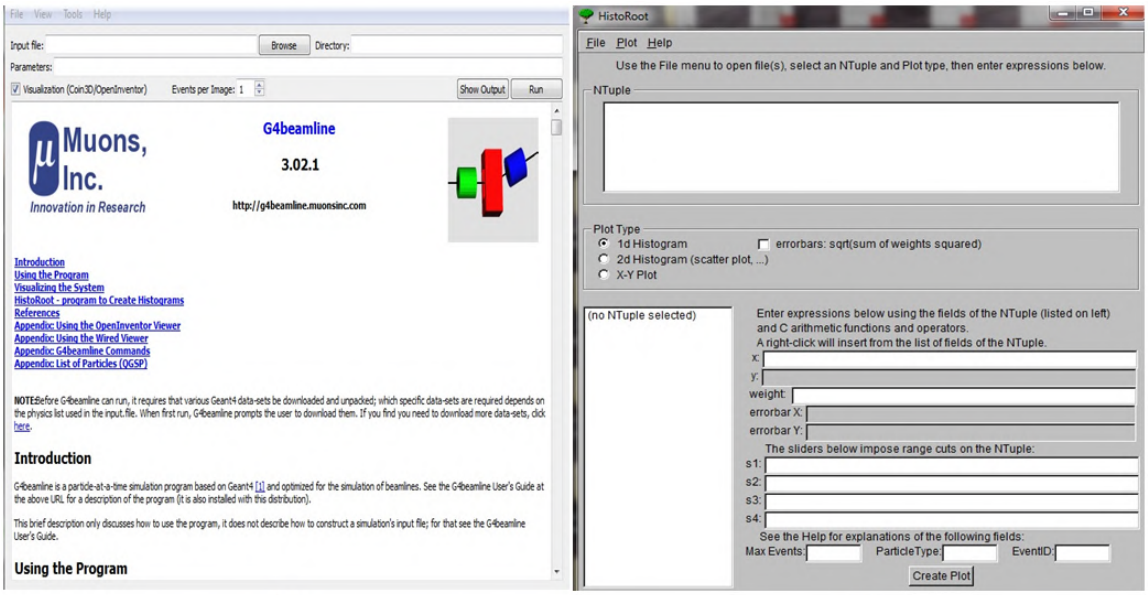

Figure 3.9: (A) G4beamline user interface with manual. (B) Historoot

It is possible to define any general object like a box, cylinder, etc of any dimension, material, or electromagnetic properties. Object placement is accurate to 2 nanometers in tracking which is far more accurate than real placements of any element. In addition, collective effect computations are also possible such as space charge effect. All Geant4 physics lists can be used here. The magnetic elements such as dipole, quadrupole, etc can be defined and implemented

by using predefined “Generic” components. Real magnets have fringe fields, G4Beamline simulation can also model them. The model is based on that in cosy infinity (the first arbitrary order beam physics code [62]). Despite the very high detailed level of G4Beamline simulations and its accuracy, there will always remain a certain degree of uncertainty in any simulation tool.

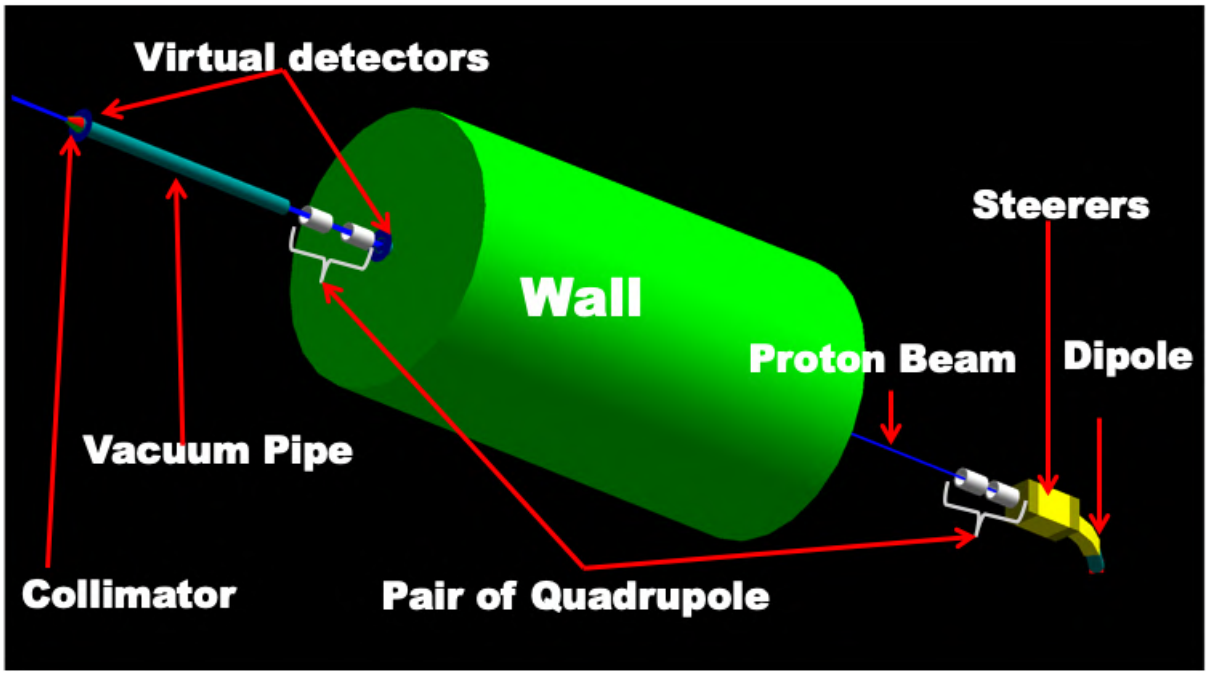

Figure 3.10: G4beamline simulation model of the high-intensity beamline at ARRONAX (see the code in appendix B.1).

In this thesis, the G4beamline simulation tool has been used to simulate beamline lattice with a 70 MeV proton beam. In figure 3.10, the model of high-intensity beamline is shown which is used to support transverse beam dynamics studies. This model includes 70 MeV proton beam, dipole, X-Y steerers, two pairs of quadrupoles, a wall, a vacuum pipe, virtual detectors or beam loss monitors, and a four-finger collimator. Mechanical dimensions and placements of all elements are kept identical to high-intensity beamlines at ARRONAX. The best suited Geant 4 physics library "**QGSP_BERT**" is being used for theoretical analysis. **QGSP_BERT** is the physics list most recommended for high energy physics (HEP). The material definition includes chemical composition and density of the actual material allowing to simulate more realistic material. A Gaussian beam has been used with initial particle spread and divergence in the X-Y plane provided by IBA. The momentum spread has been assumed to be 0.1%. Changing the maxStep size (the equation of motion will take multiple integration steps within this step size before reaching to a final solution) makes no noticeable difference but takes much longer to simulate. So, maxStep from 1 mm to 10 mm is being used depend-

ing on the element. As mentioned, real magnets have fringe fields, and G4beamline makes an attempt to model them. A "**genericsectorbend**" is a command for simulating a generic bending magnet just like switching magnet at ARRONAX. Its argument includes "**fringeFactor**". There is a bug in the G4beamline version 3.02.1 used here.This genericsectorbend is nontunable due to the presence of an extra dipole field (bug). This bug can be removed by creating and copying the magnetic field co-ordinates of genericsectorbend for a specific user defined parameters. Hence, the manipulation of parameters is only possible by repeating this whole process that consumes a lot of time. The studies in this thesis often require manipulation of dipole field to study impact on beam at the end-line collimator, losses, beam alignment, etc. Therefore, an "**idealsectorbend**" command has been implemented in the code instead of genericsectorbend. An idealsectorbend does not have fringeFactor argument. However, comparative studies indicated that the fringeFactor of bending magnet does not play an important role at the level of analysis discussed in this thesis. The quadrupole of any shape can be simulated with "**genericquad**". The above discussed bug is not seen in this command. So, the calibration data of the quadrupole field in high-intensity beamline is being compared with simulated quadrupole field in order to find the best possible "fringeFactor" in simulations. The fringeFactor (f) best fitting the calibration data is found to be equals to 0.7. This is shown in figure 3.11 where S_By and M_By are the simulated and measured quadrupole magnetic field (calibration from the manufacturer "SigmaPhi"), respectively. The x-axis shows the field length of a quadrupole magnet. The figure on the right side shows that the ratio of magnetic field (simulated/measured) is close to 100% over the field length but also shows some discrepancies where the magnetic field is smaller.

A "**virtualdetector**" is an ideal detector that detects every track that comes in or hits it. It also measures all of the track properties like position, 3-momentum, particle type, eventID, etc. Similarly, a "**detector**" command can also do the same operation. These commands have been used to simulate beam loss monitor and collimator. A "**zntuple**" is also a similar command which can be used to track the beam over a range of z-coordinates (beam direction). The measurements for all such tracks are output to a root or text file as an NTuple. This file can be used for further analysis or to plot data in historoot.

The number of particles or events directly impact the computational time. The work, presented in this thesis uses most of the time 10000 events to keep high initial statistics and the

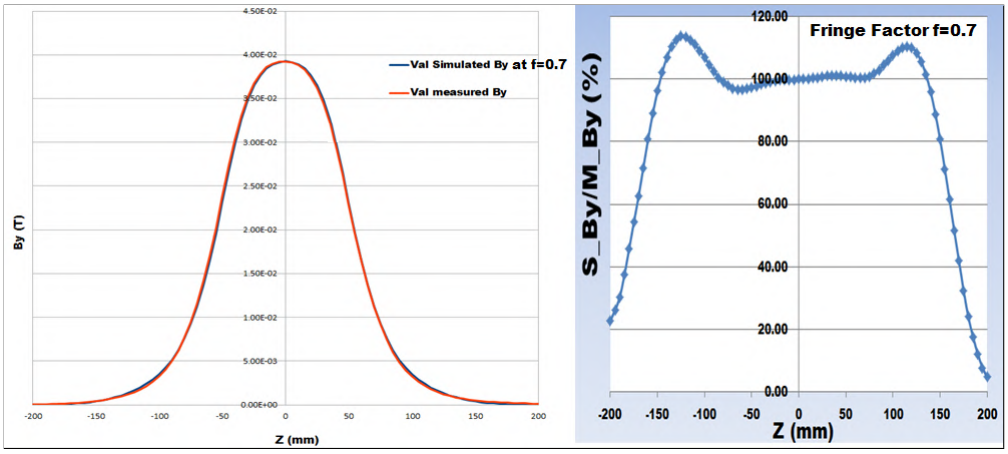

Figure 3.11: The figure on the left shows measured and simulated (f=0.7) field length as a function of quadrupole field in Tesla. The figure on the right shows field length as a function of the ratio of simulated and measured quadrupole field (%) at f=0.7.

computation time suitable. A proportionality has been observed when results have been compared with those obtained with one million events. This means proportional increase or decrease in the number of deposited particle during a quadrupole scan at collimator w.r.t. the no. of input events. Therefore, 10000 events are sufficient for most of the analysis. In few simulations like beam profile or trajectory measurements or secondary particle studies at least 30000 events are needed for statistical studies. In the context of the work presented here, statistical studies in simulation is the term referring towards a direct comparison of experimental data with simulation results using inputs from the experiments such as beamline element settings. A "**profile**" command in the code return a text or root file with beam profile measurements like particle spread, divergence, transverse emittance in the X-Y plane with respect to beam movement coordinates. For secondary particle studies (proton interaction with matter), "**kill**=0" is implemented with a minimum of 30000 events and a maximum one million. This kill command defines how the particle will interact with matter and 'kill=1' means the particle is simply getting killed without any further interaction with the surface. All the electromagnetic elements should be at kill=1. "As there is no field inside the 'iron', this can result in gross tracking errors for particles in the iron and implies that kill=1 is desirable.

3.5 Data Acquisition and Monitoring System

Previously, single Beam Loss Monitor (BLM) were connected with a "lab-view" [16] system which allowed tracing and saving data. The system was an unsynchronised standalone acqui-

sition for a single beam loss monitor. Lab-view saved data that can only be accessed offline. Later, it has been added an EPICS (Experimental Physics and Industrial Control system) [82] framework to the accelerator data acquisition system with the CS Studio platform to monitor data online. Later, BLMs have also been added with EPICS integration. This is being done during the course of thesis work.

3.5.1 EPICS and Control System Studio

EPICS is a protocol to exchange data between various types of control systems and data handling. The CS-Studio (CS-Studio) is a development tool which allows to build operator interfaces within the EPICS environment. Both are being adapted at ARRONAX.

General aspect

EPICS is a set of libraries and open-source software tools. It is globally used to create real-time control systems for scientific machines like particle accelerators, computer numerical control machines (CNC Machines), telescopes, etc. EPICS was initially developed and introduced as the "Ground Test Accelerator Controls System" (GTACS) at Los Alamos National Laboratory (LANL) in 1988 by Bob Dalesio, Jeff Hill et al [61].

As shown in figure 3.12, Epics uses publish-subscribe and client-server techniques (delivers a copy of each event to all its receivers like a message) to communicate between computers. The “input/output controllers” (IOCs), control and collect data in real-time, using the measurement devices or instruments attached to the server. This information is then provided to clients connected with the server, using pvAccess networking protocol or the high-bandwidth Channel Access (CA) which is designed to suit real-time applications such as scientific experiments. The IOC controls and runs a database of "records", which represent either devices or aspects of the devices to be controlled. Data in the database of records are represented by unique identifiers, known as Process Variables (PVs). These PVs are approachable over the channels provided by the CA or pvAccess. Different types of records are available based on the type of data or functional behavior (e.g. array, input, output, calculation, analog, binary, etc). Custom records can also be created. All types of records are listed in the EPICS record reference manual with its possible fields. Each record type consists of a set of fields, which specify data properties.

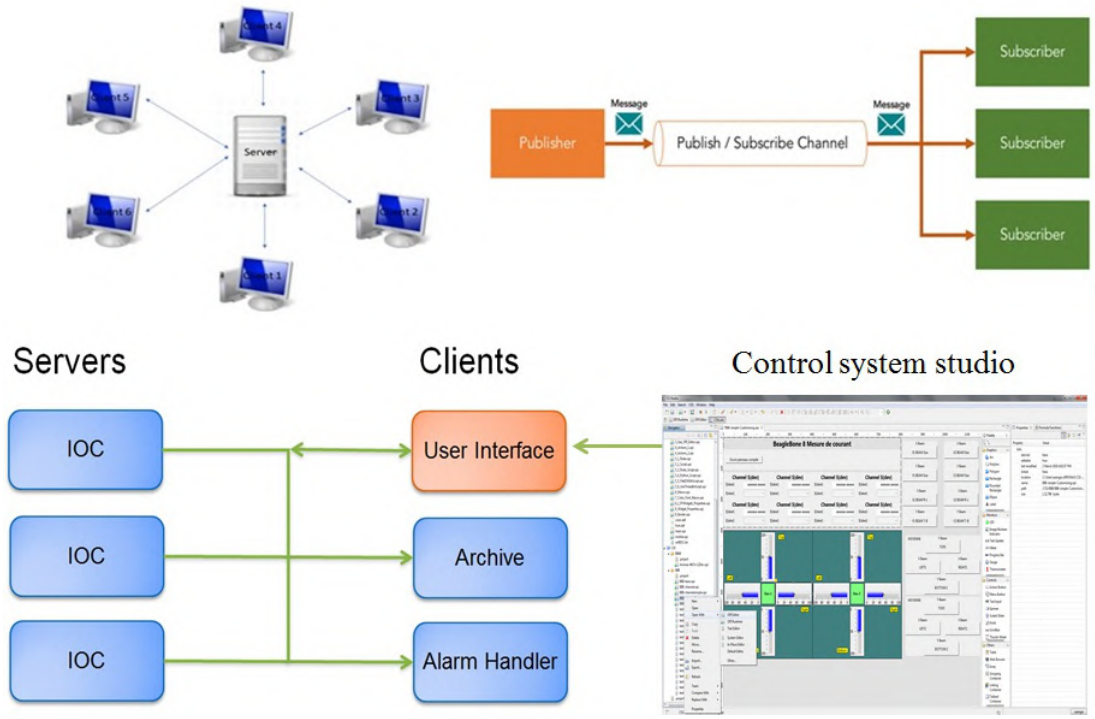

Figure 3.12: EPICS architecture

In the EPICS system, data is synchronized with control system's computer time . Therefore, all devices should share the exact time to avoid any time delay between the main server and clients.

The incoming data from numerous archived PVs is often large and to make data retrieval easier and faster, data is stored in three stages (see figure 3.13) described below:

- **Short term store (STS)** – It keeps most recent data or data for a day.
- **Medium term store (MTS)** – It stores recent data of couple of days.
- **Long term store (LTS)** – It stores the rest of the data.

Each appliance has 4 processes (see figure 3.13); these are J2EE WAR files and are deployed on separate Tomcat [89] containers described below:

- **Engine** - This component establishes EPICS Channel Access monitors for each PV in the appliance. The data is written into the STS. This component is based on the CS-Studio engine.
- **ETL** - This component moves data between stores that is, it moves data from the STS to the MTS and from the MTS to the LTS.

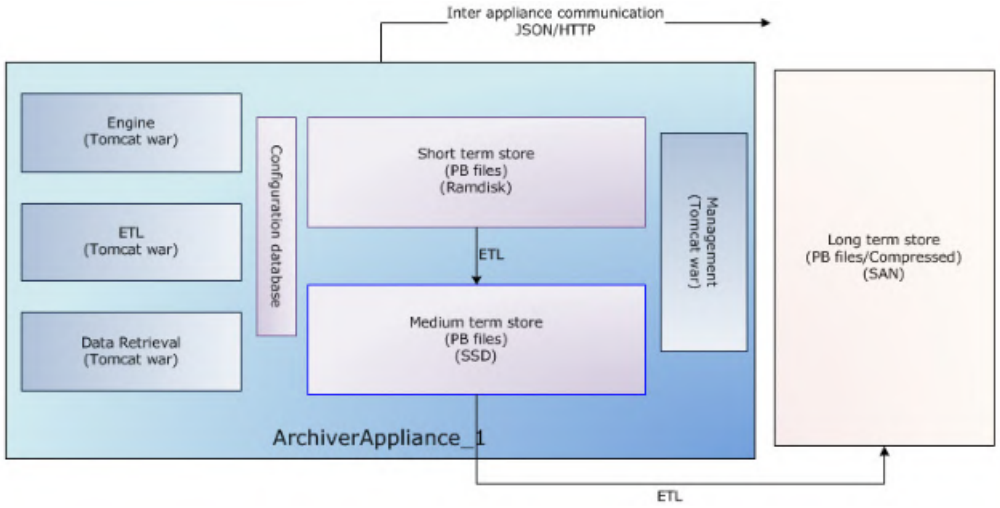

Figure 3.13: Multi storage system of Appliance archiver [65].

- **Data retrieval** - This component gathers data from all the stores, stitches them together to satisfy data retrieval requests.
- **Management (Mgmt)** - This component manages the other three components and holds runtime configuration state of archived PVs.

Control system studio (CS-Studio) [81] is a graphical user interface package that allows users to interact and view with PV data through typical display widgets. CS-Studio is an Eclipse-based collection of tools to operate and monitor large scale control systems. It can read or write PV values by implementing the pvAccess protocol. Its "operator interface" (OPI) can be customized to facilitate operators to monitor online data easily. Even online data can be monitored in the form of live plots. It is also possible to do mathematical or conditional operations with the PVs by adding and saving python or java code in the OPI editor mode of CS-Studio (see Fig. 3.12).

EPICS network and CS-Studio at ARRONAX

ARRONAX has implemented a dedicated network for EPICS environment. The CPUs of various control system is connected with control room's server (linux based computer) via IP address as shown in figure 3.14. In the server computer, EPICS is installed that comes with a web-based system called "EPICS Archiver Appliance" which was first developed by a collaboration of SLAC, BNL, and MSU. It allows users to archive millions of PVs. It mainly focuses on data retrieval performance. This web-based user interface allows to make changes to the

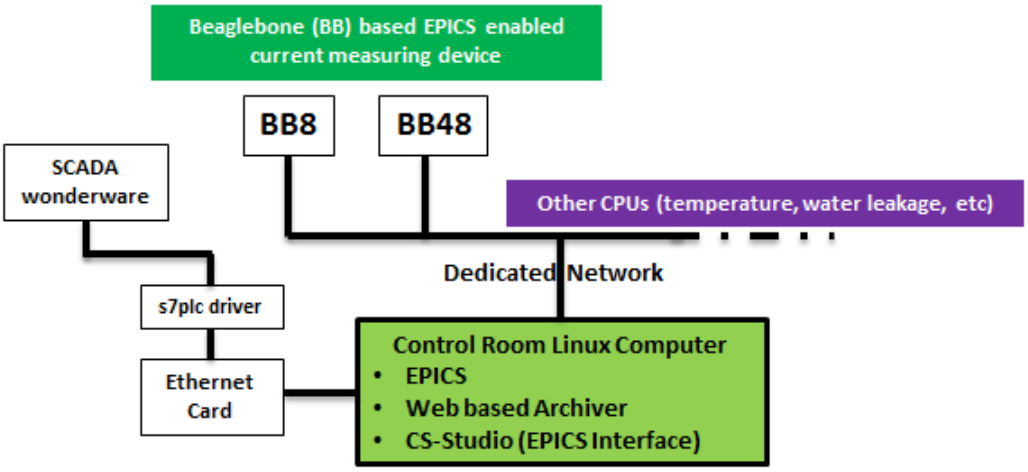

Figure 3.14: EPICS network at ARRONAX.

archived PV configuration without restarting the system. At ARRONAX, total 953 PVs (at the time of writing) are archived so the incoming data volumes are also large (0.93 GB/day).

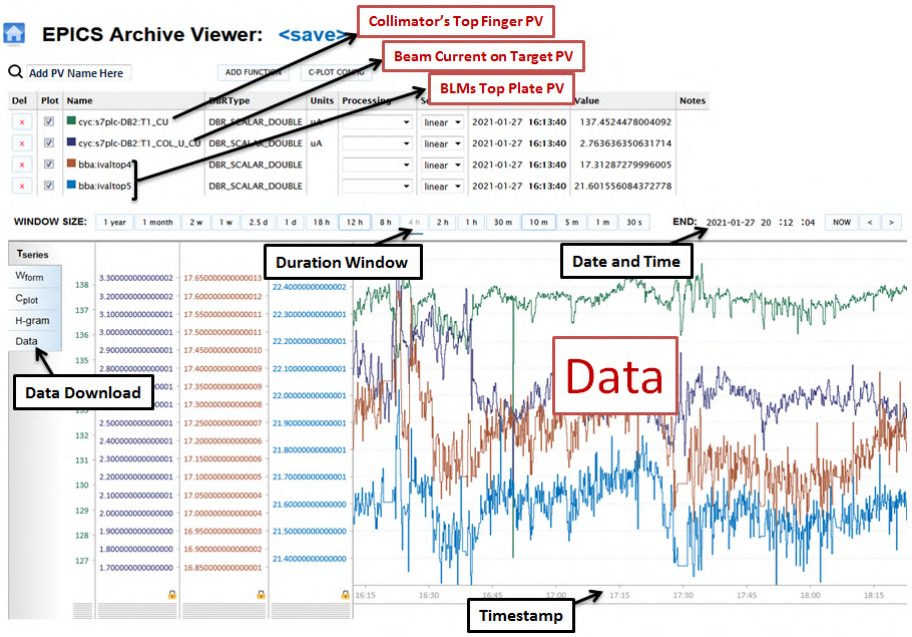

Figure 3.15: An example of web based user interface to browse and retrieve data at ARRONAX.

It also comes with plugins for the archive viewer as shown in figure 3.15. One can retrieve data from any archived PV or multiple PVs like in this example 4 PVs are shown. The PVs in green and violet color are the unique identifier name of collimator 's top finger and target's beam irradiation current, respectively. These PVs are integrated in the control system module of C70 cyclotron which is based on a Siemens s7plc board (see figure 3.14). The other two PVs shown in brown and blue color represents two different BLM's installed on the same high-

intensity beamline. The integration of BLM devices with EPICS is being performed during the course of this thesis work (detailed later on). These BLMs are now connected with 48 channel beaglebone (BB) EPICS enabled current measuring device (see figure 3.14) and are monitored on regular basis. The data can be viewed and downloaded according to manually entered date/time, and duration window (time range).

CS-Studio is installed in the control room's linux computers (see figure 3.16). This interface is being used by operators to monitor online data and to manipulate machine control systems using OPIs. The main control of the accelerator, machine protection and its environment (e.g. vacuum pumping, target transfer, etc) is based on Intouch from Wonderware. It shares its data through an Ethernet card. For more details see paper [69].

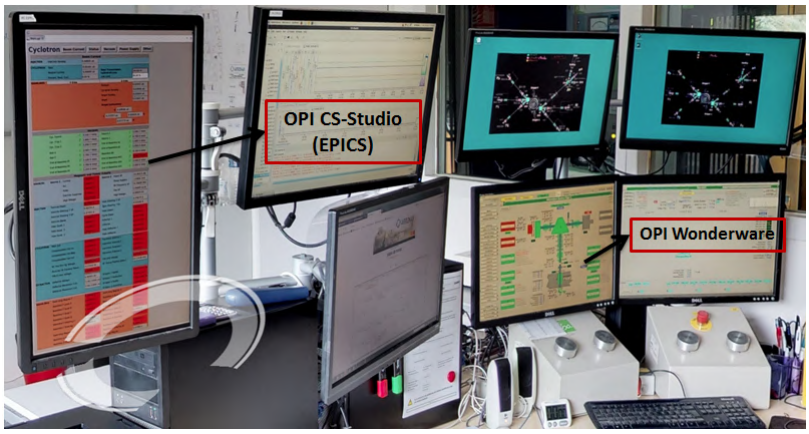

Figure 3.16: Control room at ARRONAX.

The interfaces or tools are being developed during this work either for BLM data monitoring or for online monitoring of experimental data. The BLM data monitoring interfaces are developed to facilitate operators data monitoring experience. The tools for experiments such as 'quadrupole scan related' are developed to monitor instrumental data (BLM or collimator) directly synchronized with quadrupole current settings.

Tools developed during this work

The OPIs, developed in CS-studio specifically for the BLM, are shown in figure 3.17. The OPI On the right shows the beamline in operation with its BLM data in the X and Y planes. This X-Y plane data is displaced by defining a local PV. This local PV is attached to a python script. This code is adding principle PVs of BLM's active plates facing each other. We call this X-Y plane data as 'local beam size' in X and Y plane at that BLM location. The OPI on the left

is developed to control the BLM and their power supplies. The device used here for power supply is from 'CAEN power supply' which is also EPICS enabled and for BLM integration with EPICS will be discussed in the next section 3.5.2. So in this same OPI, PVs from both the devices (EPICS enabled current measuring device and power supply) have been used to control all aspects of BLM in operation.

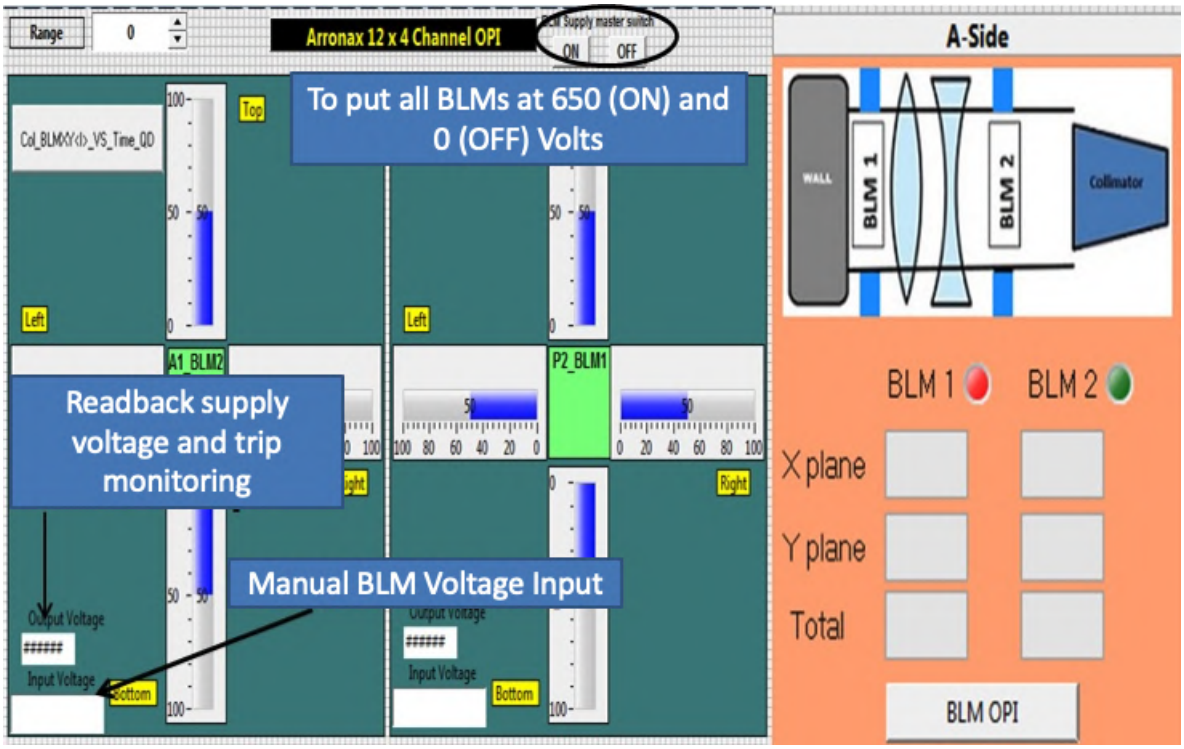

Figure 3.17: OPI developed for operators to monitor BLM signals during irradiation run.

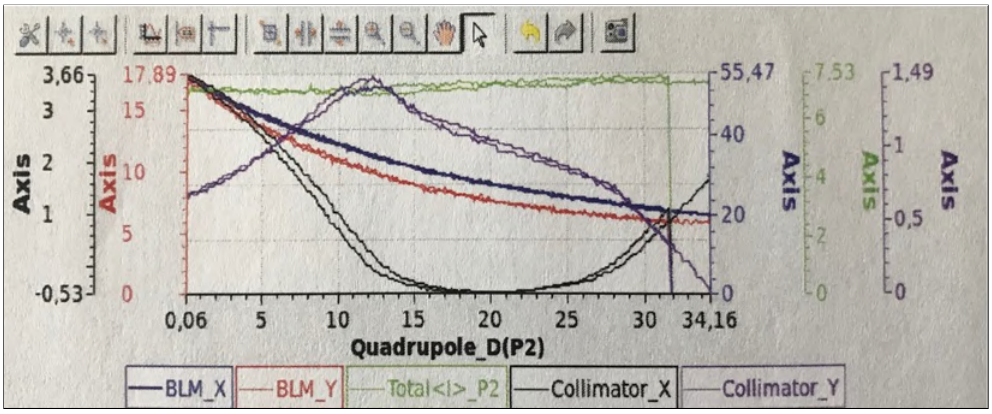

Figure 3.18: OPI developed for online data measurement of experimental data.

As discussed, the data is synchronized with time in the EPICS network. Therefore, an OPI has been developed for online data monitoring of experiments (see figure 3.18). Here, online data plots are synchronized with quadrupole settings during a quadrupole scan. The data

from BLM and collimator in the X and Y plane is plotted with total beam current or intensity (target + collimator). This OPI gives a good online approximation (without normalization) of experimental results. Similarly, an OPI has been developed for beam positioning.

3.5.2 BLM integration within EPICS network

As illustrated in figure 3.19, a 12-channel SY5527LC CAEN power supply provides the required voltage to the BLM differential plates located in the beamlines. The readout electronics is provided by iThemba Labs and is based on beaglebone (BB) boards. They are integrated within the EPICS as shown in figure 3.19). In the EPICS environment, the network is local (not connected with the internet). Therefore, a "Local Network Time Protocol" (LNTP) code has been installed in both BB devices. This LNTP keeps BB time synchronized with the main server computer. Operators can control both voltage supply to BLMs and BB device settings with CS-Studio's operator interface (OPI). For a detailed discussion on BLM, see chapter 4.

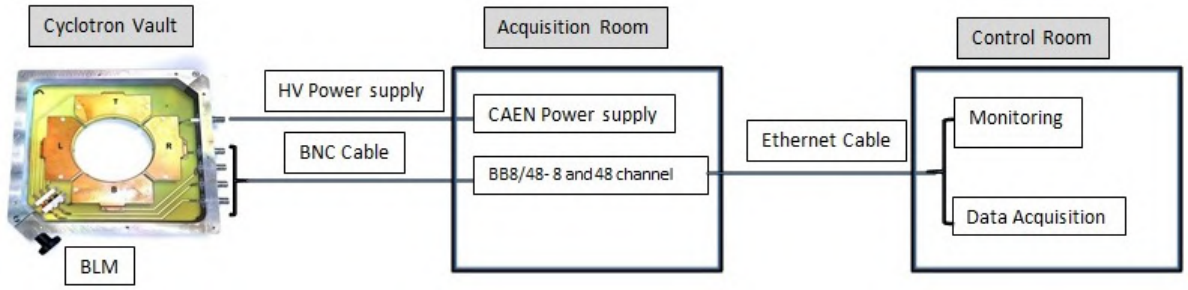

Figure 3.19: BLM connection flow chart.

Scale	BB8	BB48
1	1-20 mA – Integration time 2 μs	1-200 μA – Integration time 2 μs
2	1-2000 μA – Integration time 20 μs	1-20 μA – Integration time 20 μs
3	1-200 μA – Integration time 2 μs	1-2000 nA – Integration time 200 μs
4	1-20 μA – Integration time 20 μs	1-200 nA – Integration time 2 ms
5	1-2 μA – Integration time 200 μs	1-20 nA – Integration time 20 ms
6	1-200 nA – Integration time 2 ms	1-2000 pA – Integration time 200 ms
7	1-20 nA – Integration time 20 ms	
8	100-2000 pA – Integration time 200 ms	

Table 3.1: Details about various scales of BB8 and BB48 current measuring device.

The BeagleBones run Ubuntu linux distribution and are connected to dedicated electronics providing 8 or 48 channels (BB8 and BB48) as shown in figure 3.20. The current integrations are performed by an 8053 chip. The beagle bone sends a start signal and polls the chip. In this way, a specific time stamp is associated. BB8 and BB48 chips are tuned to achieve integrations as low as 100 pA and 1 pA, respectively. Their scales are detailed in the table 3.1 and can be set

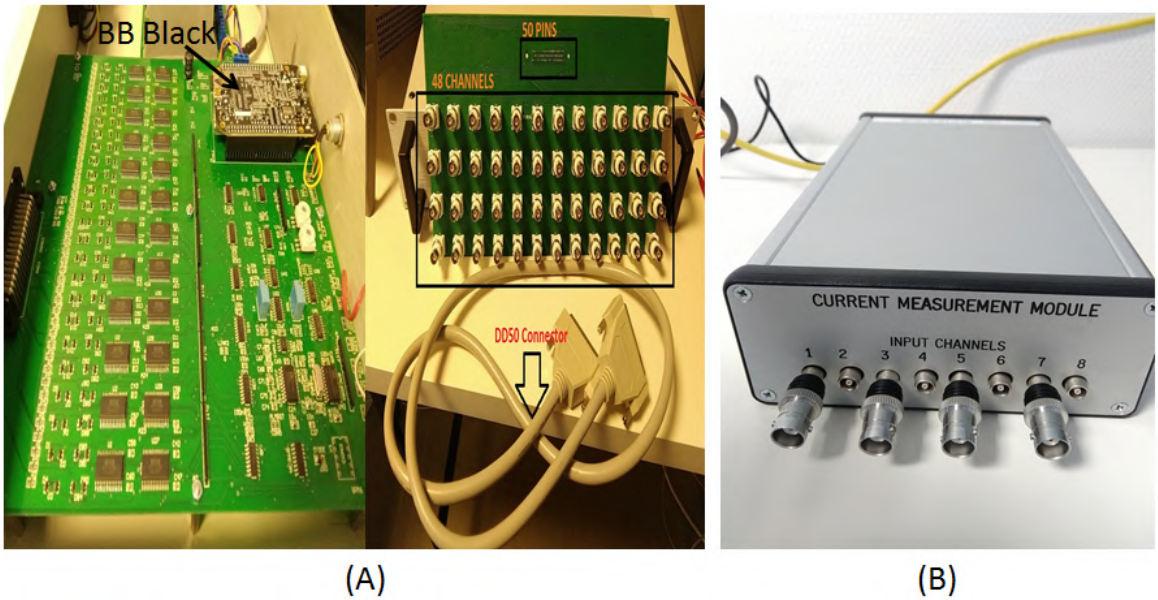

Figure 3.20: (A) BB48 board with Beaglebone black installed. (B) 8 channel current measuring device - BB8.

to a specific scale/range by using associated PV name. The main EPICS PV codes which suit ARRONAX environment with calibration coefficients and OPIs in CS-Studio for these devices were developed during thesis work.

The calibration tests have been performed with the available device 'Keithley current generator'. The output response of each scale of BB8 and BB48 is tested prior to their use for BLMs. The response of BB8 and BB48 was recorded during 48 hours, with a fixed input from the generator: No variations were observed. Therefore, beagle bone response is not only close to accuracy but stable in time. During BLM tests, the available device was BB8 which has been used to test the response of BLMs. The best suitable scale for the experiment was scale 6 (1-200 nA) and error in this range ($0\% - 0.18\%$) was found during calibration tests of BB8. After satisfactory test results, BLMs were installed in high-intensity beamlines and have been connected to the BB48 device. The BLM response tests are discussed in the next chapter.

Chapter 4

BEAM LOSS MONITOR STUDIES

4.1 General Description

We have already discussed the theoretical background and selection criteria of BLMs so far. Prior to their installation, it is essential to perform some tests in order to study and compare them. This is required to make sure that all installed BLMs are giving a similar level beam loss response. Experiments were performed to study BLM's sensitivity towards charged and neutral particles. The stability and repeatability of the BLM response has been also studied. All tests were performed in a low-intensity beamline. These tests include direct and indirect irradiation of BLM with proton beam at low beam intensity and 68 MeV energy. A direct irradiation means the proton beam hits straight the BLM and indirect means irradiation with material (beam pipe or some material) in front of the BLM. The beam intensity is ranging from 600 pA to 6 nA on beam dump (see figure 4.1), used as a reference for intensity measurement. Comparative studies for a total of four BLMs have been examined.

4.2 Experimental Setup

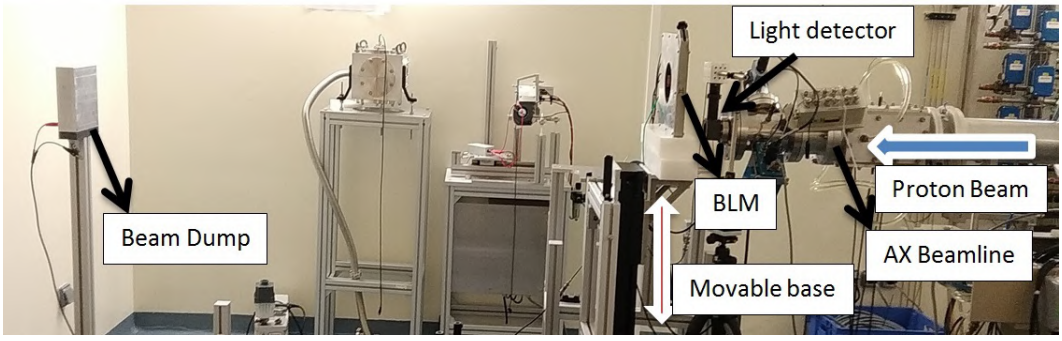

Figure 4.1: BLM test experimental setup.

For these tests, the BLMs were installed a few cm downstream the exit of the beam pipe on a movable table. This table has 2 degrees of freedom: this table can rotate or move along

the vertical axis. The experimental setup (see figure 4.1) includes a "Hamamatsu R928" photo-multiplier detector (light detector), used as a proton beam intensity monitoring reference (light emission by proton interactions with air [68]), and a large instrumented beam dump. The BLM and beam dump both are connected with a BB8 current measuring device which is EPICS enabled as discussed in chapter 3. Therefore, a total of 5 out of 8 BB8 channels are occupied.

4.3 BLM Tests

A total of four BLMs were tested under irradiation. Some experiments were performed twice or thrice to check the repeatability of results. Each BLM plate was connected through a 20 m cables with BB8 outside the vault. This cable is a combination of 3 RG59 cables for high volatage supply and 14 MXR cables with BNC connectors for BLM current measurement (see figure 4.2).

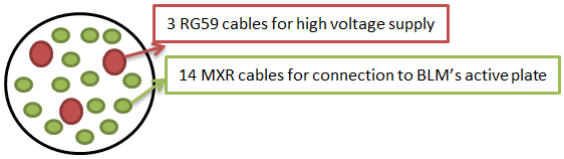

Figure 4.2: A description of the combination of cables used for BLM tests. In red and green color, 3 RG59 and 14 MXR cables are shown, respectively.

The Types of the experiment performed on BLM are listed below:

- Beam irradiating the BLM (direct) for geometrical and repeatability studies. Fixed intensity beam irradiation with varying BLM supply voltage to find suitable power supply prior to its use in the high-intensity beamlines.
- Materials were added in front of BLM to check their impact and simulate beam pipe (indirect).

The beam shots were recorded at two different positions using gafchromic film at 6 nA proton beam current, prior to tests. The first shot is at the location where BLM is positioned and another is at the location of the beam dump. It was done to estimate the beam size downstream and far behind the collimator of 10 mm diameter. The beam dump is being placed 134.5 cm behind the collimator and the BLM is placed 45.7 cm behind the collimator. The recorded transverse beam size is 15 mm at the BLM location and 40 mm at the beam dump location (see

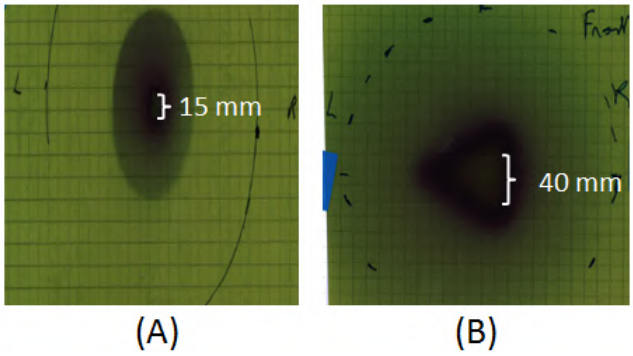

Figure 4.3: Beam shot at Gafchromic sheet placed at the location of BLM (A) and beam dump (B) during tests.

figure 4.3). The transverse beam size at the beam dump is still smaller than the beam dump dimensions. Thus, there is no transmission loss at the beam dump due to transverse beam size growth.

4.3.1 Direct and indirect beam irradiation with BLM vertical movement

During the irradiation of the BLM with 600 pA - 6 nA beam on the beam dump (performed 2-3 times at various beam intensities to check the repeatability) using 68 MeV proton beam, the supporting table was translated vertically at a very slow speed (approx. 0.32 mm/sec). The result shows as a scan of the geometrical response of the BLM active plates (see figure 4.4).

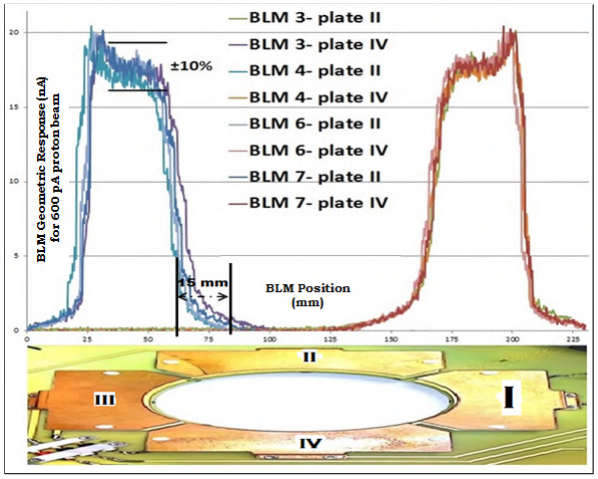

Figure 4.4: Comparison of four BLM signals obtained by moving them vertically. This movement allows to go through two active plate of each BLM. Here, these results are for 600 pA beam current measured at Faraday cup installed upstream of the collimator.

It was done with all four BLMs connected with BB8 scale 6 (see table 3.1). The level of noise in scale 6 is 0.2 nA. The active plates response between same BLM and all four BLMs

are being compared. During the scan, light detector placed upstream of the collimator gave continuous and stable output indicating stability of the beam. The beam dump response was also stable. But it detected current only when the beam was passing through the hollow section of the BLM. All active plates of the BLMs showed similar geometry and amplitude of signals, after renormalization to the intensity reference measurements done with the light detector and beam dump, when possible. The precision found in the limits of $\pm 10\%$, when BLMs were compared. The beam size is also found in good agreement with the gafchromic film image at BLM location (15 mm in the transverse plane). This is illustrated in the figure 4.4.

A 150 mm thick polystyrene high-density block, sufficient for stopping proton (verified by G4 simulations) was placed between beam exit window and BLM. BLM showed no signals during the experiment which means BLM is much less sensitive towards neutral particles (neutron, gamma). The level of noise is 3.5 pA which corresponds to BB8 scale 8 (see table 3.1). Therefore, what we measure on BLM is charged particles current. In G4beamline, polystyrene block with same thickness was simulated with 'virtualdetector' placed downstream of the block. The virtualdetector detected no charged particles but 0.037% neutron and 0.44% gamma out of simulated 1 million 68 MeV protons.

4.3.2 Indirect beam irradiation with rotating BLM on vertical axis

To replicate experimental conditions similar to operations, a 5 mm thick beam pipe is placed in the BLM's hollow circular part (see figure 4.5).

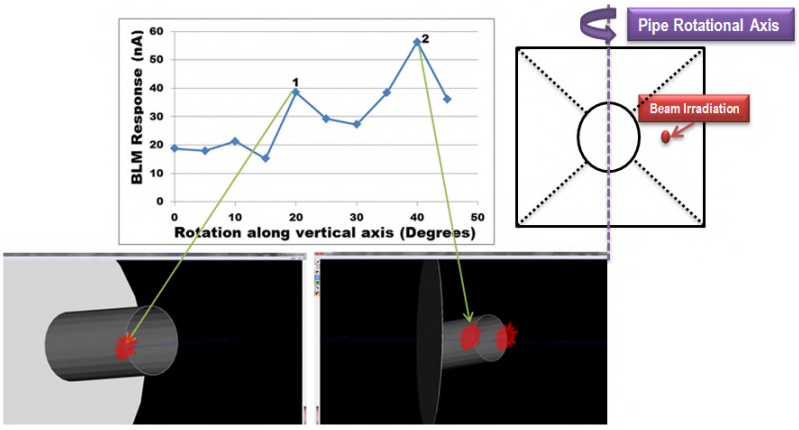

Figure 4.5: BLM response with rotated pipe along vertical axis. Bottom left and bottom right shows the beam irradiating one side and both sides of pipe, respectively. The data points are shown in blue diamond dots.

While irradiating, the BLM with the pipe is rotated along vertical axis in steps of 5 degrees. Initially, the beam is directly irradiating one of the BLM's active plates. Due to rotation, the material (Aluminum) of pipe arrives in between the beam and BLM's active plate (indirect irradiation on the BLM's active plate). In figure 4.5, the bottom left image with a red spot is showing, beam directly irradiating 5 mm Aluminum pipe at 20^o angle of rotation and the bottom right image with two red spots is showing, beam directly irradiating whole Aluminum pipe (10 mm thick) at 40^o angle of rotation. The signals are multiplied up to 3 times with respect to direct irradiation on the BLM's active plate. It is due to reduction of particle's energy (68 MeV initial energy) due to interaction with matter which is resulting in higher ionization cross section. This can be calculated using equation 2.24.

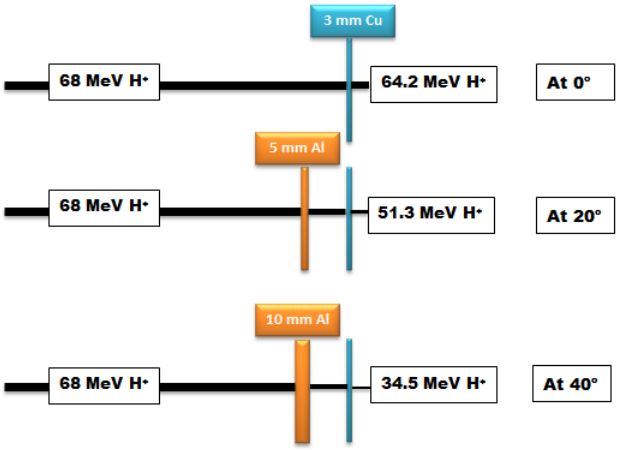

Figure 4.6: Reduction in proton energy due to interaction with matter. This simulation is being performed in SRIM V2013. On the right, experimental angle of rotation is shown for each case.

SRIM (The Stopping and Range of Ions in Matter) version 2013 [96] is used to study primary particle energy loss and relative ionization cross-section in air, when pipe is inter-spaced. In this calculation, the increase in the 5 mm thick pipe due to rotation and proton energy losses in the air have been neglected. At 0 degree angle of rotation, the reduction of energy is due to 3 mm thick copper material of the BLM plate. At 20 degree and 40 degree angle of rotation, a 5 mm and 10 mm thick Aluminum is added in this simulation. The kinetic energy of the beam at the BLM for 0^o, 20^o, and 40^o angle of rotation, is shown in figure 4.6.

For 5 mm thick pipe (20^o angle of rotation), the reduced energy of particles is 51.3 MeV with 0.58% energy dispersion. For 10 mm thick pipe (40^o angle of rotation), the reduced energy of particles is 34.5 MeV with 1.13% energy dispersion. The stopping power of proton in air, is being compared at these proton beam energies (see the plot in appendix A). Due to

reduction in the energy of the beam, the air ionization cross-section is 1.75 times higher at 20^o compared to 0^o angle of rotation. Therefore, the signals are increasing from 20 nA to approx. 35 nA (see figure 4.5). In the other case, the air ionization cross-section is 1.5 times higher at 40^o compared to 20^o angle of rotation. Therefore, the signals are increasing from 35 nA to approx. 53 nA (see figure 4.5). Thus, the major increase in the signals (experimentally) is due to the beam interaction with pipe material resulting in the reduction of the beam particle's energy. The ionization cross-section of the particle beam is higher at lower energies. This means more current will be integrated on BLM's active plate. A stable response of light detector was observed during the scan indicating stable operation conditions. Thus, it is certain that the beam was not hitting at a different location on the collimator. Therefore, the majority of the current measured at the BLM is from the primary particle energy loss and ionizing current generated depending on particle's ionizing cross-section in air. However, there should be some contribution in the measurements from shower particle production.

4.3.3 Fixed intensity beam irradiation with varying BLM supply voltage

Each BLM was irradiated with fixed beam intensity on target and with varying supply voltage. It was repeatedly experimented with different beam intensities (600 pA to 6 nA). Furthermore, it was performed on different active plates of different BLMs. This experiment is performed to investigate the right voltage supply to be set on BLMs. However, the supply voltage depends on the intensity of ionizing radiation creating ionizing current in a gas ionization detector. This has been already discussed in the explanation of figure 2.30. Similarly, one can see this dependence in the experimental results shown in figure 4.7.

There are three plots shown in different colors. The data points of each plot are being recorded at fixed beam current with varying BLM's supply voltage. The region where ionizing current is varying with increasing supply voltage, this region is termed as recombination region. After this region, ionization region comes where ionizing current is constant with increasing supply voltage. In the figure 4.7, red, green, and blue curves are attaining ionization region at 90 V, 220 V and 650 V, respectively. The level of beam losses for red curve is too low (2 nA). It has been assumed that the level of beam losses at ARRONAX should vary from 10 nA to 100 nA (1 to 2 in log scale) during a standard irradiation runs. Thus, 650 V is the chosen supply voltage for the BLM. At this voltage, signals will not fall in the recombination region (voltage

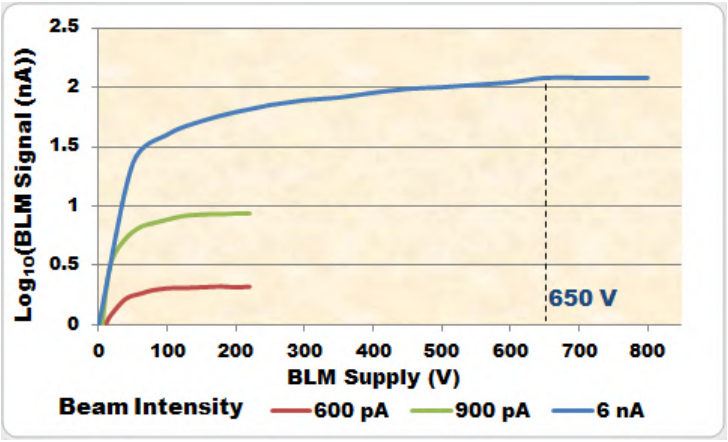

Figure 4.7: BLM response w.r.t. to supply voltage at three fixed beam intensity. The curves in red, green, and blue represent fixed beam intensity of 600 pA, 900 pA, and 6 nA, respectively.

dependence). However, the loss detection can sometimes fall in the proportional region (at 650 V supply voltage) if ionizing current detected is too low (< 1 nA). This test ensures the same BLM responses with varying levels of beam losses in high-intensity beamlines.

4.4 BLM Installation on High-Intensity Beamlines

After performing BLM tests, BLMs have been installed in three high-intensity beamlines. As shown in the figure 4.8, a first BLM is located upstream a quadrupole doublet and a second one 1.65 m downstream. Both locations have gaskets which are sensitive points if losses occur. Therefore, this study is being performed to set a threshold to avoid rubber gasket damage.

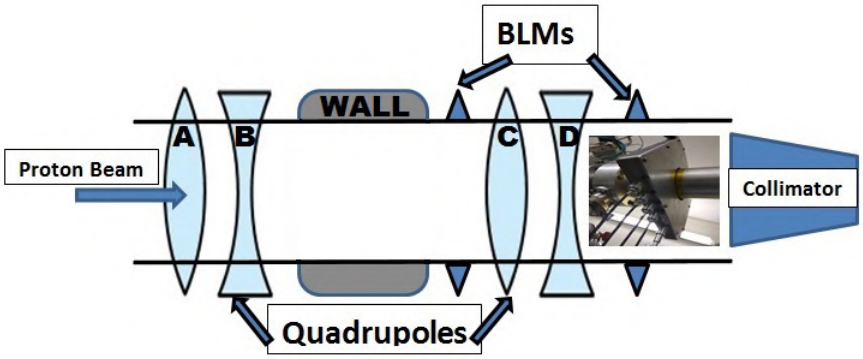

Figure 4.8: Beamline layout with 2 BLM installed.

Several independent irradiation runs (Total counts are 13 see figure 4.9) spanning over more than 100 h and of the order of 130 µA on target have been performed. The configuration of each

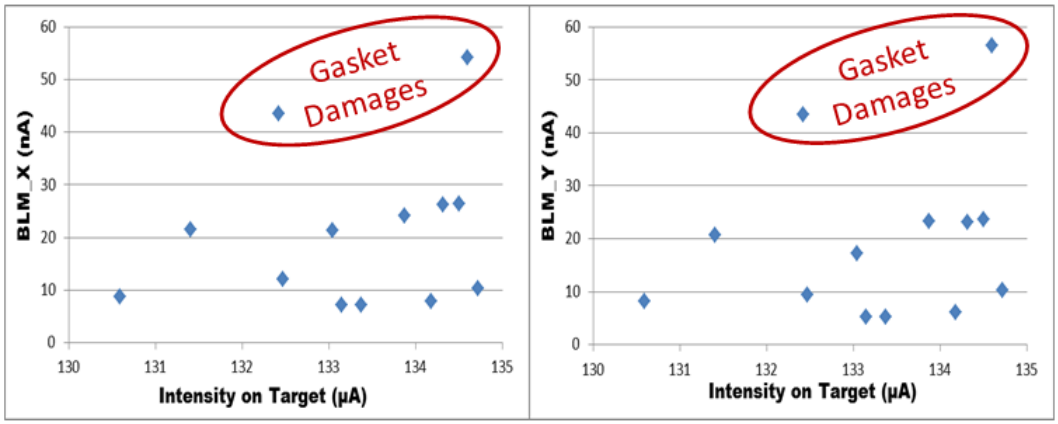

Figure 4.9: On the right, target average intensity (μA) vs average BLM signal (nA) in X plane is shown and on the left, target average intensity (μA) vs average BLM signal (nA) in Y plane is shown. Here, data is collected and analyzed from total 13 irradiation runs (number of blue diamond points).

magnetic element of the accelerator and beamlines (including dipoles, steerers, quadrupoles) during runs were set according to in-house standard operational relevance (eg. Beam transmission rate). This allowed to accumulate data from the BLM as given in figure 4.9. In this figure, a correlation between average beam losses in a plane and average beam current on the target is shown for total 13 irradiation runs. The average level of beam loss is under 30 nA in 11 out of 13 runs. With some configurations, losses (average) have reached up to 60 nA. For runs with BLM measurements above 40 nA, post-operation tests on vacuum and gasket showed leakages and damages. This advocated the need to set a minimum threshold for the losses measured on the BLM. This limit was proposed to be 50 nA for 650 V supply voltage. To account for lower intensity runs and then losses, a 30nA value has been also defined for 220 V BLM supply voltage.

4.4.1 BLMs for background radiation measurement

BLM was also placed in one of the high-intensity beamline near Faraday cup in the cyclotron vault (see figure 4.10). During irradiation runs, BLM detected no background radiation. It has already been verified that the BLM does not detect radiation coming from the back side. BLM responded when Faraday cup is inserted in the line (see table 4.1).

It shows that the level of background radiation is lower than BLM's sensitivity when Faraday cup is out of line. The background radiation increased, when the beam is being stopped by

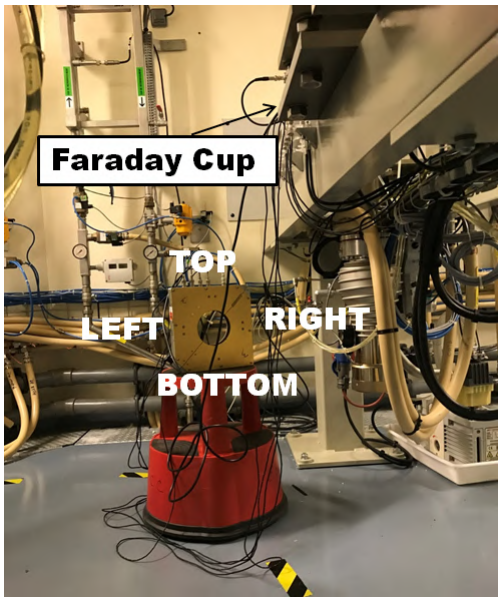

Figure 4.10: BLM placed near Faraday cup for background measurement test.

Faraday cup. This is done to use BLM for background radiation detection but background level is lower than BLM's sensitivity. Therefore, BLMs can only be used for background detection in high activity zone such as target station (12000 mSv/h), Faraday cup locations (when inserted), cyclotron vault (1500 mSv/h), etc.

Beam on Faraday (μA)	**RIGHT** (nA)	**TOP** (nA)	**LEFT** (nA)	**BOTTOM** (nA)
10	1.82	1.86	1.12	1.32
30	5.11	4.86	2.68	3.56

Table 4.1: BLM active plates background radiation detection when Faraday cup is inserted.

4.4.2 BLM operationality tests

The Operationality test performed below is to indicate if the BLM shows the expected behavior when quadrupole tuning is applied. This is done for both BLMs placed on a high-intensity line (see figure 4.8). For BLM 1 (upstream of the 2nd pair of quadrupole), the behavior of losses is studied by the 1st pair of quadrupole (i.e. quad A and B) current variation mapping. For BLM 2 (upstream of the collimator), operationality test is performed by a quadrupole scan of the last quadrupole (i.e. quadrupole D).

BLM 1 test: In a pair of quadrupole, 1st quadrupole is X- focalizing and 2nd quadrupole is Y-focalizing according to standard polarity settings at ARRONAX. For this test, 3D mapping of 1st pair of quadrupole is performed in standard and reverse quadrupole setting polarity. This

3D mapping is created by performing quadrupole A scan (54 A to 71 A) at several settings of quadrupole B (quad A and B scan mapping).

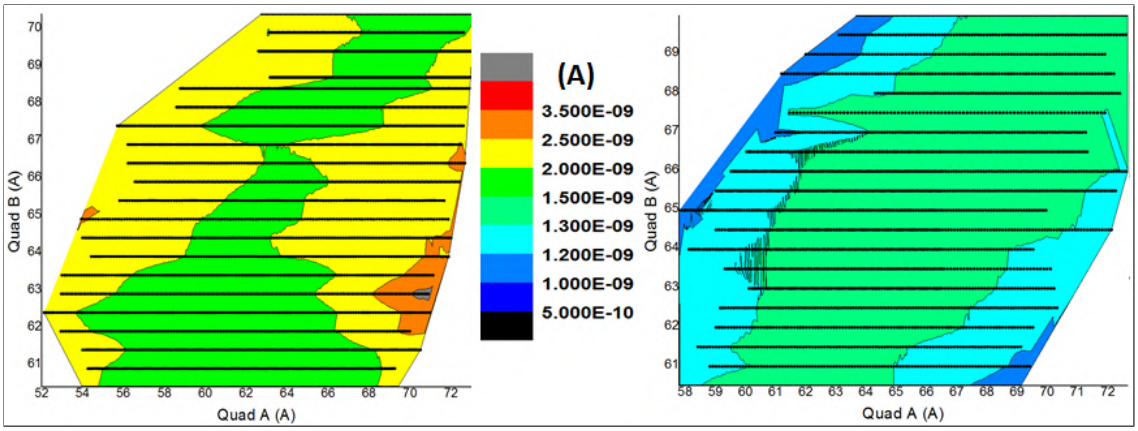

Figure 4.11: 3D mapping of beam losses as a function of Quad A and Quad B settings in X plane with standard (on the left) and reverse (on the right) quadrupole polarity. Black dots are the actual data points.

The measurements of the BLM 1 is indicated in figure 4.11 which is showing that losses increase when the first quadrupole move the focal X-point close or away of the BLM. This increase of loss is supported by the increase in vacuum and decrease of intensity at the end-of-line. The inverse general behavior, with respect to the quadrupole settings, is also checked in reverse polarity configuration of the quadrupoles where the maximum losses in reverse polarity correspond to the minimum losses with the standard polarity settings. With this reverse polarity, the first quadrupole is Y-focalizing and the second is X-focalizing. Here, a 30 µA proton beam on target is used in both configurations.

When results of 'quad A and B scan mapping' are compared in X and Y plane with both configurations. It has been found that in reverse polarity highest beam loss (1.362E-09 A in X) is smaller than the lowest beam loss (1.82E-09 A in X) in standard polarity. A reduction in the overall losses has been observed in reverse polarity (see figure 4.11). However, simulations (replicating the same experiment) indicated no such change in the beam losses at the location of that BLM. It is highly possible that the location of losses might have shifted (experimentally) and BLM detected lower signals in reverse polarity. Moreover, operational settings of the second pair of quadrupole have to be kept at least 20 A higher in order to converge the beam on the collimator and target in reverse polarity quadrupole configuration. Due to this limitation, it has been concluded that the standard configuration is better and operational for irradiation runs. This test is also verifying that BLM 1 is operational.

BLM 2 test: For this test, Quadrupole D scan is performed which is placed upstream of the BLM 2 (see figure 4.8). The response of the BLM 2 during a quadrupole scan is shown in figure 4.12. This scan is performed in such a way that one can see the effect (loops) of hysteresis in both planes of BLM response. The quadrupole scan is initialized at 10 A then the current is gradually increased till 70 A. It is then decreased till -70 A and is brought back to initial setting (i.e. 10 A) in the same way.

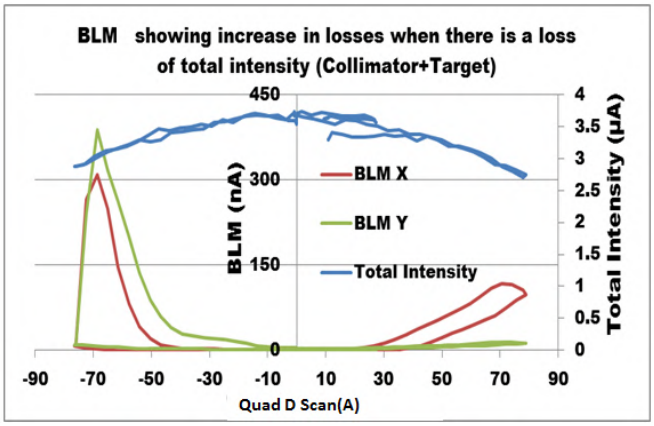

Figure 4.12: BLM 2 response to an upstream quadrupole scan and scan is performed in such a way one can see the effect of hysteresis. BLM X and Y is the local beam size in horizontal and vertical plane, respectively.

The BLM 2 response is also compared with total intensity (sum of collimator and target current). A correlation has been observed between total intensity and BLM 2 response. Any loss in total intensity indicates an increase in beam loss. This increase in beam loss can be seen on the BLM responses in both the transverse plane. At ARRONAX, the quadrupole is y focalizing in positive current configuration and vice versa. From 30 A to 70 A, BLM X is showing losses due to defocalizing effect of quadrupole D in X plane. On the contrary, both planes are showing losses from -30 A to -70 A. The losses in Y plane is due to defocalizing effect. In X plane, these losses are due to over focalization effect of Quadrupole C and D (both are X focalizing mode). The focal point is located in front of the BLM 2 in X plane with large envelop size causing beam losses.

The BLM 1 and 2 both are indicating losses relative to their upstream quadrupole settings. Hence, we can conclude that both BLMs are operational and indicating the losses at their installed locations. Nevertheless, one should keep in mind that BLMs are only detecting local losses (not the beam loss distribution over a beamline) and the measurements are not absolute (an amplification is always there).

4.5 Conclusion

The electrical response from BLMs did not show any unexpected behavior. The BLM does measure the increase of charges behind a pipe (BLM operationality tests). These BLM were then installed in high-intensity beamlines and regularly monitored.

BLM Characteristics	Experimental results
Charged particle detection	Yes
Charged particle detection sensitivity	High
Neutral particle detection sensitivity	Low
Output signal	Current Integration
Operating voltage	650 Volts

Table 4.2: BLM Characteristics.

After the first two quadrupoles, BLM helps to indicate losses at that location while the downstream BLM shows beam loss indication of the second pair of the quadrupole. The threshold on BLM will facilitate operators to tune the beamline and also, will act as an indication of beam optics issues during irradiation. The BLMs with increased diameter for 5 mm thick pipe are under production and will be installed when ready. Thus, transverse beam dynamics studies based on quadrupole scans have been performed. These studies include BLM signals and the collimator 4-finger upstream of the target which measure integrated current deposited by particles. The overall findings are tabulated in the table 4.2.

4.6 Future Extention of BLM Installation

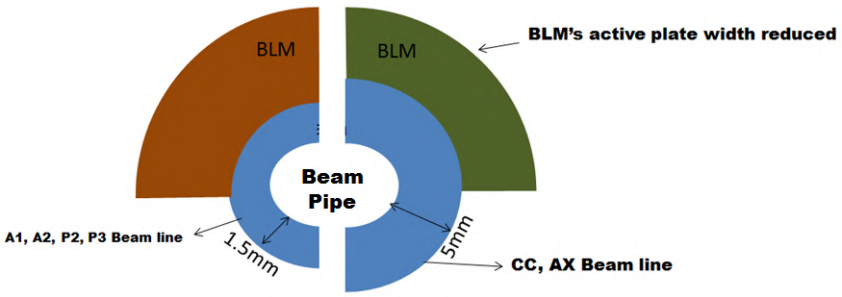

Figure 4.13: Beam pipe with different thickness at ARRONAX. On the left, pipe thickness is 1.5 mm in high-intensity beamlines. On the right, pipe thickness is 5 mm in cyclotron vault and low-intensity beamline.

All available BLMs are optimized for high-intensity beam pipe (A1, A2, P1, P2, and P3 beamline) by geometry. But the beam pipe geometry of low-intensity beamline (AX beamline)

and cyclotron vault (CC) are different. The thickness of the beam pipe in high-intensity line and CC or low-intensity line is 1.5 mm and 5 mm, respectively (see figure 4.13). But the internal diameter is the same. Therefore, G4beamline simulations have been used to study required BLM geometry and variation in the beam losses compared to 1.5 mm thick pipe.

As shown in figure 4.14, this is the comparative studies of BLM compared to 1.5 mm and 5 mm thick beam pipe in simulations. Here, 70 MeV proton beam (10000 events) with secondary particles generation enabled configuration is used to study that in G4beamline simulations. Initially, the beam transverse dimensions are chosen such that both BLMs detect losses with centered beam. Subsequently, an off-centered beam in the X plane has been introduced to study higher losses and BLM response with 1.5 mm and 5 mm thickness of the beam pipe. This has been studied in $\pm$ 10 mm horizontally off-centered beam with the step size of 2.5 mm.

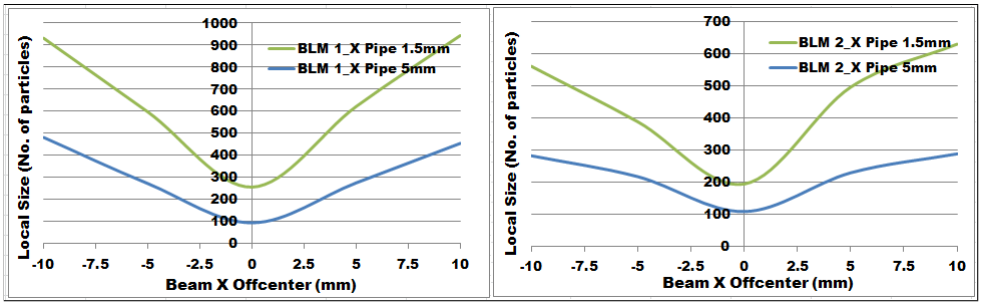

Figure 4.14: Simulation of beam loss detection with 1.5 mm and 5 mm beam pipe. Here, negative sign on the x-axis shows left off-centered beam in horizontal plane and vice versa.

It has been found that the BLM signal has reduced by a factor of 2 for 5 mm thick pipe compared to 1.5 mm thick pipe despite the identical losses in both simulated cases. For 5 mm thick pipe, the 'virtualdetector' with larger dimensions were also simulated. This was done to check if it is possible to increase the loss detection coverage range of the BLM's active plate in order to maintain same level of response compared to 1.5 mm thick pipe. But most of the particles stopped in the thickness of the pipe and there is no difference observed in the level of loss detection. Thus, the simulations indicated that changing the active plate dimension of the BLM will not help to maintain the same level of response. Therefore, it is advised to keep the outer dimension of the BLM similar to the BLMs in the high-intensity line. But the inner hollow circular dimension should be bigger such that it fits adequately on the beam pipe with thickness of 5 mm . At the time of writing, these new BLM is under production and will be installed in the low-intensity beamline and cyclotron vault.

Chapter 5

TRANSVERSE BEAM DYNAMICS STUDIES AT ARRONAX

5.1 Initial Studies

As presented below, various studies on beam dynamics have been performed, by IBA during the development phase and by ARRONAX in the hands-on phase of the C70 ARRONAX machine: IBA performed simulations to study beam dynamics in injection line, cyclotron dees, and beam extraction. Also, IBA implemented single and multi-particle tracking simulations such as TOSCA [83] and TRANSPORT. Later, experimental and simulation work were performed by ARRONAX on beam dynamics for several beamlines. The beam dynamics studies include the single particle tracking tool called G4Beamline simulations, used at ARRONAX. These base studies from IBA and ARRONAX are pertly described below.

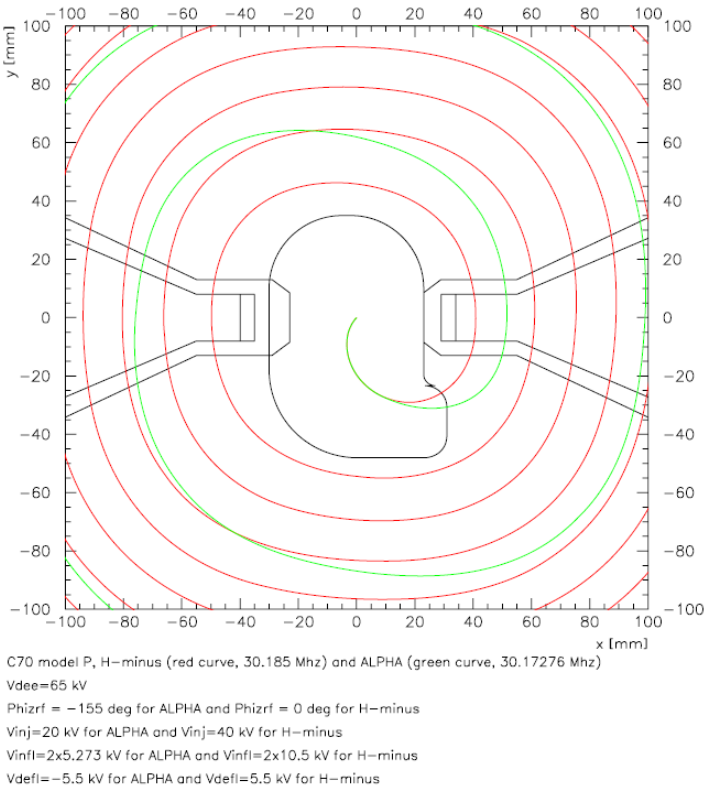

Figure 5.1: Turn patterns for particles accelerated on 2nd harmonic (red curve) and for particles accelerated on fourth harmonic (green curve) [11].

Using the TRANSPORT model, IBA studied the H^- beam envelopes from the source to the inflector in the work of W. Kleeven et al. [11]. It has been found that beyond the triplet the round beam is restored. A minimum beam envelope is right behind the second solenoid i.e. injection Glaser (see figure 2.7) where the buncher is placed. Within the cyclotron Glaser solenoid, the beam envelopes obtain a maximum size and are then focused strongly to a few mm size corresponding with the calculated matching condition of Eigen-ellipse of the cyclotron. It was also studied emittance growth factors in the cyclotron by comparing the emittance at the injection and after 50 turns. The estimated emittance growth factors are 2.7 horizontally and 1.4 vertically for the H^- beam. The H^- makes about 540 turns up to 70 MeV and other ions make about 155 turns up to their respective maximum energies (see figure 5.1).

In order to study the extraction system, The H^- isochronous field map was modeled from the 3D magneto-static model calculation in TOSCA by IBA [26]. A single particle tracking studies was used to determine the radial positions of stripper foil as a function of beam energy, in such a way that all paths cross in the center of the switching magnet. In this study, it has been found that the stripping process redefines the horizontal phase space parameters and vertical phase space remains unchanged. It was done with multi-particle tracking studies for energies 35, 60 and 70 MeV (see table 5.1). The circulating beam's normalized emittance was taken as $\epsilon_H^N = 6\pi$ mm-mrad. It has been found that the redefined emittances (after stripping) in the horizontal plane are much smaller than the circulating ones.

T (MeV)	70	60	35
$\epsilon_H(\pi mm - mrad)$	3.0	3.3	6.0

Table 5.1: Normalized horizontal emittance at different H^- beam energy.

An overall analysis of beam losses by G4Beamline simulations has been done in the work of Xiao LI [70]. The primary goal was to estimate the most suitable position for the installation of beam loss monitors. Beam's definition at the beginning of the beamline used in the simulation is provided by IBA's simulation results. The potential of large beam envelop size was found at the location of the second pair of quadrupoles. Thus, the major losses are distributed in the pipe downstream of the wall (see figure 4.8). Also, preliminary simulations have shown that the space charge effect does not play a dominant role in the range of use <200 µA and 70 MeV proton beam. These simulations were performed in the work of W.Tan [84]. Similarly, a beam alignment in a beamline was studied in the work of Shuang NING [71]. It has been found experimentally that the stripper foil azimuthal settings help to align the beam at the last pair

of quadrupoles. Nevertheless, simulation of the beam alignment was not able to provide more theoretical evidence to support the experimental results.

In the work of A.Sengar [85], quadrupole scans have been performed at beam intensity ranging 10-30 μA. The main goal of these quadrupole scans was to find the best settings for the transmission in the beamline with adequate beam size at the target location and to measure the beam emittance. In order to perform preliminary emittance measurements, a model-dependent study was implemented. At first, a transformation of the proton deposition on the collimator (10 mm aperture radius) into the beam dimension was done. It was then plotted as a function of the strength of the quadrupole setting. The parabola obtained was then fitted to acquire the emittance according to:

$$\epsilon_x = \frac{\sqrt{AC}}{d^2} \tag{5.1}$$

Where A and C are parameters of the fitted parabola similar to a single wire scan and d is a distance, here a fixed conversion factor from the simulation model is used. The first measurements indicated variation in the emittance by a factor of 4 for runs separated by few weeks. In part, these results have been given in this paper [69].

As discussed in the above mentioned studies, transverse beam dynamics plays an important role in the transport of the ions to the end-of-beamline. They also revealed the need for further and more detailed studies, specifically in regards of:

1. Stripper foil azimuthal settings help to align the beam on the last pair of quadrupoles. The operational observation requires examination of the implied physics.
2. Beam loss simulation indicated how losses are distributed in a beamline. How to reduce them, needs more experiments and theoretical studies with BLMs installed at those locations.
3. Emittance measurements differed by a factor of four when measured at different times. The root cause of this, requires more studies and statistical studies to test the machine over a period of time.

In this chapter, we will discuss performed G4Beamline simulations and experimental studies on transverse beam dynamics with protons in the beamlines of ARRONAX C70 cyclotron. Most of the experimental studies have been performed with a high-intensity beam (μA). Some specific studies include also a low-intensity beam (nA).

5.2 G4Beamline Simulations

In simulations, the high-intensity beamline is modelled as discussed in section 3.4. At first, measurements are performed on high-intensity beamline in order to get the relative placement of beamline elements and their dimensions. An attempt has been made to model the actual quadrupole fields in simulations including fringe field (see figure 3.11). The transverse beam trajectories have been studied with the optimized simulation model.

5.2.1 Simulations of beam envelop

Beam envelop depends on focusing and bending magnetic elements setting. The high-intensity beamline at ARRONAX has two pairs of quadrupoles. Thus, the beam envelop is being studied with multiple combinations of the quadrupole settings in G4beamline simulations. The beamline geometry implemented is without the beam pipe (see figure 5.2). This is done to avoid any beam interaction with pipe for better envelop simulations. As there is no vacuum pipe, the world material defined here is the vacuum. A 70.3 MeV proton beam with 30000 events is used here, as discussed in chapter 3.4. A "profile" command (for more details see chapter 3.4) is used to study the beam envelop (beam sigma in X and Y). The main objective of this study is to find the best possible combination of quadrupole settings for which the best beam transmission can be achieved. Also, the focal point of the beam at the end of line is one of the key parameter which ensures safer target irradiation. The desired focal point can be found in front or far behind the target with an optimal beam size on the target location. The secondary objective is to verify location of large transverse beam envelop in a beamline.

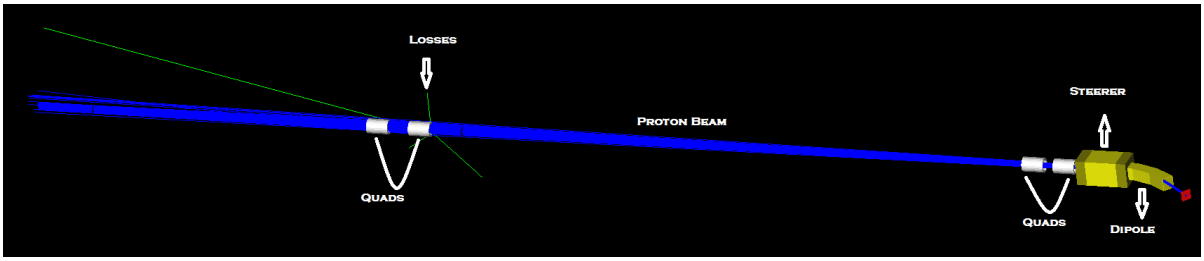

Figure 5.2: Visualization of a beamline implemented for beam envelop studies (simulations).

In the simulations, the exact experimental beam configurations, such as particle spread, and beam divergence, are unknown. Therefore, a few quadrupole scans have been performed and compared with the experimental results prior to the beam envelop studies. These quadrupole

scans (experiments) were following the production run settings. The same quadrupole settings (Quad A, B, and C) are used in the simulations and a quad D scan is being performed and compared. The quadrupole scan results, in terms of percentage of electrical deposition for the experimental and percentage of particles, are shown in figure 5.3. The scans use the same settings in both, the simulation and the experiment and display a good agreement. This is an indication that the beam trajectories in the simulations are relatively similar to the experiments when the same quadrupole settings are used. The differences are due to different experimental and simulated beam definition. A hypothesis has also been made in these studies that the beam divergence in X is higher than Y at ARRONAX beamlines with 0.26 MeV/c momentum dispersion of the gaussian beam. So in simulation, beam configurations used are as such. This hypothesis is based on IBA's obtained results during the design phase [11].

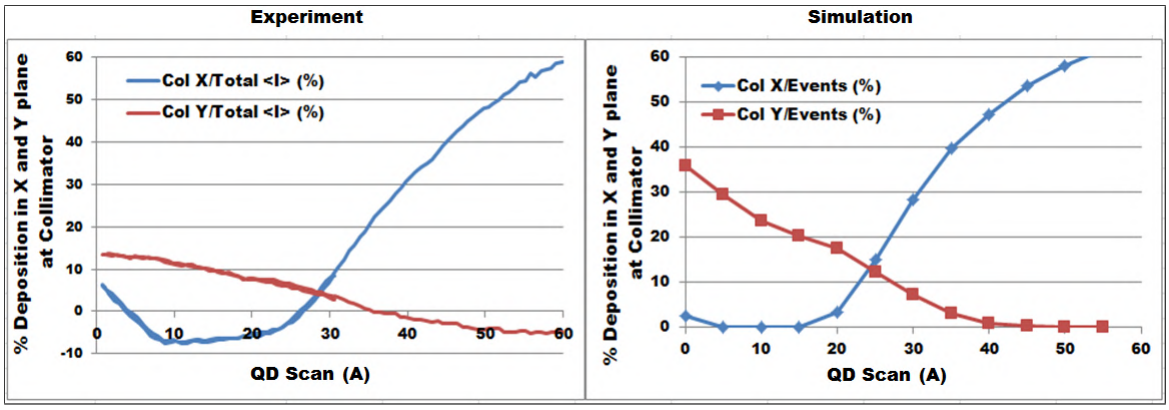

Figure 5.3: Comparison of simulated and experimental quadrupole scan (P side) results using the same quad A (-56.39 A), B (-63.65 A), and C (-40.94 A) settings. Right side shows the result from the simulation and Left side shows experimental result.

To identify potential focal points with respect to the settings of the quadrupole, various combinations are explored using the simulation. The resulting transverse beam envelop, with several combinations of quadrupole settings, are shown in figure 5.4. Each quadrupole configuration is coded in the legend. The two-digit number represents all quads at the same setting, 2 two-digit number means 1st two-digit is QA/QB setting and 2nd two-digit number shows QC/QD setting, and 8 digit number is showing two digits for each quadrupole settings in this sequence QA, QB, QC, and QD. According to the standard quadrupole configuration, QA and QC are X-focalizing while QB and QD are Y-focalizing. The range of quadrupole setting combination used in the simulation is 35 A to 65 A as applied during irradiation runs.

A large beam envelop is always found upstream of the last pair of quadrupole. It is also found that the focal point in front of the collimator is not possible in both the transverse plane

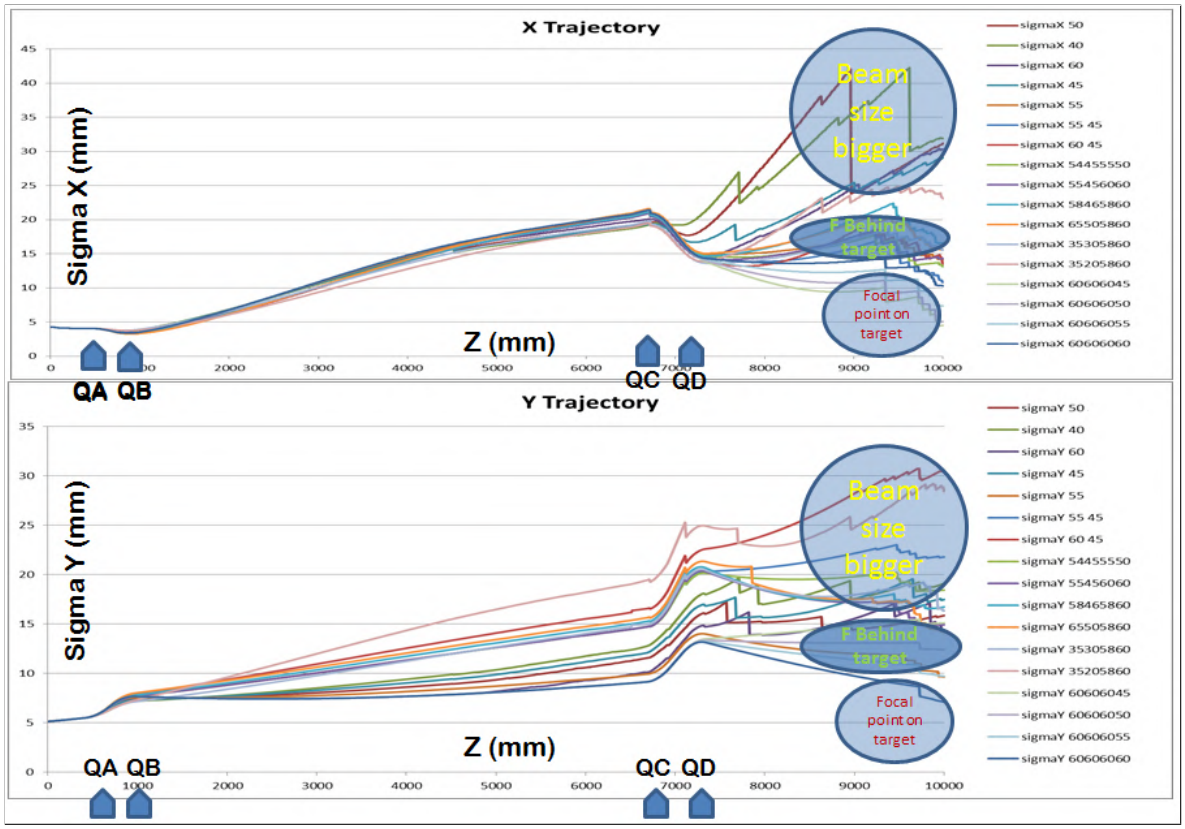

Figure 5.4: Beam envelop at several combinations of quadrupoles (QA, QB, QC, and QD). Top shows X and bottom shows Y beam trajectories.

together for any quadrupole setting combination. When the focal point is in front of the collimator in any of the plane then the focal point in the other plane is always far behind the collimator. Yet, a few quadrupole configurations are found for which the focal point is behind the target in both transverse planes. These configurations are discussed below:

- **QA (X Ampere), QB (X-10 Ampere), QC (Y Ampere), QD (Y-5 Ampere)**: As one can see in figure 5.2, the drift space between the 1st and 2nd pairs of quadrupoles is long (5 m approx.). In this quadrupole settings, the beam in the X plane gets lesser defocalizing effect by quad B, and the losses are significantly reduced. The configuration of Quad C and D is as such that the focal point is far behind the target. This configuration is reverified at several such quadrupole setting combination and at several beam emittances to check robustness. At smaller transverse emittances, there are fewer particle deposited on the collimator. This allows to push the focal point position further behind the target. This type of quadrupole settings are ideal for the desired beam envelop. The operators put 8% proton deposition on collimator (equal on each finger) during irradiation. This operational constraint is checked for this configuration in simulations. It is found that QA (X Ampere), QB (X-10), QC (Y Ampere), QD (Y-15 Ampere) is the possible setting to have equal deposition on collimator. In this configuration, the focal point in X is on the target which can damage the target. So this type of settings can not be used at ARRONAX high-intensity beamlines.

- **QA (X Ampere), QB (X±2 Ampere), QC (Y Ampere), QD (Y±2 Ampere)**: In this quadrupole setting, the focal point is behind the target with higher losses compared to the above-discussed settings. Even so, in this configuration it is possible to obtain equal deposition on the collimator's fingers. When production settings data is analyzed for quadrupole settings over the span of 1.5 year (21 irradiation runs), it is observed that quadrupole settings in 15 out of 21 irradiation runs are in this configuration QA (X Ampere), QB (X±5 Ampere), QC (Y Ampere), QD (Y±5 Ampere). However, the setting of QA is being found mostly at a smaller current than QB.

The configuration that operators usually keep, is with QA at a lesser input current than with QB. In such configuration, the longitudinal distance between the focal points in X and Y is reduced. This type of quadrupole settings are adequate when there is a need for homogeneity in the transverse plane for a specific experiment. The above studies are indicating that there are not so many quadrupole setting configurations possible for operators due to the operational requirement, i.e. the equality of electrical deposition on the fingers of the collimator. Also, the focal point in front of the collimator is not possible in both transverse plane, though it can be pushed further behind the target at smaller transverse emittances.

Thus, the results from quadrupole scan with the end-of-line collimator are studied at several transverse beam emittances. This is done to study the impact of transverse emittance in a beamline at the collimator by an upstream quadrupole scan.

5.2.2 Simulations of transverse beam emittance in a beamline

The beam emittance can be measured by several methods as discussed in chapter 2. In the low-intensity beamline, a single wire beam profiler is installed and used. In this measurement technique, quadrupole scan is performed to sample the beam profile, with no disturbance in the drift space between that quadrupole and beam profiler. These studies of emittance measurement will be discussed in section 5.3.3. There is no profiler pre-installed in a high-intensity beamline. So the emittance measurement is not possible in high-intensity beamline at ARRONAX. Also, because there are fewer particles intercepted by the collimator, the focal point can be pushed further behind the collimator at smaller emittances as discussed in previous section 5.2.1. Thus, the impact of transverse beam emittance in a beamline at the end-line collimator is studied in simulation by an upstream quadrupole scan.

In G4beamline, a beam can be defined by transverse beam width (σ) and beam divergence

(angle) in each transverse plane. Any change in σ or angle changes the transverse beam emittance in a beamline. Therefore, quadrupole scans are simulated separately at various beam divergences and particle spreads in a plane. A 70 MeV proton beam with 10000 events are used. A virtual detector is also placed downstream of the collimator, to keep a track on the total number of particle during a quadrupole scan, that are passing through collimator's aperture. The total number of particle in simulations is equivalent to the total beam current and already discussed in section 3.3. In simulations, the total number of particle is the sum of number of particles at virtual detector and total number of particles lost at the collimator. The collimator is defined in such a way that it kills all interacting tracks. Therefore, collimator and virtual detector behind it, can not detect the same event.

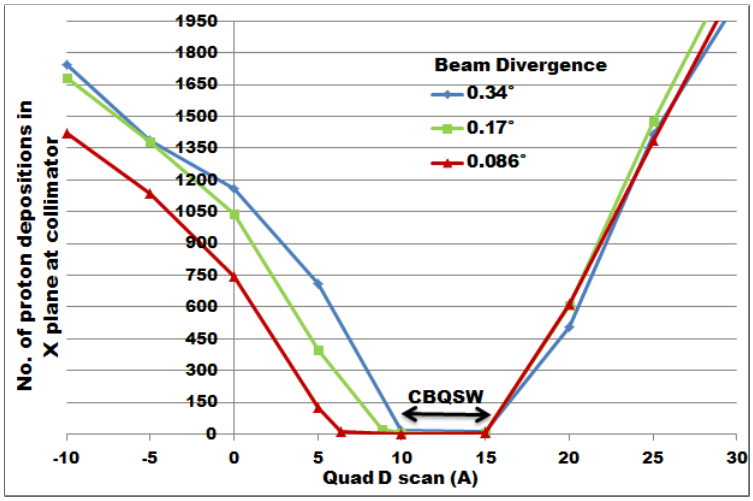

Figure 5.5: Quadrupole scan at different beam divergence in G4beamline simulations.

The quadrupole scan result at collimator, with 3 horizontal beam divergences in X plane is shown in figure 5.5. The beam positioning in vertical plane and total number of particles (10000) are identical for all three plots. The transverse emittance is defined in such a way (smaller emittance) that there is no deposition on collimator for a range of quadrupole scan. The range of quadrupole settings where there is no deposition on the collimator is giving an indicator proportional to the beam transverse emittance. As one can see "CBQSW" (discussed in section 3.3) is varying with beam divergence. For smaller beam divergence, the measured CBQSW is larger. This indicates an inverse correlation between beam divergence and CBQSW. Subsequently, the quadrupole scan with various beam σ in horizontal plane is also studied in simulations.

The quadrupole scan at collimator with various σ in X plane is shown in figure 5.6. The

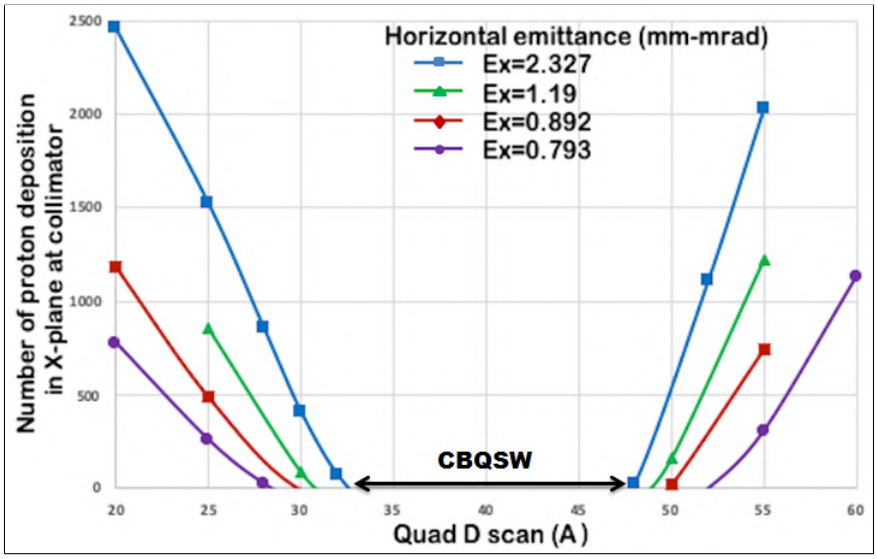

Figure 5.6: Quadrupole scan at different particle spread in X plane or σ_x in G4beamline simulations.

beam alignment (position) and the total number of particles (10000) are identical in both the transverse plane, for all four plots. It is observed that the CBQSW is varying in the same way as in the case of various beam divergence simulation. The smallest σ_x (Ex = 0.793 mm-mrad) is obtaining the largest CBQSW. This indicates an inverse correlation between transverse beam σ and CBQSW. Nevertheless, the nature of the curve is not the same compared to figure 5.5.

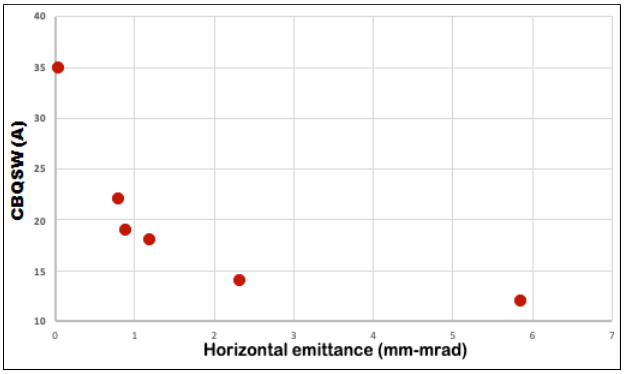

Figure 5.7: CBQSW at various transverse beam emittance in a horizontal plane (simulations) using fixed collimator dimensions.

CBQSW highly depends on collimator's physical dimensions and drift space between collimator and scanning quadrupole. The relation between CBQSW and transverse beam emittance is studied in simulations using identical collimator dimensions, similar to the ones in the high-intensity beamlines of ARRONAX. The correlation found between them (CBQSW and transverse beam emittance) follows an exponential curve and is shown in figure 5.7. It has been observed that for smaller emittance (<2 mm-mrad), CBQSW is varying rapidly. For horizontal

emittances close to 1 mm-mrad, there is a significant and rapid change in the magnitude of CBQSW. CBQSW is becoming linear due to collimator's limited dimension for larger emittances (>2 mm-mrad). It can be seen as a limitation of this technique to indicate transverse beam emittance. This technique includes a quadrupole scan that needs a well centered beam. CBQSW dependency on beam positioning at collimator, is studied experimentally and is discussed in section 5.3. As indicated in chapter 4, BLM's potential of transverse beam positioning indication is also studied in simulations and is discussed in next section.

5.2.3 Simulations of beam positioning with BLM

Due to the geometry with 4 active plates, the BLM has the potential to measure beam transverse positioning. However, BLM as a position indicator is a crude method to estimate beam positioning as it is used only when losses occur. An attempt has been made in G4beamline simulations (see the code in appendix B.2) to examine this indicator capability. Beam positioning in the simulations using BLM is studied by introducing a displaced beam in the simulated model at the entrance of the dipole. This dipole is the first element downstream of the extraction system as mentioned in chapter 3. Also, the beam positioning at BLM is being compared with the results of beam positioning at the collimator.

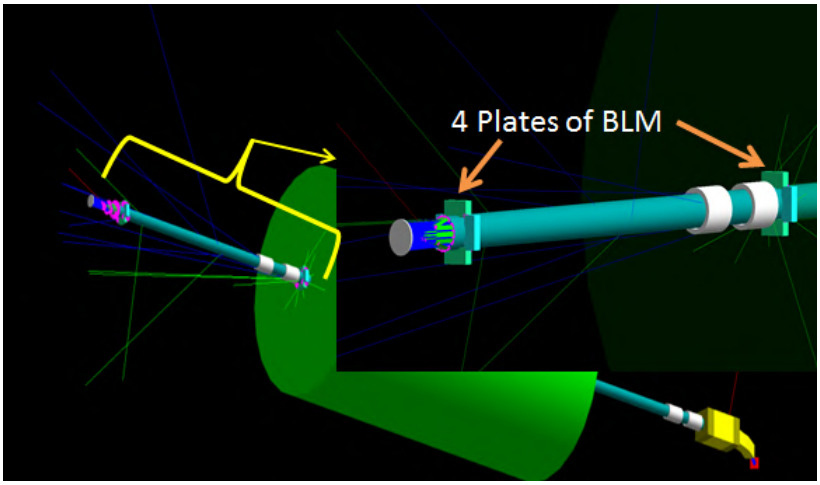

Figure 5.8: G4Beamline simulation model with BLM at ARRONAX (see the code in appendix B.2).

The geometric representation of the simulation model including the BLMs on the beamline is depicted in figure 5.8. An ideal detector (Virtual Detector) is being used to simulate BLM with 10000 particles and 70 MeV proton beam. The virtual detector in the simulations here

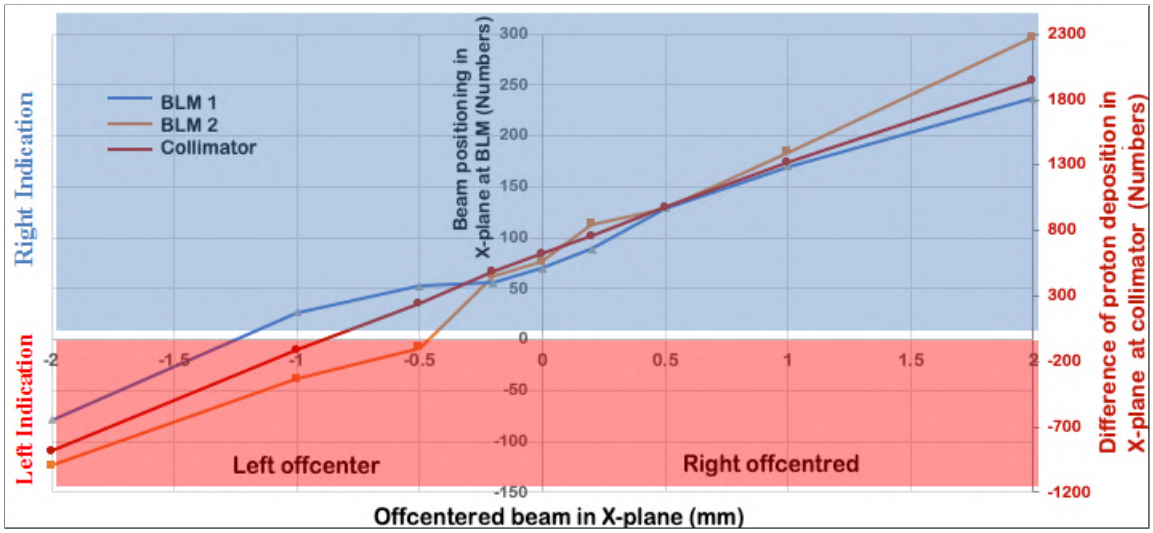

Figure 5.9: Comparison of BLM and collimator signals w.r.t. the off-centered beam. Negative represents left off-centered beam and vice versa (G4beamline simulations).

is made up of four parts to measure top, bottom, left, and right losses with similar geometry of actual BLM active plates. Similarly, the collimator is modeled without its outer casing. The initial setting of dipole is optimized to center the beam at the exit of the dipole. The beam definition is used such that BLM (simulated) can detect losses all the time. A position offset is then introduced at the beam origin. The collimator and both BLM responses are examined and local positioning is calculated (right-left) as shown in figure 5.9. It is observed that the positioning indication by BLMs and collimator follow similar trend on a large scale (over several mm of beam displacement). However, beam positioning indications, by both instruments when the displacement is small (below 1.5 mm), lead to responses that can indicate right off-centered beams for a left-centered displacement (for example: at -1 mm displacement on the figure 5.9). In this simulation, it shows that BLM and collimator positioning response will be similar if the beam is off-centered by more than 1.5 mm. In figure 5.9, the beam positioning at collimator is considered as a reference transverse positioning in a beamline. BLM 1 response depends on settings of the first pair of quadrupoles whereas, BLM 2 response can dominantly be influenced by the second pair of quadrupole settings. If a beam is off-centered at a quadrupole in front of BLM 1, the induced quadrupole kick can be seen by BLM 1 and BLM 2 can not see this displacement. As both BLM responses depend on different quadrupole pairs, they can indicate opposite beam positioning due to a kick, when the beam is slightly off-centered or the level of losses is very low. In other words, BLMs are showing their limitation to be used as a transverse positioning indicator, when the level of loss is very

low. In continuation of this study (see figure 5.10), an upstream quad B scan is performed in simulations.

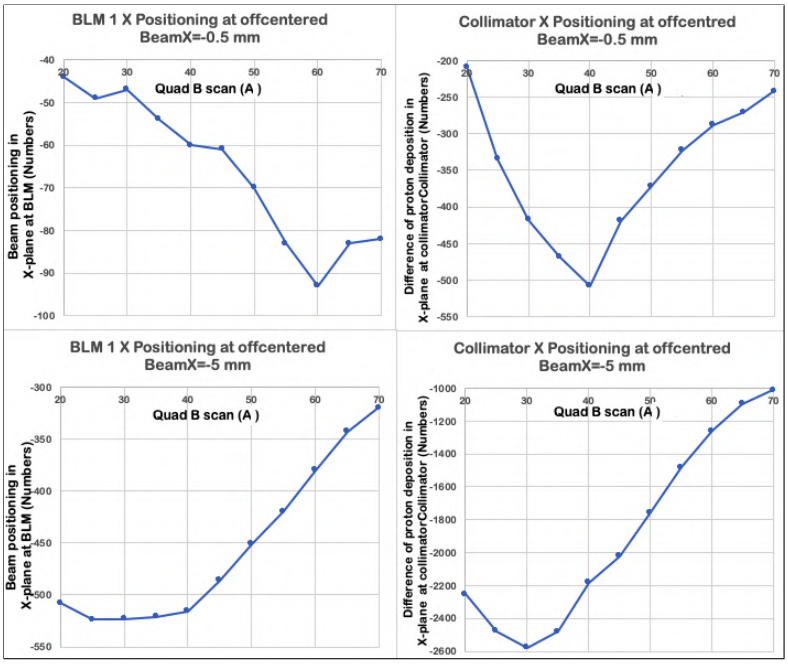

Figure 5.10: Comparision of BLM 1 and collimator response between -0.5 mm and -5 mm off-centered beam. (Simulations)

BLM 1 and collimator positioning are being compared with 0.5 mm and 5 mm left off-centered beam. As shown in figure 5.10, the quadrupole B scan is compared with two beam displacement (0.5 mm and 5 mm left off-centered). The negative sign (-0.5 mm and -5 mm) is the sign convention to represent a left off-centered or displaced beam. For -0.5 mm, BLM 1 and collimator indications are dis-similar. At quadrupole current 40 A to 60 A, BLM is indicating that the beam is left off-centered and it is moving towards left. On the other hand, the collimator is indicating that the beam is left off-centered and moving towards right. Similarly, a 5 mm left off-centered beam is being studied and both showed similar positioning indications during a quadrupole B scan. This implies that BLM 1 and collimator show similar beam positioning indication, when the beam is off-centered by margin (greater than 1.5 mm). Therefore, it can be concluded that when the beam is slightly off-centered (less than 1.5 mm), the beam positioning indication may contradict at BLM 1 and collimator. However, BLM 1 is showing potential of indicating the transverse beam positioning.

The opposite beam positioning indication from BLM and collimator have observed in one of the experiment. This has performed after machine settings optimization including beamline settings. In this experiment, a quadrupole scan of the first pair of quadrupole (Quad A and Quad

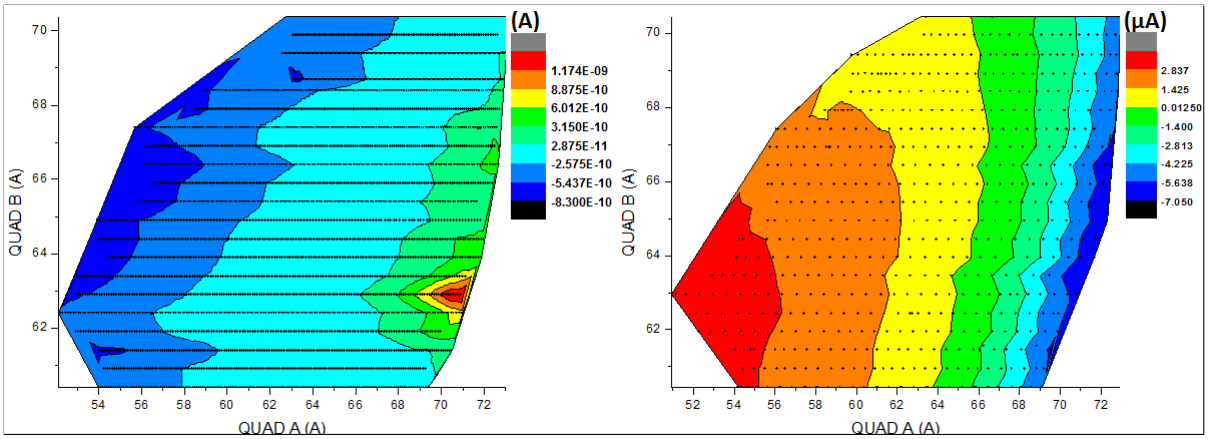

Figure 5.11: Experimental 3D mapping of 1st pair of quads in the high-intensity beamline. Left side showing horizontal positioning at BLM and right side at collimator.

B) is performed (see figure 5.11). Quadrupole A scan is repeatedly performed at several Quad B settings in order to obtain a quadrupole scan mapping. The beam positioning (right-left) results are then compared between BLM 1 and collimator. It is observed that collimator and BLM 1 positioning indications are contradicting. On the BLM side, the beam is mostly on the left side (data points with negative sign). On the other hand, the beam is mostly on the right side (data points with positive sign) at collimator. According to the simulations such contradiction is only possible when the beam is slightly off-centered. Thus, this can be concluded that the experimental setup on that day was optimal and the beam was close to center. Moreover, BLM 1 is showing potential in beam positioning indication. BLM as beam positioning indicator can be studied experimentally with BPM installed in a beamline.

In simulations, various studies concerning transverse beam trajectories, impact of transverse emittance at collimator by an upstream quadrupole scan, and potential of beam positioning measurement with BLM have been discussed. In the next section, the experimental observations on transverse beam dynamics studies in a beamline, is discussed.

5.3 Experimental Studies of Transverse Beam Dynamics

Beam dynamics can be defined as the study of charged particle motion in static or time varying electromagnetic fields. Here, the transverse beam dynamics of 70 MeV proton beam is studied in the high-intensity beamlines of C70 ARRONAX cyclotron. These studies include various branches such as beam in the presence of electromagnetic components (dipole and quadrupole),

focal point at the end-of-line (safer target irradiation), beam losses, transverse beam size, and positioning. The focal point at the end of line is studied in the high-intensity beamlines and is detailed in the next section.

5.3.1 Focal point studies at the end-line

The focal point at the end-line defines the transverse shape of a beam on the target as shown in figure 5.12) where A and B corresponds to two settings of the quadrupole. The size of the beam at the target location is larger for the focal point A than for B.

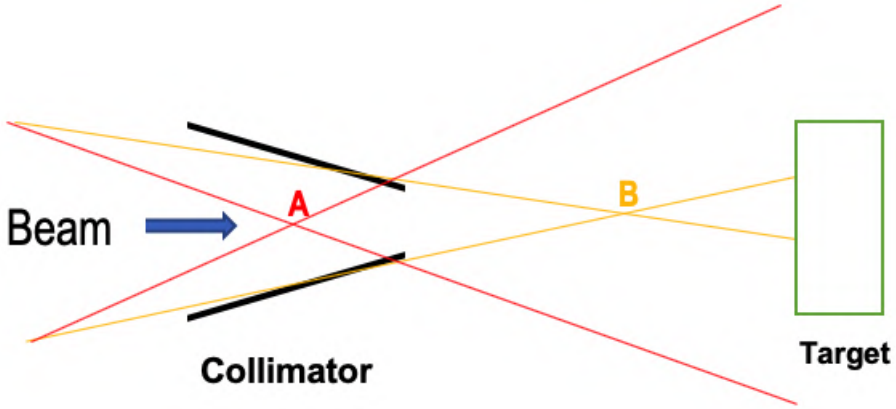

Figure 5.12: Example of the transverse beam shape on the target for two different focal point locations w.r.t. the collimator.

The prediction of the exact focal point is not possible without dedicated instrumentation. The collimator is placed upstream of the target. Thus, studies are performed to locate the approximate position of the focal point with respect to (w.r.t.) the end of line collimator location. This information can give good approximation of the transverse beam shape on the target. If we compare the experimental results at a lower intensity with a higher intensity beam, the focal point at the end of line should remain the same. At lower beam intensity, experiments will be safer from the point of view of damaging the machine and maintaining good vacuum pressure. There are no beam position monitors at ARRONAX cyclotron. Therefore, the collimator is being used for beam positioning measurement at the end-line. For this, collimator should have proton depositions all the time. It is only possible in two configurations when the focal point is in front of the collimator (e.g. x-plane) and another is behind the collimator (e.g. y-plane or vice-versa). So the limitations on possible focal point configurations are studied. Prior to this, a method is developed to locate the focal point w.r.t. the collimator by performing a 'single

quadrupole scan'.

Focal point with respect to the end-line collimator

The shape of the collimator at ARRONAX is as shown in the figure 5.13. We have taken advantage of this shape of the collimator to predict the focal point with respect to it in a single quadrupole scan. During the following tests, it is found that Quadrupole A and C are X-focalizing where B and D are X-defocalizing according to the standard configuration in high-intensity beamlines at ARRONAX.

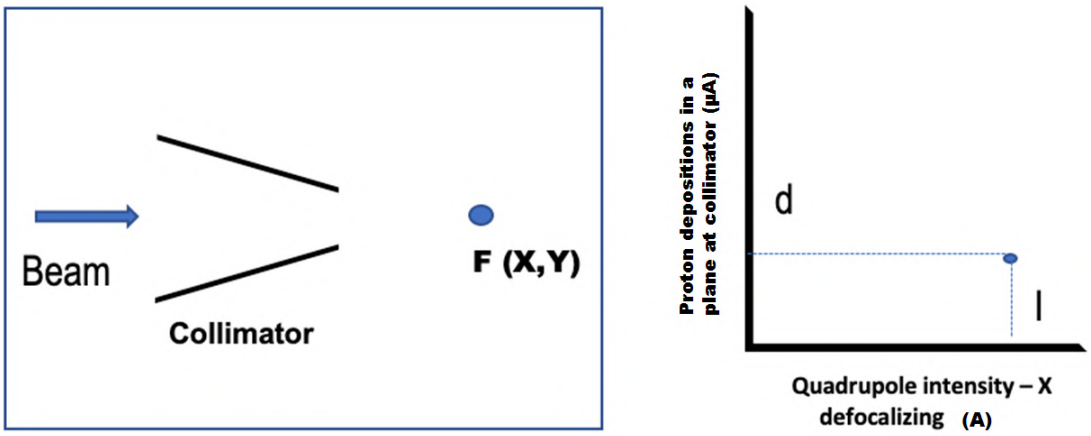

Figure 5.13: Example of the focal point at the same point behind the collimator. On the left, representation of focal point w.r.t. to collimator. On the right, corresponding local beam size in a plane at that quadrupole setting.

Let's take the example of quadrupole D which is X-defocalizing. Now lets assume that the focal points in both the planes are at the same point, behind the collimator. As shown in the figure 5.13, both focal points are located at point 'F' and quadrupole D is set at 'I' Ampere current with equal proton deposition 'd' on the X and Y planes at the collimator. The Quadrupole gradient is directly proportional to the current. Therefore, the focal point will move during a quadrupole scan with respect to the collimator. In the case of X-defocalizing quadrupole, any increase in current will move the focal point in Y towards and in X away from the collimator. It will eventually result in decreased signals in Y due to the beam envelop reduction in Y-plane. Similarly, Signals will increase in X due to the defocalization effect of the quadrupole in X-plane. So, it can be easily translated in terms of increase or decrease in proton deposition at collimator in X or Y plane. A quadrupole scan results in parabolic shape of the deposition versus the current and can be characterized in terms of a focal point with respect to collimator as shown in figure 5.14.

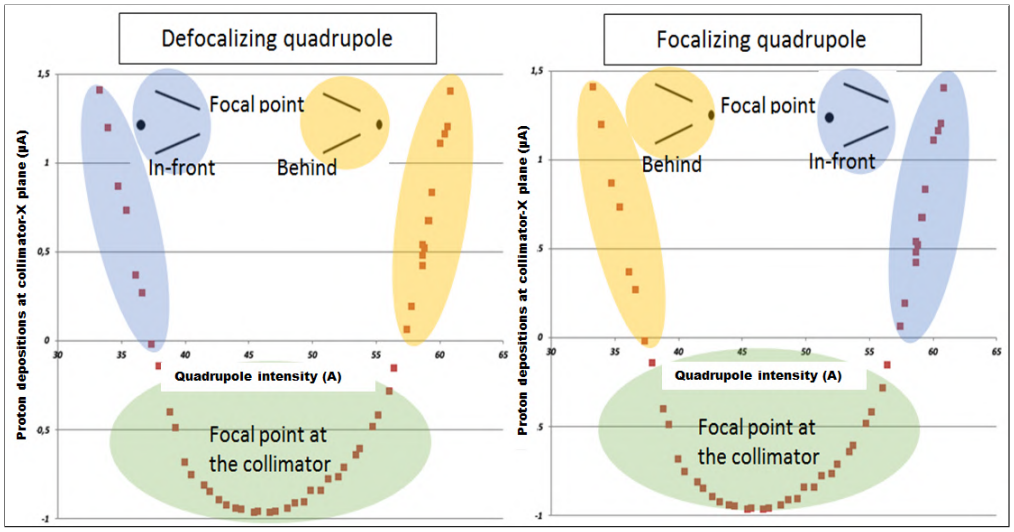

Figure 5.14: Example to illustrate the focal point w.r.t. to the collimator. On the left and right side showing defocalizing and focalizing quadrupole scan curve, respectively.

Particularly, figure 5.14 illustrates that with the quadrupole scan technique, the left descending part of the parabola curve (blue area) corresponds to the focal point being in front of the collimator with a de-focalizing quadrupole. With a focalizing quadrupole the same part of the curve corresponds to the focal point (yellow area) being behind the collimator. When the focal point is at is 'at' or 'close' to the collimator (green area), one can see continuity in the negative signals. The negative signal is due to calibration offset at ARRONAX.

Focal point with respect to the beam intensity:

Quadrupole scans can only be performed on a limited range at standard operational beam intensity (approximately 150 µA). At high intensity, the impact of losses on vacuum or the density of the beam on the target when performing the scan, can cause rapidly uncontrolled damages. Thus, the technique is applied at lower average intensity than standard operation. To check the impact and difference of beam intensity on the result of the quadrupole scan several beam intensities are used: 10 µA, 30 µA, and 50 µA. The experiment has been first tuned at 10 µA beam on target. The source current is then used to increase the beam intensity as performed for standard operation.

As shown in figure 5.15, beam intensity used for a scan is 10 µA, 30 µA, and 50 µA represented with different colors. The plots are normalized at 10 µA level. Quadrupole scans are performed in such a way that one can see loops in the curves which shows the effect of hys-

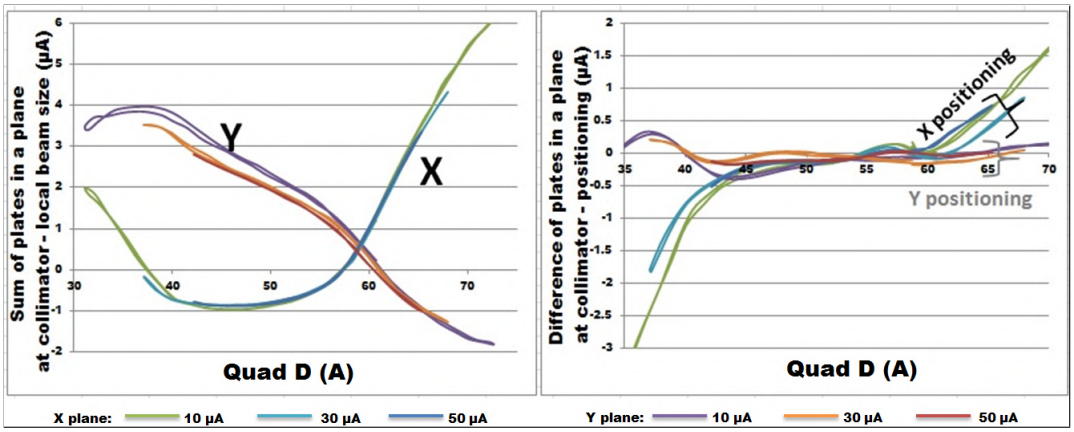

Figure 5.15: Comparison of Beam size changes and positioning as function of quadrupole current with different beam intensity on same day. Plots are normalized at 10 µA total beam current.

teresis of quadrupole magnetic field. Quadrupole scans showed similar shape, focal point, and positioning. With an increase in beam intensity, the focal point is not getting affected much which means a focal point on the same day (i.e same machine settings) at 10 µA beam will be the same for beam at a much higher intensity. At 10 µA, the quadrupole scans are more secure from the point of view of vacuum and allows to extend the range of the scans. This range can be observed in the plot itself. The quadrupole range of the scans are 32 A to 70 A, 38 A to 68 A, and 42 A to 64 A for the scans at 10 µA, 30 µA, and 50 µA, respectively. This difference in the range used to do the scan is due to the limitation of vacuum pressure at higher beam intensities (higher level of beam losses at sensitive locations at higher beam intensities).

Limitations on focal point:

The collimator is placed upstream of the target so it is essential to know the focal point at the end-line because it defines the dimension of the beam on target during irradiation as discussed earlier. This has been studied by performing a quadrupole scan mapping (2nd pair of quad QC-X focalizing, and QD-Y focalizing upstream of the collimator) experiment at 5 µA beam on target as shown in figure 5.16. This 3D mapping has been created by performing QD scan at four QC settings shown with dotted points (see figure 5.16). The same discussed above method is implemented to predict the location of focal point w.r.t. the collimator. The pair of quadrupole (placed upstream of the collimator) are scanned and it is observed that the focal point in front of the collimator is not possible in the high-intensity beamlines at ARRONAX.

When the focal point is in front of the collimator in any plane, it results in a large beam envelop size in the other transverse plane. This envelop size is large enough to detect losses at BLM 2. One can see bottom two plots in figure 5.16, BLM 2 is detecting losses in a plane, when the focal point is in front of the collimator in the other transverse plane. The same results are obtained in the beam envelop simulations and discussed in section 5.2.1. Therefore, the focal point should be always behind the collimator in the high-intensity beamlines during operations. In figure 5.16, the focal behind the collimator (both the transverse plane) can be associated at QD=40 A and QC=-35 A, with approximately equal deposition (≃0.5 µA) on each plane.

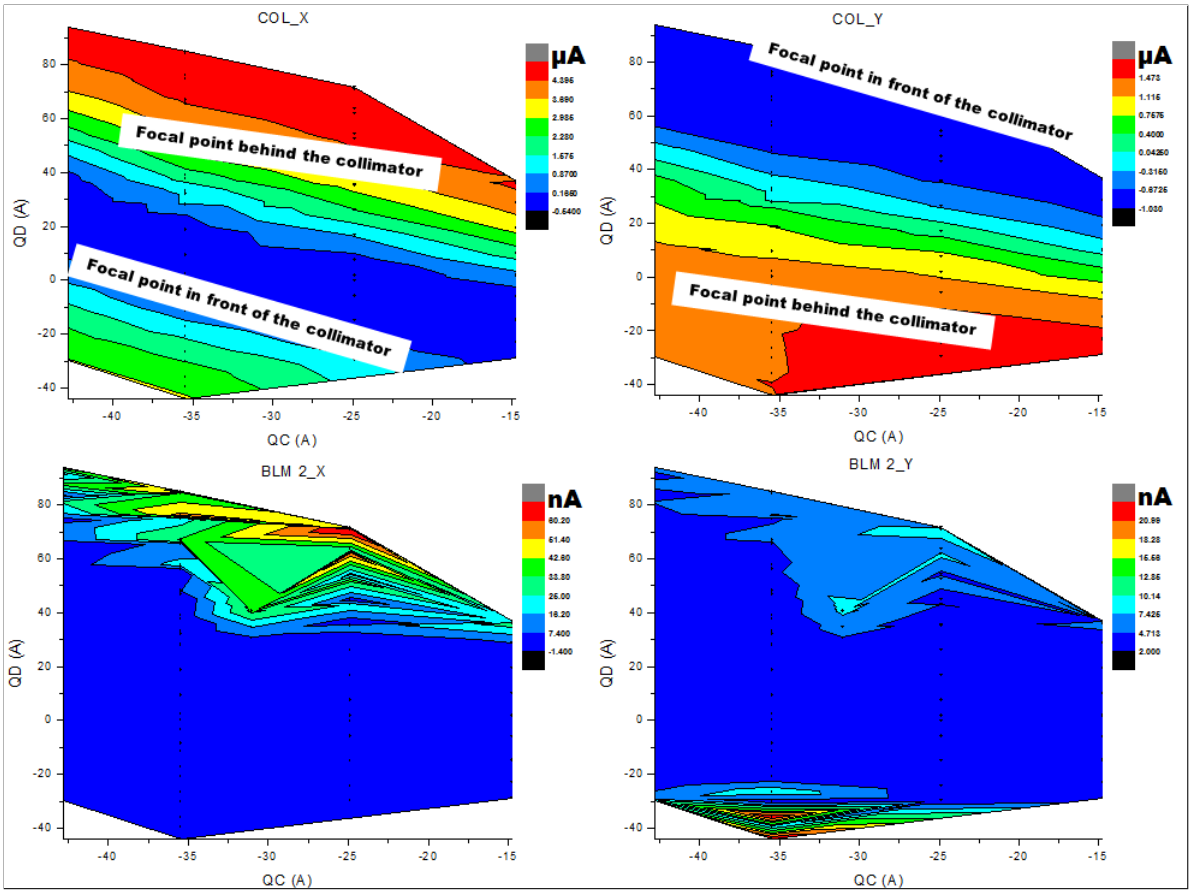

Figure 5.16: 3D mapping of local beam size in X and Y at collimator and BLM where QC and QD are a pair of quads upstream of the collimator. The coloring represents the interpreted intensity level on the collimator and BLM. The black dots in the plot show the actual data points.

For irradiation runs, there is a protocol, operators follow to have approximately 8% total proton deposition equally distributed on the collimator's finger. The above experiment indicates that it is possible only when the focal point is behind the collimator in transverse plane. Thus, the focal point is always behind the collimator, during standard irradiation runs in the high-intensity beamlines of ARRONAX. The irradiation runs should be stable and the beam

positioning is one of the essential parameter that ensures stable beam in a beamline.

As discussed in the "Initial Studies" section, the stripper foil azimuthal settings help to align the beam in a beamline. Preliminary studies have been performed in the beam alignment work of Shuang NING [71]. Below, stripper foil azimuthal settings are experimentally further investigated to examine the underlying physics.

5.3.2 Stripper foil studies

As presented below and detailed after, several experiments have been performed to find the dependency of beam positioning with other settings for the beamline or the cyclotron. The instrumented collimator is used to measure local beam positioning (difference of proton deposition in a transverse plane). The Methods to reduce these beam displacements are also essential for operators to perform more stable operations. Beam dynamics will improve if operations manage to have a centered beam. We have already discussed in section 2.1.6 that the extraction of proton beam in a beamline by using "diamond like carbon" stripper foil. An off-centered beam gets a dipole kick with a quadrupole scan and it modifies the dimension of the beam at the collimator. Stripper foil settings are found to help stabilize the beam by reducing those beam displacements during quadrupole scans. At ARRONAX, the azimuthal setting of the stripper foil is an adjustable parameter. In this section, stripper foil azimuthal settings have been studied followed by an upstream quadrupole scan. The impact of stripper foil azimuthal settings on collimator is examined.

At first, the experiments are performed to check the robustness of stripper azimuth settings. This is done to check the repeatability in the sum and difference (positioning) of proton depositions in a plane at collimator during an upstream quadrupole scan on the same day. For such experiments, the quadrupole scans are performed at several stripper azimuth settings twice or thrice with a tuned machine on the same day. The results of these experiments have indicated that these settings are robust enough to produce exact same results of sum and difference of proton depositions in the transverse planes at collimator on the same day. Also, it was found that stripper azimuth settings do not have any effect in the vertical positioning and have only an impact on the horizontal positioning. Besides this, the vertical positioning is close to the center and relatively stable during a quadrupole scan.

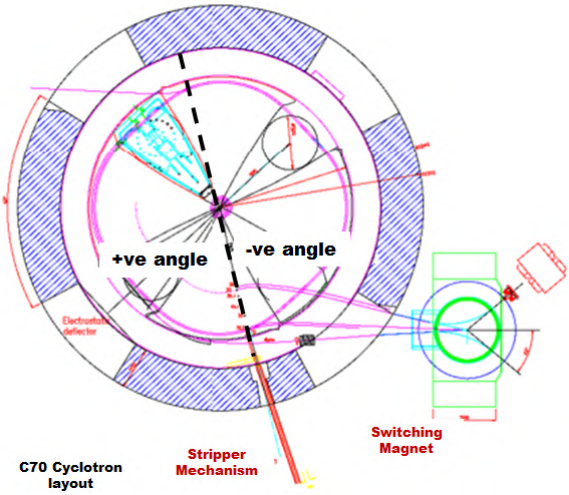

Figure 5.17: Illustration of the trajectory of the particle wrt to the radial position of the stripper foil. The stripper foil is in a central azimuth position, and positive and negative angle represent left and right movement, respectively [7].

The azimuthal settings vary the angle of the stripper foil. During operation, the stripper foil azimuthal setting is referenced by the mechanical displacement of its rod, and is in "mm". This position is transformed (for the equation to convert mm to degrees see appendix C) in an angle to keep the consistency with the simulation model and the reference to the beam view point. With this view, the tilt to the right is referred to the negative angle and the left to the positive one, as illustrated in figure 5.17.

Quadrupole scans with varying stripper foil azimuthal settings:

The experiments are performed to study beam positioning in horizontal plane (collimator) at various stripper foil angles as shown in figure 5.18. As one can see, the stripper foil azimuthal location helps to mitigate the measured beam displacement in horizontal plane by centering the beam during a quadrupole scan. The angle of the stripper foil with respect to the central position of the cyclotron ranging from $-0.74°$ to $-1.06°$ in steps close to $0.03°$.

In figure 5.18, the different colored solid lines are showing quadrupole scans at various stripper foil angles. The measurements are normalized to the same 'total beam current' (as discussed in chapter 4). Each measurement indicates by how much the beam moves horizontally when the intensity on the quadrupole is modified and shows that each angle setting has a different impact on the position. Above 60 A, the slope of position's change is positive for angles below $-1°$ and the slope increases as the angle decrease. The slope becomes negative for angles

above $-1°$. The minimum beam displacement in the horizontal plane is observed at stripper foil angle close to $-1°$ within the range of stripper settings examined in this experiment. This setting modification has no influence on vertical beam positioning.

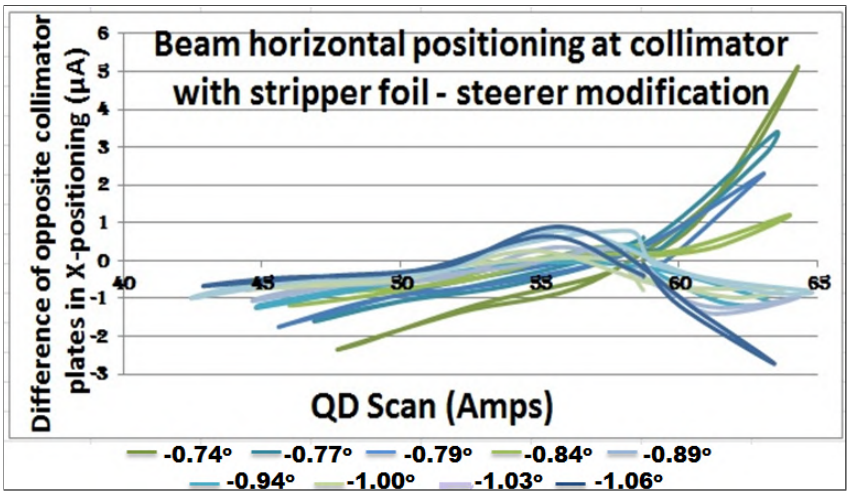

Figure 5.18: Beam positioning as a function of quadrupole current with stripper foil (angles) – steerer modification.

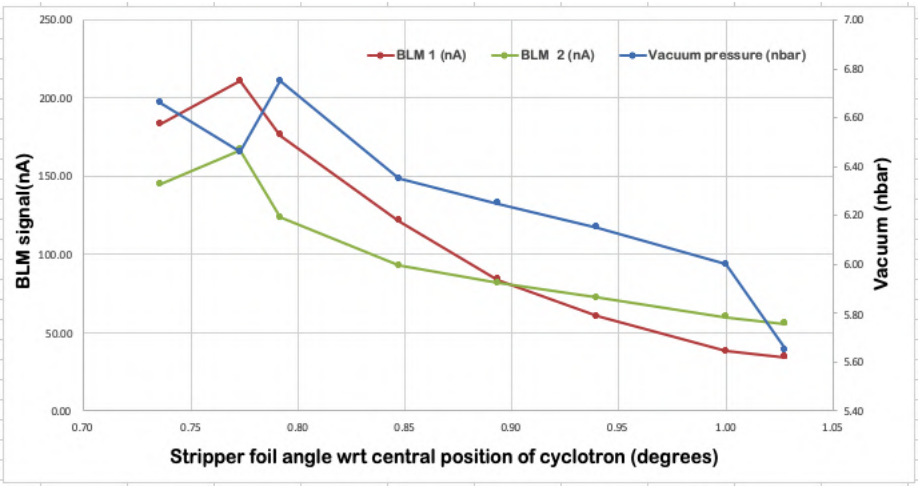

Figure 5.19: Response of BLM 1 and beamline vacuum pressure with stripper foil azimuthal settings (angles) modification.

In high-intensity beamlines, beam envelop size is large at sensitive locations [69] and beam losses at those locations affect vacuum pressure. As shown in figure 5.19, it has also been observed that, with a centered beam, BLM signals have significantly reduced by 80% in both the transverse plane and results in a lower vacuum pressure (15% improved). The range of quadrupole scan is limited to 20 A (45 A to 65 A - see figure 5.18). The losses are particularly high at 50 µA (used beam intensity in the experiment) resulting in losses upstream of the collimator. This ultimately has resulted in an increase in vacuum pressure i.e. limiting the range.

Thus, these quadrupole scans are not able to obtain a complete parabolic shape (sum of proton deposition at collimator).

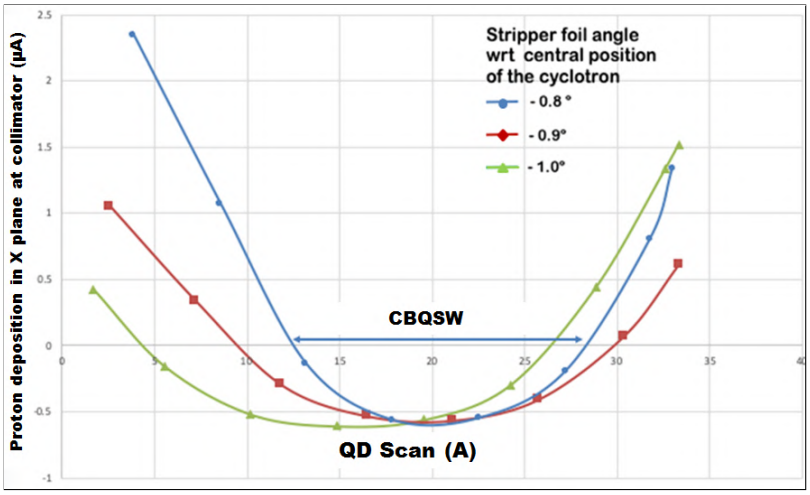

Figure 5.20: Quadrupole scan at different stripper foil angle w.r.t. central position of the cyclotron on the collimator.

A similar experiment was performed at 5 μA beam intensity in order to achieve complete parabolic shape. The sum of proton depositions, during an upstream quadrupole scan at various stripper foil angles on collimator in horizontal plane, is shown in figure 5.20. As one can see, the Collimator Based Quad Scan Width (CBQSW) is varying at various stripper foil angle. During experiments, a change in CBQSW has never been observed with the other elements (Injection line settings and main coil) of the machine. In the simulations, a change in CBQSW has only been observed with distinct transverse beam emittances (particle spread and beam divergence). These quadrupole scan results have shown similar tendency to the result of simulation of the quadrupole scans at various horizontal beam divergence and is shown in figure 5.5.

In figure 5.20, the $-0.8°$ angle (blue curve, plain dot) is giving the smallest CBQSW and, the largest angle of $-1.0°$ (green curve, plain triangle) is delivering the largest width. As discussed above, the minimum beam displacement (transverse positioning) in horizontal plane is being achieved at stripper foil angle close to $-1°$ (see figure 5.18).

The experimental results of quadrupole scan at various stripper azimuth settings are indicating that the stripper foil azimuthal settings impact both, the beam orbital trajectory at the beam extraction in a beamline and the horizontal beam divergence. Because of these impacts, CBQSW depends on beam positioning. Therefore, in the following paragraph, CBQSW dependency on beam positioning is being investigated in the following paragraph to verify if the

horizontal beam divergence is causing this change in CBQSW.

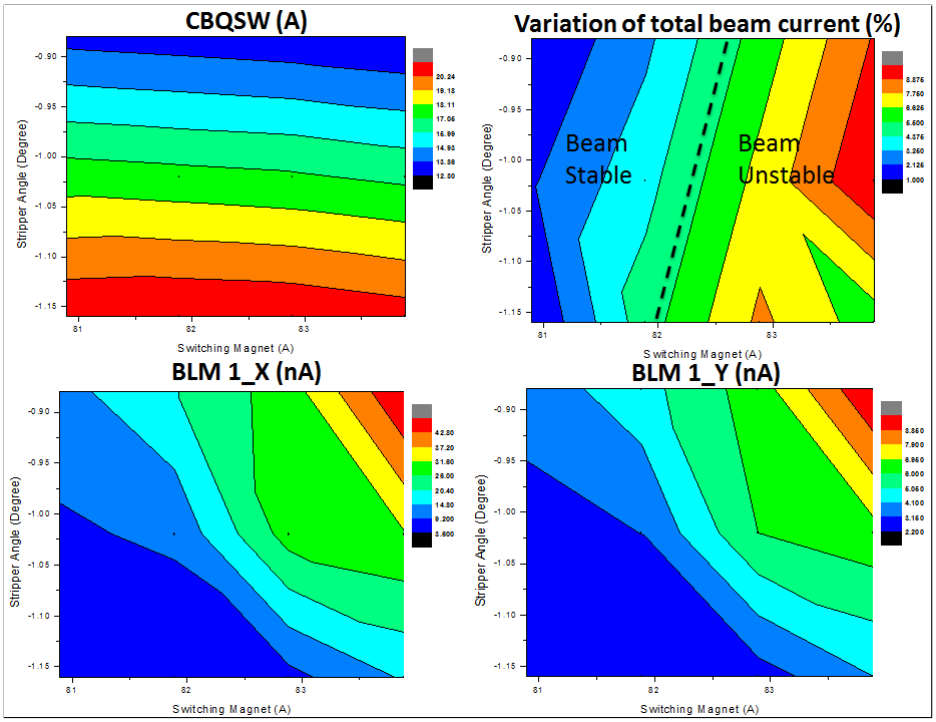

Figure 5.21: 3D mapping of stripper angle and switching magnet settings. Top left plot shows Collimator based Quad scan width (CBQSW), Top right shows variation of total beam current during quadrupole scans, Bottom left shows BLM 1 signal in X plane, and Bottom right shows BLM 1 signal in Y plane. The plots obtained on the Top (both) is showing mapping from quadrupole scan results and on the Bottom (both) is showing mapping at various combination settings of stripper angle and switching magnet.

This is examined by performing quadrupole scans at four switching magnet settings ranging from 80.89 A to 83.89 A with step size of 1 A. Furthermore, these quadrupole scans with the range of switching magnet settings are performed at three settings of stripper foil azimuth i.e. $-0.88°$, $-1.02°$, and $-1.16°$. This experiment is performed at 5 µA beam current. This has created a mapping of switching magnet and stripper foil azimuth settings. These 3D mappings are shown in figure 5.21. In the top left plot, the 3D mapping of CBQSW is shown with an upstream quadrupole scan at various stripper angle and switching magnet settings.

This can be depicted from the plots that CBQSW does not depend on the switching magnet. However, a change of ± 0.4 A in CBQSW is observed due to $\pm 10\%$ displacement in Y beam positioning (positioning is already discussed in figure 3.8). In the top right plot, the 3D mapping of the total beam current shows fluctuations during an upstream quadrupole scan as discussed in chapter 3. The higher fluctuations in the total beam current (greater than $\pm$ 5%) imply that the

beam is unstable or off-centered by a margin and it is getting higher kicks during a quadrupole scan. Also, this can be inferred that switching magnet setting should be lower than 82 A for stable beam operations. In the bottom plots, one can see that the level of losses have increased in both the transverse plane, when the beam is unstable. There is a correlation that can be observed, between variation of total beam current and beam losses at BLM. This experiment is indicating that CBQSW in X plane depends on Y positioning and stripper azimuth settings do not have any impact on Y positioning. Thus, stripper foil azimuth angle is influencing beam divergence in a beamline and variation in the CBQSW is acting as an indicator.

Discussion

When foils are placed in the path of a beam to strip ions, the Coulomb scattering [87] upon transition through such an obstacle leads to an increased angular beam divergence. This increase in the angular beam divergence can be estimated by using the classical multiple scattering formula [35] discussed in equation 2.22. This leads to an increase in RMS emittance which is independent of the initial emittance and is proportional to the value of the focusing function (β_x) at the foil (see equation 2.23).

In G4Beamline simulations, this is simulated with 1 million proton (70 MeV) events and identical beam definition (σ and angle) in transverse plane. A virtual detector is placed 60 cm downstream of the origin of a proton beam (see figure 5.22) in a vacuum environment. At first, beam angular divergence is measured on the virtual detector which is found to be equals to the defined initial beam angle. When the stripper foil (800 nm carbon foil with 10% boron doped) is placed 50 cm upstream of the virtual detector, an increase in the angular beam divergence of 0.4 mrad in both planes is measured on the downstream virtual detector. There is no significant change in the observed beam divergence with the angular change of the foil.

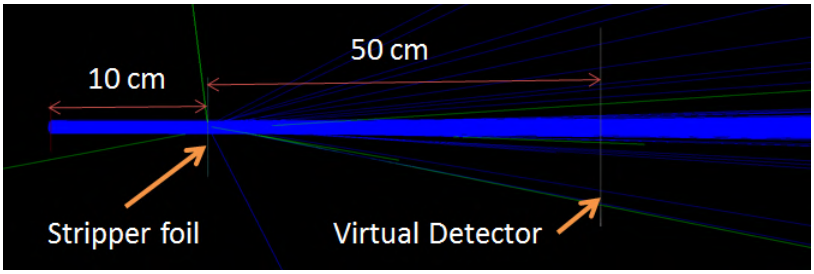

Figure 5.22: Simulation model of Stripper foil at ARRONAX.

The stripper foil displacement mechanism is found responsible for these observed experi-

mental results as discussed below. The stripper foil displacement mechanism at the C70 ARRONAX cyclotron is based on the articulation of a long supporting rod with respect to the hinge joint as shown in figure 5.23. The supporting rod mechanism translate horizontally on a bed with the stripper foil azimuth setting variation. The magnitude of translation on this bed is translated into tilt angle of the foil. At the same time, there is a change in horizontal position of the foil which is equivalent to the magnitude of horizontal translation on the bed. Therefore, the interaction point of H^- beam with foil will be discrete which will lead to a distinct horizontal beam orbital trajectory. At a particular azimuth setting, the beam orbit will match the centre of selection magnet (switching magnet). Moreover, the foil will fall in a different magnetic flux density zone of the azimuthally varying magnetic field of the sector magnet. Due to this, the Lorentz force acting on proton beam will vary. This has an impact on the radius of curvature of the proton beam after electrons stripping by the foil. This change in the radius of curvature can also have a direct impact on beam divergence.

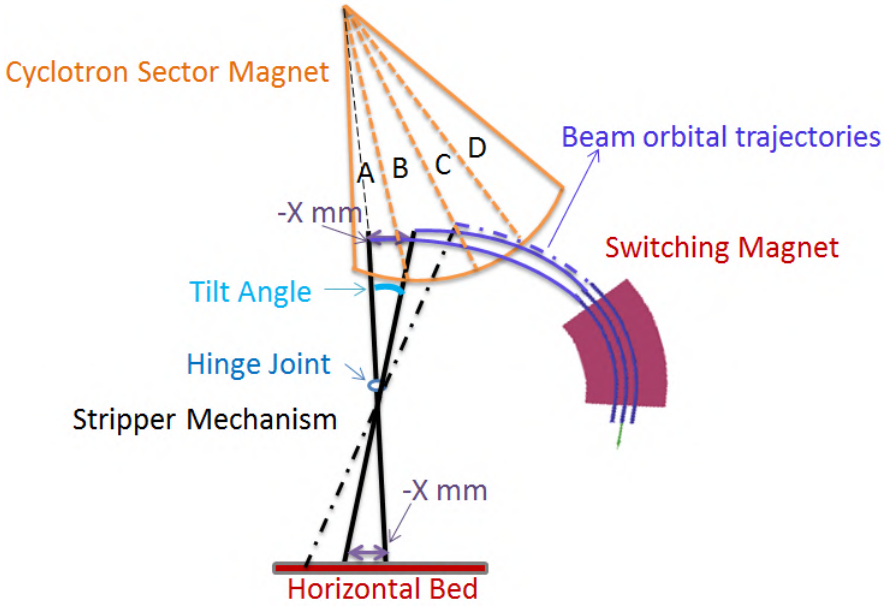

Figure 5.23: Illustration of stripper foil azimuthal settings mechanism of C70 ARRONAX cyclotron. A, B, C, and D is showing the azimuthally varying magnetic flux density of the cyclotron sector magnets.

Calculations are performed to estimate the magnitude of Lorentz force with the stripper foil azimuth settings which is based on IBA's calculation on azimuthally varying field of hill and valley sector magnets of the cyclotron [13]. It has been found that there is an increase of approximately 9 Gauss magnetic flux density per mm change in the stripper foil azimuth setting at 1166 mm cyclotron's radial length (the position corresponds to a 70.3 MeV proton

beam extraction point). This results in a change of proton beam's radius of curvature due to a increase in the Lorentz force. This radius of curvature is calculated by equating Lorentz force and Centripetal force (see equation 5.2).

$$r = mv/qB \tag{5.2}$$

where r is the radius of curvature of the path of a charged particle with mass m and charge q, moving at a speed v perpendicular to a magnetic field of strength B.

The azimuth settings, examined in the experiments, are ranging from -16 mm (- 0.74º) to -25mm (-1.15º). There is approximately 2 mm reduction in the radius of curvature of proton beam and orbital change is in the order of 7 mm. In the experiments, this is the main reason behind a change in beam positioning and divergence in a beamline with stripper azimuth settings. So, due to the scattering of the beam on the stripper foil, an increase of beam divergence takes place and is reduced by re-adjusting the optics in the downstream beamline. There is a possibility of getting an impact from de-focalizing effect of cyclotron fringe fields which is not studied here.

The blow-up of the RMS emittance is directly proportional to the foil thickness (see equation 2.22). If we change the stripper foil thickness then there should be a noticeable effect on CBQSW with the same settings on the same day. This has been studied and discussed in the next section.

Quadrupole scans with different types of stripper foil

A typical long irradiation runs for isotope production lasts for more than 100 hr and is of the order of 130-150 µA on target. During these irradiation, stripper foil degrade due to a rise in temperature and radiation effects damaging the foil [86]. To explore the effect of the foil modification due to the irradiation, quadrupole scans are performed and, an irradiated foil (integrated current on the foil 23486 µAh) is compared with a pristine stripper foil on the same day. This experiment is following an optimization of the machine and the exact same settings are used with both the foils. The quadrupole scan is performed at -0.76º and -0.86º stripper foil angle w.r.t. central location of the cyclotron. The results of the beam positioning at the collimator are found to be identical. However, CBQSW with irradiated foil is found smaller

compared to pristine foil: a difference of 5 A in CBQSW has been observed after comparing results. This indicates that the beam emittance increases over time due to the foil damage with the extraction process using the stripper foil.

After this experiment, three stripper foils are compared similarly at -0.85° foil angle in the same beamline on the same day. The specifications of these foils used are given below:

- Pristine 800 nm (Standard) Diamond like Carbon (DLC) Foil.
- Pristine 1500 nm Multi-layered graphite like properties (GRM) Foil.
- Irradiated (26879 µAh) 800 nm DLC Foil.

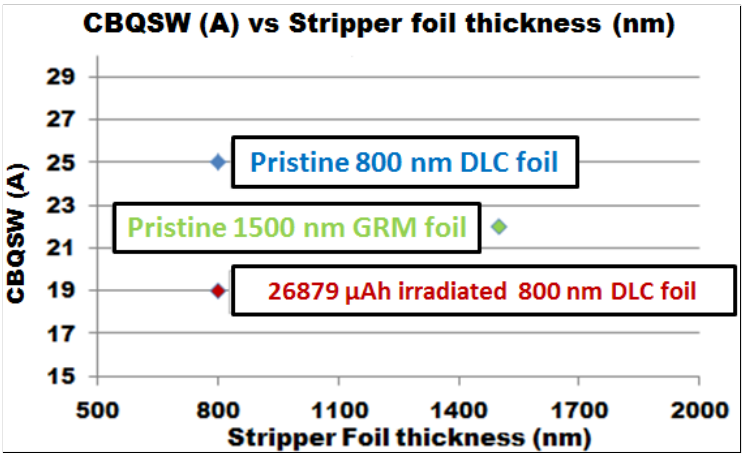

Figure 5.24: Variation in the CBQSW during a quadrupole scan w.r.t. stripper foil thickness and condition (radiation damage).

The measured CBQSW by an upstream quadrupole scan with distinct stripper foil thickness and condition (integrated beam current) is shown in figure 5.24. The lowest transverse emittance is obtained with pristine 800 nm DLC foil (25 A CBQSW) and the highest is for an irradiated 800 nm DLC foil (19 A CBQSW). The pristine 1500 nm GRM foil's CBQSW comes in between i.e. 22 A. The quadrupole scan results of this experiment is showing that foil thickness affects the beam emittance growth though foil damage plays a possibly more important role in the emittance growth. A thicker foil is mechanically more stable and gives better electron stripping efficiency. However, a thicker foil results in higher beam loss and emittance growth through scattering. Large angle elastic scattering and inelastic scattering are assumed to result in beam losses, while multiple Coulomb scattering gives a small angle increase and blows up the circulating beam emittance [96]. The choice of optimum foil thickness is a compromise between these effects.

This experiment is indicating that there is a need to study foil damage over time. To probe the effect of time, and as a preliminary work, CBQSW has been measured for foils cumulating intensity from 0 uAh to 25000 uAh as shown in figure 5.25. This can advocate to put a threshold on foil's deposited intensity integral (µAh) and lead to the decision of an installation of a new foil once the old foil has reached the threshold.

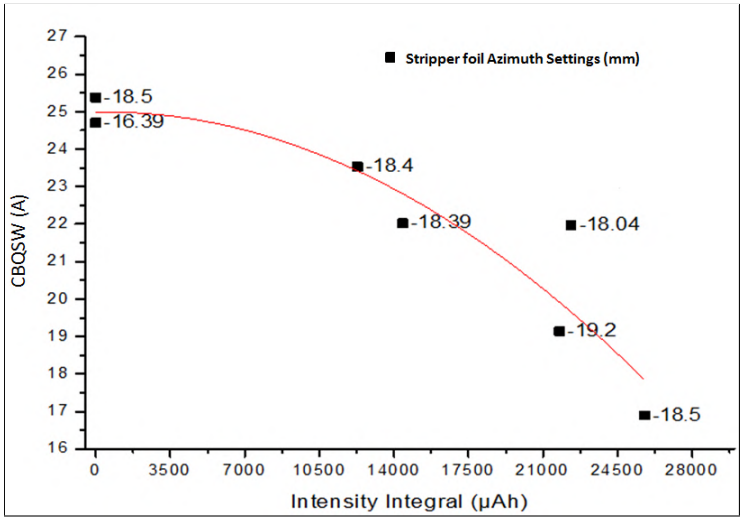

Figure 5.25: Measured CBQSW as a function of intensity integral on stripper foil following irradiation runs along with stripper azimuth settings (mm) at the time of various measurements. The curve in red is showing the tendency.

The measured CBQSW versus the intensity integral are plotted with their respective stripper foil azimuth settings in mm (black squared dots). A total of 7 quadrupole scans results (measured CBQSW) are shown in this plot. The differences of the beam y-positioning, as measured on the collimator, of each scan is neglected to obtain this plot. Regardless of this fact, one can see the tendency of CBQSW with intensity integral on a foil that is shown with the red fitting curve. The result indicates that the transverse beam emittance is increasing as the foil is aging.

In the previous section, we have performed various studies to verify that CBQSW is inversely proportional to the transverse beam emittance in a beamline. The magnitude of this change in transverse beam emittance with stripper azimuth settings is also investigated.

5.3.3 Transverse beam emittance measurement

We have already discussed the low-intensity beamline in chapter 3.1.2. This beamline is equipped with a single wire profiler. Therefore, it is the best-suited line for transverse emittance measurement. This emittance measurement technique with a single wire profiler [40] includes

a quadrupole scan without any magnetic element or, obstacle in the drift space between the scanning quadrupole and profiler. A collimator has been placed behind the profiler in a similar "way" as the previously used beamline. The profiler was installed adequately but the placement of collimator downstream of the profiler in vacuum was not possible mechanically. Thus, the collimator is placed in the air downstream of the profiler so that results from the profiler and collimator can also be compared (see figure 5.26).

The experimental setup for the transverse emittance measurement is shown in figure 5.27. The X-focalizing quadrupole, which is placed upstream of the profiler, is being scanned . The location of the quadrupole and position of the profiler creates a drift space of 127.6 cm. The shape of this collimator is similar to the collimator in high-intensity line with exit diameter of 10 mm. The experimental setup also includes a large instrumented beam dump, used as a proton intensity monitoring reference, with a 99.5% accuracy.

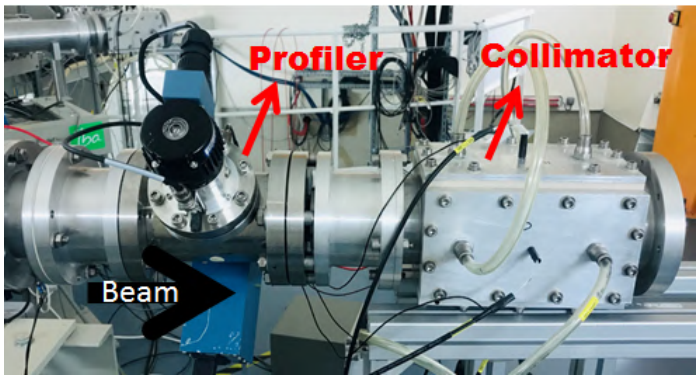

Figure 5.26: Experimental setup for transverse beam profile measurement where collimator is placed outside vacuum chamber.

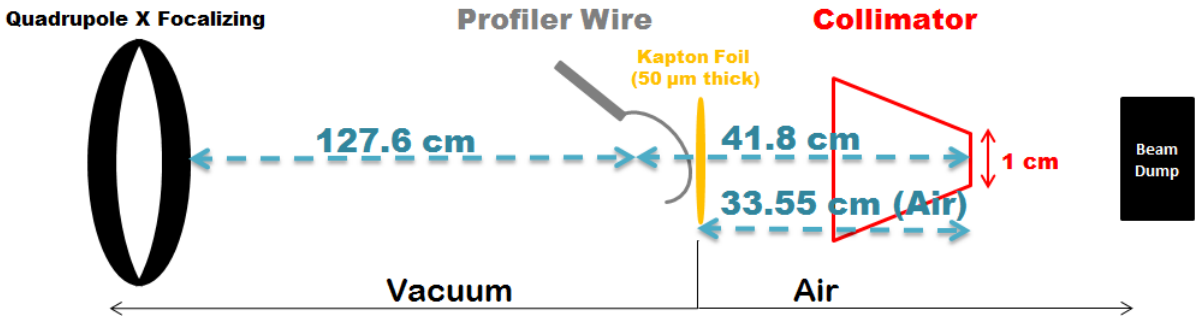

Figure 5.27: Measurement of the drift space between quadrupole, scanning wire and collimator.

The single wire profiler's model "BPM80" is from National Electrostatics Corporation (NEC). The BPM80 includes molybdenum wire with a 0.5 mm diameter. It has a housing and a

pre-amplifier. The housing has a nominal diameter of 10 cm with a 2.54 cm diameter molybdenum beam entrance aperture. A magnetic coupling is used to transfer motion into the vacuum pipe for rotating the scanning wire. The wire sweeps across the beam twice during each revolution. It gives a Y profile in a half revolution and X profile during the second half revolution. This scanning wire is surrounded by a collector cylinder which picks up generated secondary electrons from the wire. This collected secondary electrons pass through a pre-amplifier stage. This signal is then sent to an oscilloscope for profile visualization and for downloading the profile measurement data. The oscilloscope used here is from "Agilent Technologies model DSO7054A Oscilloscope: 500 MHz" with 4 analog channels. An in-house made filter is also utilized to reduce noise from scanning wire vibrations during measurements.

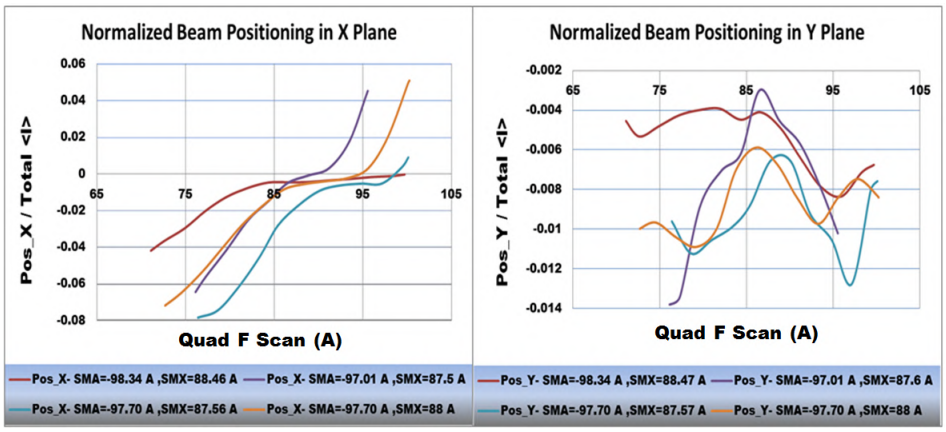

Figure 5.28: Beamline tuning with dipole magnets for best positioning during a quadrupole scan.

For beamline tuning, a pre-installed library, optimized for a low-intensity line, is used. The library settings are further optimized for the best transmission. Quadrupole scans have been performed with dipole modifications in order to find better beam positioning if possible. The beam positioning results at various combination of dipole settings arre shown in figure 5.28. The beam positioning results are normalized at 1 nA level by dividing by the total beam current (nA). The best positioning in both planes is found at SMA=-98.34 A (the first dipole downstream of the beam extraction point) and SMX=88.46 A (the second dipole upstream of the beam extraction point) which is shown in red color. At this setting, the beam is most stable as it is getting lesser kicks during a quadrupole scan. The transverse profile measurement is being performed with three different stripper foil azimuthal settings i.e. -17.2 mm (-0.8º), -19.2 mm (-0.89º), and -21.2 mm (-0.98º). For each stripper foil setting, the beam centering at the collimator is being done by optimizing steerer X settings (stripper azimuth settings affect horizontal

beam positioning only) prior to quadrupole scan for profile measurement. A quadrupole scan is performed with a step size of 2.5 A per measurement. The range of the quadrupole sufficient for profile measurement in both the X and Y plane has been decided by a developed OPI during the course of this work and is mentioned in chapter 3, figure 3.18. The range of quadrupole scan found is from 50 A to 115 A for transverse profile measurement.

During a quadrupole scan at each setting, beam profile data from the oscilloscope and collimator particle deposition are recorded and analysed for later comparison of CBQSW with the RMS emittance at three different stripper foil azimuthal settings. As shown in figure 5.30, transverse beam profile data from the oscilloscope is fitted with a Gaussian curve of the equation written below:

$$y = y_0 + A * exp(-0.5 * ((x - x_c)/w)^2) \tag{5.3}$$

The equation 5.3 is illustrated in the figure 5.29.

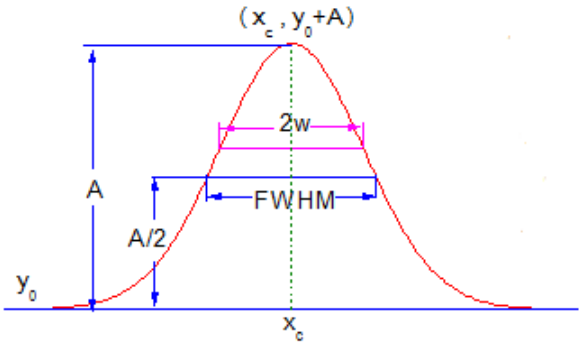

Figure 5.29: Description of the gaussian curve and the equation 5.3.

The beam profile data is fitted with a gaussian equation at each step of quadrupole during a scan. One out of several gaussian fitting in X plane at 83.5 A quadrupole strength, is shown in figure 5.30. Here, oscilloscope data is synchronized in time (msecond) which is converted into wire position (mm) by multiplying by a factor of 2000. The value obtained from the fitting w^2 is the beam σ^2 which is being plotted as a function of quadrupole settings (see figure 5.31). The data points of this plot is then fitted with a parabolic $(AX^2 + BX + C)$ fitting.

The coefficients A, B, and C obtained from parabolic fitting is being compared with the

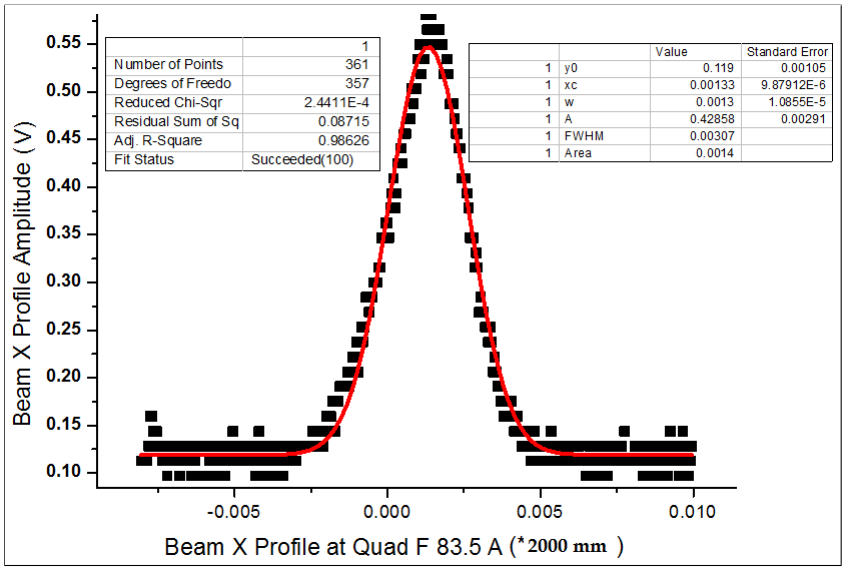

Figure 5.30: Gaussian fitting in X plane at 83.5 A quadrupole strength.

coefficients of the equation 5.4. This is to reconstruct beam matrix Σ in transverse plane.

$$Beam \quad Matrix \quad \Sigma = aK^2 - 2abK + (c + ab^2) \tag{5.4}$$

where K is quadrupole field strength.

These beam emittance in a plane is then calculated from the determinant of the beam matrix $\epsilon_x = \sqrt{det\Sigma^x_{beam}}$. Thus, the transverse beam emittance in X plane is given by the equation 5.5.

$$\epsilon_x = \sqrt{ac}/d^2 \tag{5.5}$$

where d (127.6 cm) is the drift space between scanning wire and quadrupole.

This emittance measurements are performed with three settings of stripper foil azimuthal i.e. -17.2 mm (-0.80º), -19.2 mm (-0.89º) and -21.2 mm (-0.98º). Simultaneously, CBQSW (collimator) at each stripper foil setting is measured in both the transverse planes as shown in figure 5.32.

These measurements (see figure 5.32) are also verifying that CBQSW at collimator during a quadrupole scan is inversely proportional to the beam emittance in that plane. In the high-intensity beamline, a comparison of quadrupole scan at collimator and simulation studies have also indicated the same correlation between CBQSW and transverse beam emittance. The measured RMS emittance is of the same order as the normalized emittance obtained by IBA

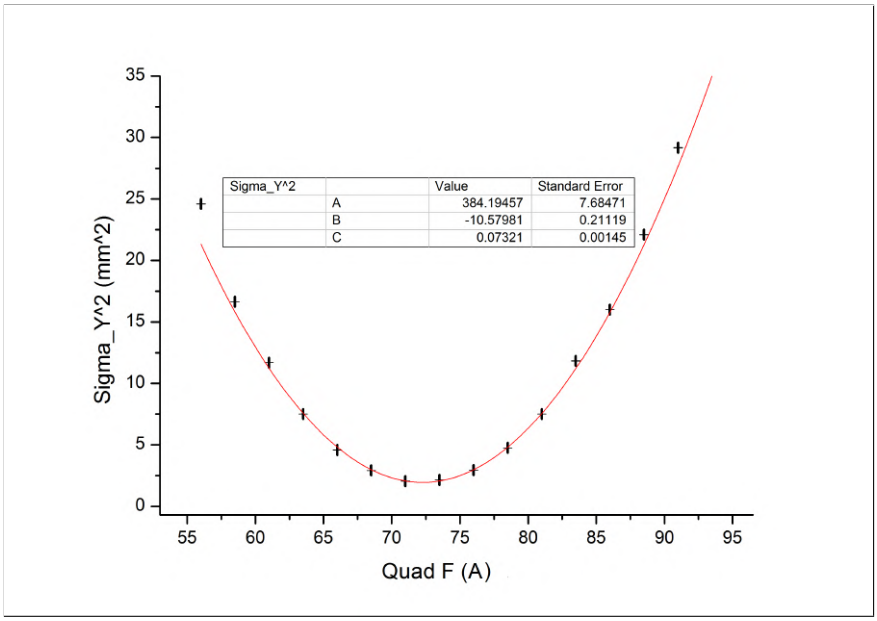

Figure 5.31: Parabolic fitting in Y plane at -17.2 mm (-0.80º) azimuth stripper foil setting.

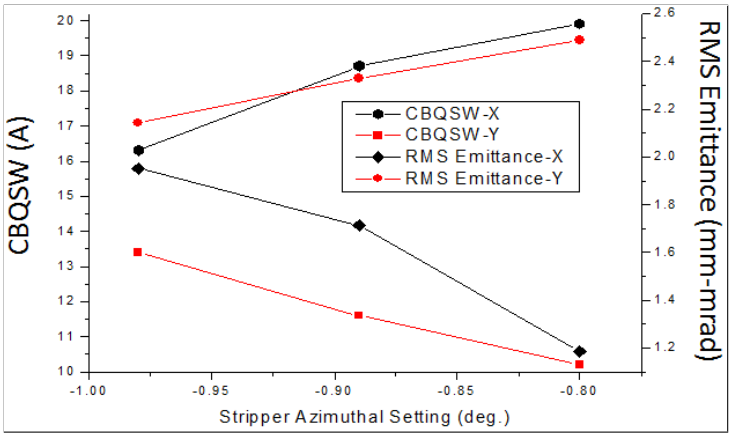

Figure 5.32: Measurement of transverse beam emittance and CBQSW at different azimuth stripper foil settings showing an inverse co-relation. The plots in black are representing horizontal plane while red plots are showing vertical plane.

which is shown in table 5.1. For the emittance measurement, we have also found that there is a change of approximately 40% horizontally and only 14% in vertical plane with varying stripper foil azimuth settings. In this work, IBA has also made an assumption that the stripping process redefines the horizontal phase space parameters and vertical phase space remains unchanged [26].

A minima of quadrupole scan at collimator and parabolic fitting represents focal point at the end collimator and scanning wire, respectively. The distance between scanning wire and collimator's end is 41.8 cm. The focal point at the end of the collimator and at the wire position in X plane is at quadrupole strength equals 96 A and 104 A (see figure 5.33), respectively. This

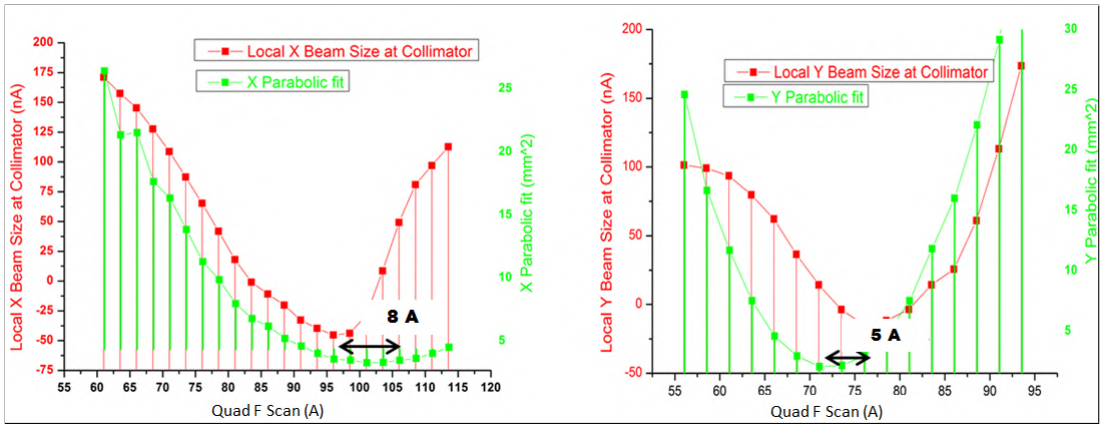

Figure 5.33: Comparison of focal points at the scanning wire and the end of the collimator in X (on the left) and Y (on the right) planes.

difference of 8 A represents the distance between the scanning wire and the end of the collimator that is 41.8 cm. In thin lens approximation, quadrupole strength is inversely proportional to focal length. Despite of this fact, if we assume that the focal point movement is linear and there is no acceleration involved in focal point movement (constant speed). Then, it is possible to calculate the rate of change of focal point position per Ampere change of quadrupole settings (S_f). This technique gives a good idea of focal point movement, during a quadrupole scan.

$$\mathrm{S}_f = \frac{Distance \quad between \quad scanning \quad wire \quad and \quad collimator's \quad end \quad (cm)}{Difference \quad in \quad the \quad minima \quad of \quad collimator \quad and \quad parabolic \quad profile \quad fitting \quad (A)}$$

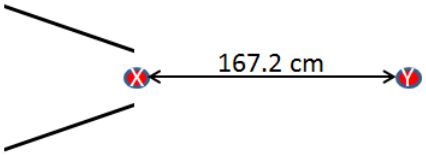

Figure 5.34: Distance between focal points in X and Y plane when the focal point in X is at the end of collimator.

S_{f_x} and S_{f_y} are found to be 5.225 cm/A and 8.36 cm/A, respectively. Now, the focal point in Y and X at the end of the collimator is at 76 A and 96 A, respectively (see figures 5.33). If we multiply the difference of quadrupole settings ($96 - 76 = 20A$) and multiply it with S_{f_y}. This gives us the distance between focal points in X and Y when the focal point in X is at the end of the collimator and is equals to 167.2 cm (see figure 5.34). If we assume ideal conditions and multiply CBQSW with S_f in X and Y plane. We obtain the distance traveled by focal point during CBQSW. This is illustrated in figure 5.35 for three different stripper azimuthal settings (STPA). Within 3 mm change in the stripper azimuth settings, the difference of the transverse focal point behind the collimator is in the order of 10 cm to 14 cm. Also, this is showing that

the focal point can be pushed further behind the collimator by minimizing the transverse beam emittance. The same has observed in simulations which is discussed in section 5.2.1.

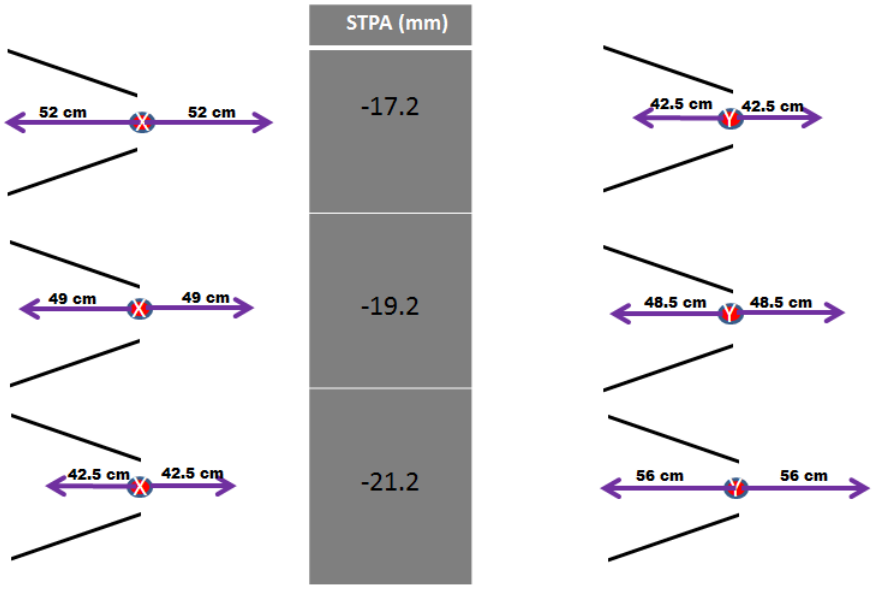

Figure 5.35: Distance travelled within CBQSW range by the focal points in X and Y plane at -17.2 mm (-0.80°), -19.2 mm (-0.89°) and -21.2 mm (-0.98°) azimuthal stripper foil settings.

Fundamentally, these calculated S_{f_x} and S_{f_y} can be applied to the high-intensity beamlines of ARRONAX. In the section 5.3.1, we have discussed the location of focal point w.r.t. collimator's position. Thus, it is possible to approximately estimate focal point location by applying the above calculation.

In the previous section, we have gained the knowledge of the interpretation of the results of quadrupole scans at collimator. The repeatability of results during a quadrupole scan has also been studied on the same day. We have found that the machine settings are robust enough to produce the same results at collimator, when performed on the same day. The repeatability of settings on different days is also investigated. For this, statistical analysis is implemented and is discussed in the next section.

5.3.4 Statistical studies

There are two types of statistical studies performed and discussed in this section.

- The first is to produce some statistical data following the irradiation runs over a span of 1.5 years. In these studies, following the irradiation runs, quadrupole scans are being

compared at the collimator. This quadrupole scan is performed at the beginning and at the end of irradiation runs (total 21 irradiation runs studied). All these quadrupole scans are compared to estimate the variation in CBQSW during irradiation runs.

- The second is to check the robustness of the operational settings of the machine. In these studies, same library settings are used with only modification of the main coil settings to optimize the transmission rate of each day. Three quadrupole scans are performed each day at three fixed stripper foil angles. This has been done, in total four times on each side (Beamline A and P). Each experiment is performed every after 15 days approx.

Quadrupole scans following the production run:

The experiments are performed at the beginning and end of several irradiation runs with optimized machine settings. It is being done to study the beam configuration following the production run. This study can also give idea on the focal point at the beginning and end of the irradiation run. Some studies include quadrupole scan results following the production run. This is to measure the range of variation in CBQSW. This range reflects the change in the transverse emittance.

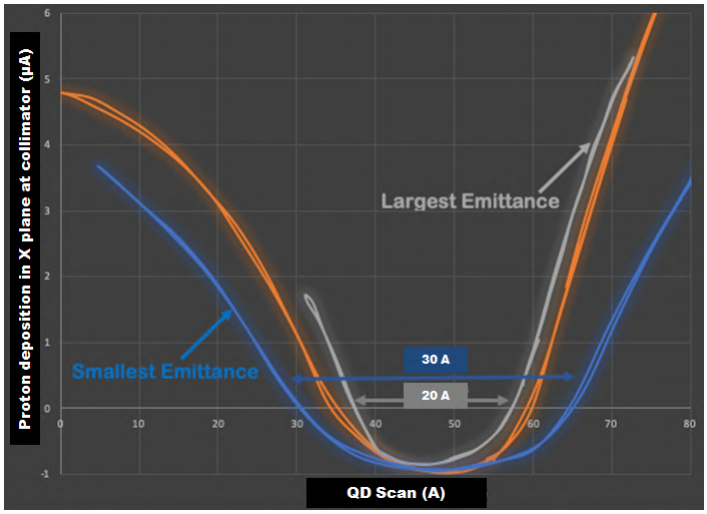

Figure 5.36: CBQSW obtained during a quadrupole scan over a span of 1.5 year.

ARRONAX has several libraries optimized for beam-type or specific isotope production. Accordingly, the operator uploads one of the library settings. All these settings are further optimized to improve the transmission rate. A quadrupole scan is being performed after such optimization and another reading is being taken at the end of that run. It has been done repeatedly over a span of 1.5 year. It is observed that the focal point of a quadrupole scan at the beginning of the run does not match with another scan at the end of the run. Besides, the CBQSW for each scan at the beginning is larger than at the end of the run scan results. At the

beginning of each irradiation run, operators switch to a pristine foil. Thus, this later indicates that the transverse emittance has increased over that period of run. This is due to the degradation of the foil over time. Later, all these quadrupole scans are normalized and compared. It is found that the CBQSW varies from 20 A to 30 A. This means the change in the emittance is in 10 A range at ARRONAX C70 cyclotron. The minimum emittance is at 30 A and the maximum is at 20 A. This is illustrated in figure 5.36. This figure can be correlated with simulation results shown in figure 5.6 where simulations are performed with various beam sigma. This indicates a variation of beam sigma in a beamline in time.

The parameters affecting the emittance in the beamline are stripper foil angle interacting with the beam and integrated beam intensity of the foil. This is already discussed in section 5.3.2. The other parameters affecting the beam emittance in the machine can be found in the ongoing beam dynamics studies of the injection line at ARRONAX.

Machine setting robustness for regular operations:

Machine settings are studied to examine robustness for regular operations. In this method, at first, we have optimized and saved the machine settings such as on from the source, the injection line, the cyclotron, and the beamline. The quadrupole D scan is then being performed at various stripper foil angles w.r.t. to the central position of the cyclotron. This experiment is being repeatedly carried out with the same already saved settings with minor modifications of the main and compensation coil settings, to improve the transmission on each day.

As shown in figure 5.37, a total of four readings have been taken at three randomly chosen foil angles. This experiment is performed on both sides A and P beamline. Each reading is taken with an interval of approximately two weeks. As one can see, the CBQSW is changing with the same operational settings used on both beamline sides. This shows that the emittance on each day is different in an experimented beamline. It is highly possible that the beam emittance is not the same due to the degradation of stripper foil in time. During the experiment, each time they are in different conditions varying the transverse emittance. Another parameter that can affect the beam emittance is injection mismatch (discussed in the chapter 2).As mentioned earlier that the beam injection is done in cyclotron by spiral inflector. With a spiral inflector, it is not possible to inject a beam that has a matched emittance ellipse because the inflector couples the two planes while the planes are not coupled in matched emittance in the cyclotron

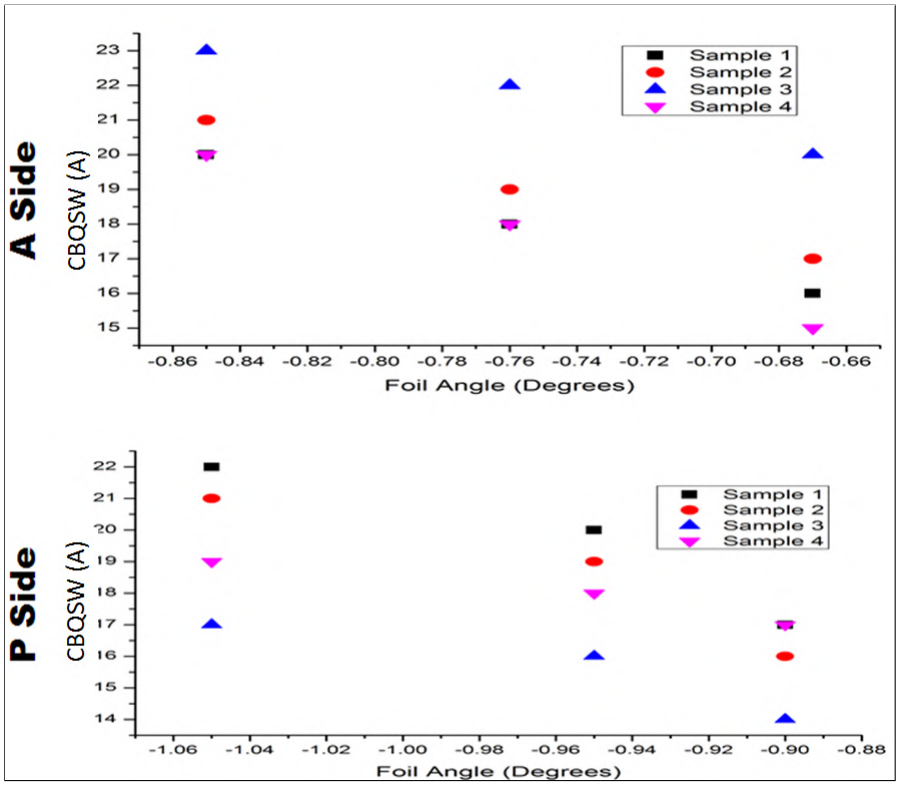

Figure 5.37: CBQSW obtained during the quadrupole scans at different stripper foil angles with same machine settings on different days (A and P Side with total 4 sample size on each side).

itself. It is also clear that there is a need of beam dynamics studies in the injection line. In these experiments, the stripper foil angle and steerer-X couples are used to recenter the beam. Operationally, the focusing element setting has to be changed to accommodate the beam with different twiss parameters. It can be seen on the plots that the settings are not robust enough to produce the same result (beam) at collimator. The variation in the CBQSW observed is 15-20% with the same settings on various days.

When we compare the results from figure 5.37, this can also be extracted that with increasing stripper foil angle (magnitude), CBQSW is also increasing. This means that in all cases, and both the beamline sides (A and P side), the stripper foil angle is behaving (impact on the beam) in the same way. The beam emittance is varying each day resulting in a dissimilar end result. Nevertheless, the stripper foil angle for the best beam dynamics can be fixed. The stripper foil angle should be approximately at -1° and -0.85° on P and A side, respectively for best beam dynamics at C70 cyclotron beamlines.

5.4 Conclusion

Using a quadrupole scan technique, high energy (70 MeV) proton beam characteristics (i.e. transverse focal point, size and, position) of the cyclotron have been studied. With beamline setting modification, the quadrupole scans results at the end-line instrumented four-finger collimator and BLM have delivered various information about global and local beam characteristics.

The global beam characteristics mean the applicability of these characteristics is independent of time. A method has been developed to predict transverse focal point w.r.t. the end-of-line collimator. Due to beam losses at sensitive locations, it is not possible to keep the focal point in front of the collimator in both transverse planes. For safer target irradiation, it is essential to keep the focal point far behind the collimator in the transverse plane. Besides, a CBQSW is obtained at the collimator during a quadrupole scan which is inversely proportional to the transverse beam emittance. This is being verified experimentally and in simulations. It varies between 20 A to 30 A during various irradiation runs such as Sr^{82} production run. It can also be inferred as a change in the transverse beam emittance at ARRONAX cyclotron. The beam quality in a beamline depends on the condition of the stripper foil in use and also, its azimuthal angle. The operational settings are not able to produce the same beam on target partly due to the foil degradation. The best beam quality by transverse size is obtained at -0.85º (-18.5 mm) and -1.0º (-21.5 mm) azimuthal angle of the foil on A and P side, respectively. At those angles, beam divergence is minimal and also the beam orbit is matching the center of the selection magnet.

The local beam characteristics are time-dependent properties during operations. It is observed that the beam quality tends to diminish with the aging of stripper foil. During operations, one can see an increase of beam losses, depending on the condition of the foil, due to an increase in multiple and inelastic scattering. As well, the focal point on the same day is found to be independent of the beam intensity. Therefore, a quadrupole scan on the same day at a low-intensity beam can give a good approximation of the beam at higher intensity.

In the low-intensity beamline, the inverse nature of CBQSW with the transverse emittance has been investigated. Also, we have correlated the quadrupole setting to locate the focal length in the transverse planes, leading the future application of the technique to give the position of the focal point and indication of transverse emittance, with respect to the quadrupole scan.

Similarly, the focal point can be calculated for high-intensity beamline by adding an insertable beam profiler upstream of the collimator. With this knowledge of focal points in the transverse plane, operations will be safer from the target's point of view.

The level of losses need to be low in order to increase operational beam intensity for isotope production. The addition of beam diagnostics such as BLM, helps to minimize these losses. In doing so, the capacity to indicate the position of the beam diminishes. In other words, the BLMs show their limit to be used as diagnostics. In addition, for radioisotope production, focal points have to be away of the target. In this thesis, a technique has been devised not only to measure the focal point but also to infer the longitudinal displacement of the focal point, from an indirect emittance measurement. This technique includes a quadrupole scan which requires the beam to be steered in an adequate position (centered). Besides the BLM, being less significant with low losses, using Beam Position Monitor (BPM) upfront the targets, to steer the beam would help to keep the above technique more accurate and be able to pinpoint the longitudinal location of the focal point more reliably. On the other hand, the BPM provides a tool to operators for beamline tuning by matching a beam centroid with central axis of a vacuum pipe. Moreover, BLM's positioning potential and impact of stripper foil angle on beam positioning at the extraction point, can also be examined experimentally.

Chapter 6

DEVELOPMENT OF BEAM POSITION MONITOR AT ITHEMBA LABS

6.1 General Description

Beam position monitors (BPMs) are the frequently used non-destructive beam diagnostics used at accelerator facilities around the globe. BPMs deliver information about the beam centroid and also act as a monitoring system for the longitudinal bunch shape [73]. As mentioned earlier, the ARRONAX machine is not equipped with any BPM diagnostics. Therefore, ARRONAX showed interest in one of the BPM design proposed by iThemba labs, South Africa. The iThemba labs is the continent's largest facility for particle and nuclear research as well as produce radionuclides for commercial, research and medical applications. This BPM is being proposed for a new C70 cyclotron project at the iThemba labs [72]. One of the reasons behind ARRONAX's interest in that BPM is its compactness. The BPM dimension can fit adequately in the limited space of the beam diagnostics chamber at ARRONAX. So ARRONAX worked in collaboration with them to develop that BPM. Within this collaborative framework, simulations and initial calibration of the BPM at iThemba labs facility is carried out. This study implemented the tools and electronics present at iThemba labs. "BPM proposed" works on the principle of electromagnetic pick-ups [73]. The idea is to measure the flux of electric charge induced by the electric field of the beam particles on an insulated metallic plate. As the electric field of a beam is time-dependent, an alternating current (ac) signal is seen on the plate and the coupling is done using radio frequency (rf) technologies (see figure 6.1).

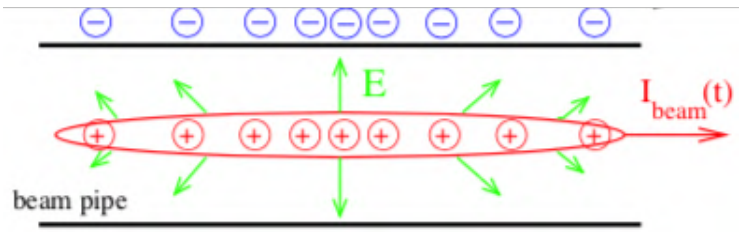

Figure 6.1: The beam current inducing a wall current [73].

An operating environment for electromagnetic research and analysis (Opera3D) [74] software is used in simulations. It is a Finite Element Analysis software suite that allows users to perform simulations of electromagnetic (EM) systems in 2 and 3 dimensions. Previously, it was known as the "Vector field" simulation software. Opera3D is extremely useful for the design of electric motors, magnets, and other electrical machines.

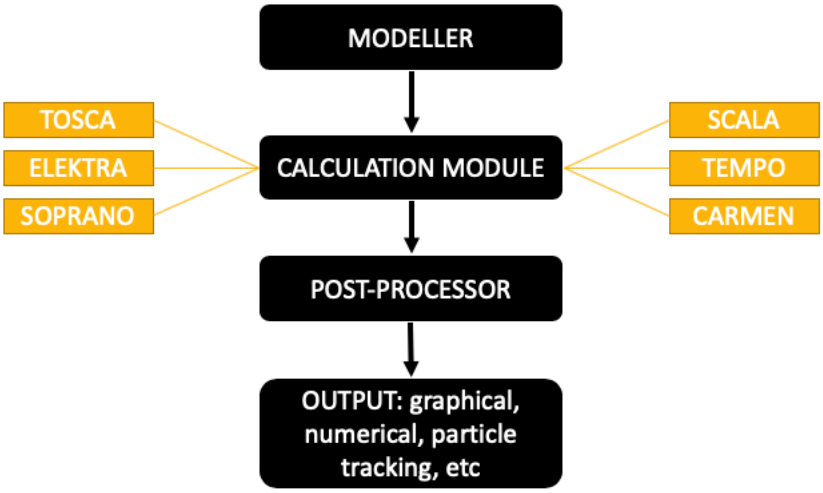

Figure 6.2: The module and structure of the Opera3D software.

As shown in figure 6.2, Opera3D includes dedicated modeler or pre and post-processing environments for problem definition and result analysis. It is possible to upload design directly from a CAD model, to begin with, the analysis. It contains several modules such as TOSCA (Static Field Analysis), ELEKTRA (Time-Varying Analysis), SOPRANO (High-Frequency Analysis), SCALA (Space Charge Analysis), TEMPO (Static and Transient Thermal Analysis) and CARMEN (Rotating Machines Analysis).

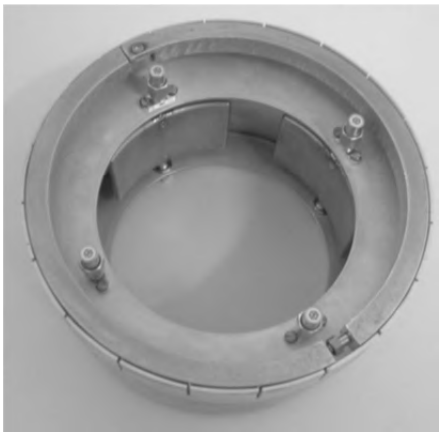

Figure 6.3: The structure of "BPM in operation" at iThemba labs [75, 79].

BPM calibration is being performed with an experimental setup including the BPM and RF

antenna to replicate the beam. Experiments are detailed in the following section and includes the proposed electronics for the BPM operation in the beamline. The "BPM in operation" at iThemba labs is used for preliminary studies to validate the experimental test setup. As shown in figure 6.3, the "BPM in operation" is of circular shape with an internal diameter of 100 mm and an outside diameter of 150 mm [75]. It has four copper electrodes or probes to measure the beam positioning. It has been operational for over a decade at the iThemba Labs. For the "BPM proposed" calibration, experiments with a RF antenna are being performed after verifying the experimental setup with the "BPM in operation". The principle of both BPMs ("BPM in operation" and "BPM proposed") is the same. However, they are totally different in shape, size, and placement of probes. The "BPM in operation" is conceptually a better choice. "IThemba labs" is preparing the installation of a new C70 cyclotron for isotope production. The dimensions of "BPM in operation" does not fit in the design of C70 cyclotron. Therefore, they came up with a new BPM design for their C70 cyclotron. As shown in figure 6.4, the proposed BPM probes are of squared shape with 3.5 mm side length. Two probes are placed on the same side with a 5 mm gap. Both pairs of probes are facing each other in the final installation setup. The distance between both pairs of probes is kept at 100 mm for the following calibration tests, for the reason that 100 mm is the internal diameter of the beam pipes at ARRONAX and iThemba labs.

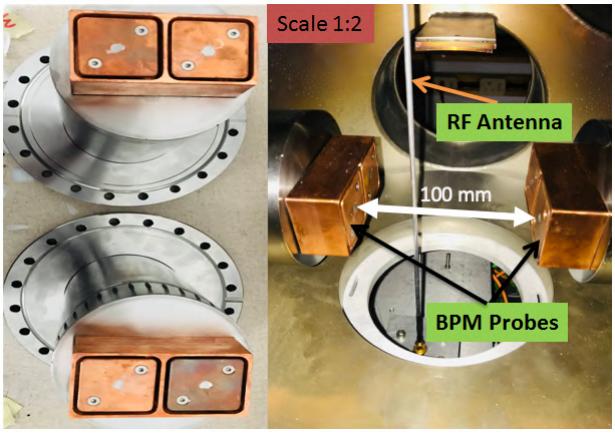

Figure 6.4: The "BPM proposed" design by iThemba labs.

6.2 Experimental Setup

The experimental setup for BPM calibration includes RF antenna. A monopole RF antenna is used here to simulate the beam. As shown in figure 6.5, this represents the circuit diagram of the

experimental setup. A monopole antenna is connected with a Rohde and Schwarz RF generator. The RF range used in the experiment is from 5 MHz to 30 MHz frequency with maximum 10 dBm amplitude. The in-house antenna is made up of copper and aluminum material. It is mounted on an X-Y table. This table can be controlled through an EPICS enabled PV (Process Variable) control system.

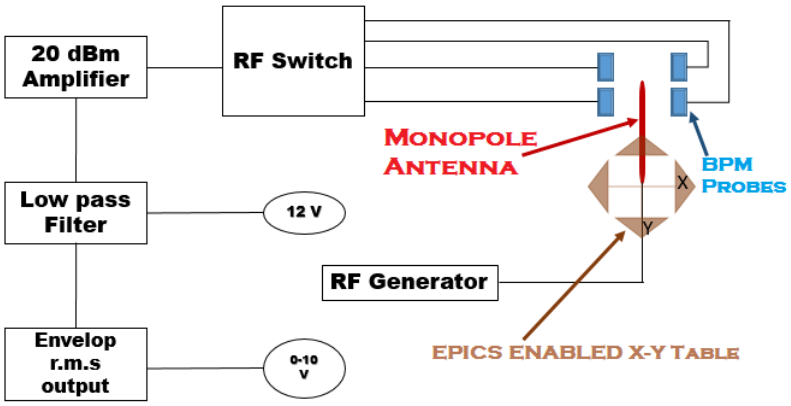

Figure 6.5: Experimental setup (circuit diagram) for BPM calibration.

Each of the BPM electrodes or four probes (see figure 6.5), is connected to the "BECK-HOFF EK1100 RF Switch". RF switches are connected to an in-house made 20 dBm amplifier, low pass filter, and RMS output converter unit with required supply voltages. This whole setup is also EPICS enabled: the input-output of each RF switch and antenna X-Y position can be controlled or recorded using their Process Variable (PV) names. A Python Interface to the Epics Channel Access protocol of the Epics control system called "PyEpics" [76] coding (see the code in appendix D) is being used to control the experiment with visual studio compiler interface. The code has been developed during the present work. "The PyEpics package provides a base epics module to python, with methods for reading from and writing to Epics PVs via the CA protocol" [76]. "React Automation Studio" [77] has been implemented as a graphic user interface (GUI) and is also used to calibrate the antenna at the origin with respect to the BPM mounting. It provides interfaces like CS-Studio (see chapter 3). This application is web-based similar to the just "EPICS archive appliance" at ARRONAX as discussed in chapter 3.

6.3 BPM Calibration

6.3.1 Introduction

The BPM calibration experiments can be done using the beam itself or an instrument simulating the beam. As discussed in the experimental setup, a monopole antenna [78] is used to replicate the beam. A monopole antenna is a "class of radio antenna consisting of a straight rod-shaped conductor, often mounted perpendicularly over some type of conductive surface, called a ground plane" [78]. The monopole antenna's signal field around it is shown in figure 6.6. This concept is used to replicate a beam for calibration tests.

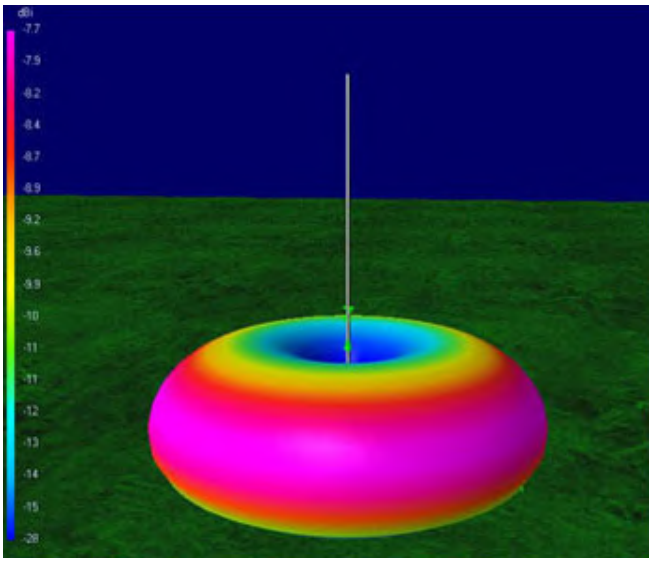

Figure 6.6: "3D Radiation pattern of the 1/4 wavelength monopole antenna over real ground" [80].

Similarly, an antenna is mounted vertically perpendicular on the X-Y table. The length of the antenna is kept above BPM in the experiments to have proper signals on the BPM probes. The X-Y position of the antenna with respect to the BPM is manually calibrated using vernier caliper and standard ruler. The center of the BPM is considered as the origin point which means origin is defined w.r.t. the BPM mounting. Then the antenna position has been saved in X-Y table position PVs from react automation studio GUI. The PyEpics code is prepared for doing measurement on a grid with RF switches cycling at 100 Hz (for code see appendix D). This is done to create a mesh of BPM probes response for the calibration. Once this code is running, the antenna position is scanning the grid in the transverse planes ($\pm$10 mm in X and Y co-ordinates). During the process, RF switches are kept cycling through probes

at 100 Hz, for registering antenna signals on each probe. The signals are being registered on BPM probes at each antenna position which has been recorded using EPICS PVs. Once this process is complete, we get the mapping of all four probes response with respect to the RF antenna position on a grid. The experimental data is being saved at the end of a run by the PyEpics code. These experiments are performed at an RF frequency of 10 MHz, 16 MHz, and 30 MHz with 6-10 dBm amplitude for regression analysis. The normalization factor has been decided according to regression analysis with the lowest possible error in predicting the antenna position with respect to BPM probes. In other words, the coefficients obtained should not vary significantly from the regression analysis of experimental data at various frequencies. The most important point here is the error in predicting the antenna's position in X-Y plane. The error should be minimum while using the same coefficients at different frequencies and amplitude, when the antenna is positioned at the center of the BPM. The RF switches measure the response from the probes in log power (dBm). For better interpretation, it is first converted into watts and later into volts for regression analysis of experimental data (see equation 6.1).

$$P_{(dBm)} = 10 * log_{10}(P_{(W)}/1W) + 30 \quad and \quad V \propto \sqrt{P_{(W)}} \tag{6.1}$$

Where $P_{(dBm)}$ and $P_{(W)}$ are power in dBm and watts respectively.1W is equals to 30 dBm and V is the voltage in volts. Therefore, the BPM final output will be in volts.

6.3.2 Model preparation in OPERA3D

In Opera3D, the beam is defined as a static solid cylindrical volume with charge density. The volume length used is 150 mm with a radius of 5 mm. The charge density used in the simulations here is 100 Coulomb per mm^3. This volume is displaced within $\pm$10 mm in the X-Y plane similar to the experiments for measurement on a grid. The re-normalized curve to predict the position of the antenna is then compared to the experimental results. The CAD model has been uploaded to create the final model with the best finite element meshing of the whole model volume. In the final model itself, the material definition, finite element step size for meshing the volume, and whole model body is being prepared and solved. This creates a file for the post-processor of Opera3D. In the post-processor, flux from the electric charge of a static solid cylindrical volume is calculated over the area of each probe. The flux data is the final data that

is analyzed for simulation studies in OPERA3D.

6.3.3 Validation of experimental setup

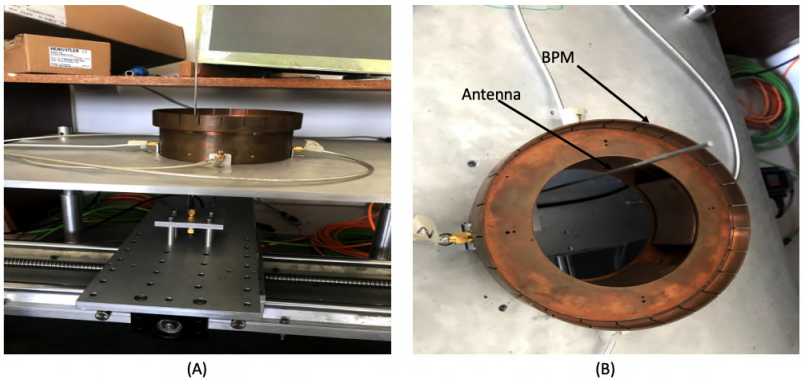

Figure 6.7: The experimental setup for the "BPM in operation". (A) is the side view and (B) is the top view of experimental setup.

As shown in figure 6.7, the "BPM in operation" is mounted on the X-Y table with the RF antenna in the hollow part between the probes. The PyEpics code is developed to perform measurement on the grid in ± 10 mm X-Y plane. A total of 441 data points are recorded by compiling the code. The recorded data is then analyzed and plotted for each probe as a function of the antenna position in X-Y coordinates as shown in figure 6.8. All probes have shown the same behaviour on the grid analysis. The probes are showing higher signals when the antenna is closer and is shown in red color. For probe 1 and 3, the measured power increases as the antenna is moved away in the X direction (from 100 nW to 400 nW at 10 mm to -10 mm, respectively). In the y direction, the power is mildly flat. For the probe 2 and 4, a similar trend is measured but in the y direction and the flatness of the response in the x direction. The results show expected behaviour of probes response. It is also observed that the probe's response is non-linear with the RF antenna position. BPM is to measure the beam's center-of-mass with respect to the center of the beam pipe. For that purpose, regression tests are performed with normalization factors (see equation 6.2) in the X and Y planes.

The beam displacement in a plane can be obtained by normalization to the sum signal of two facing probes. As shown in figure 6.9, the probes are numbered in that pattern: Probe 3 and probe 1 are in the horizontal plane and the other two probes are in the vertical plane. The normalization factor for which the relationship is linear between probes and RF antenna

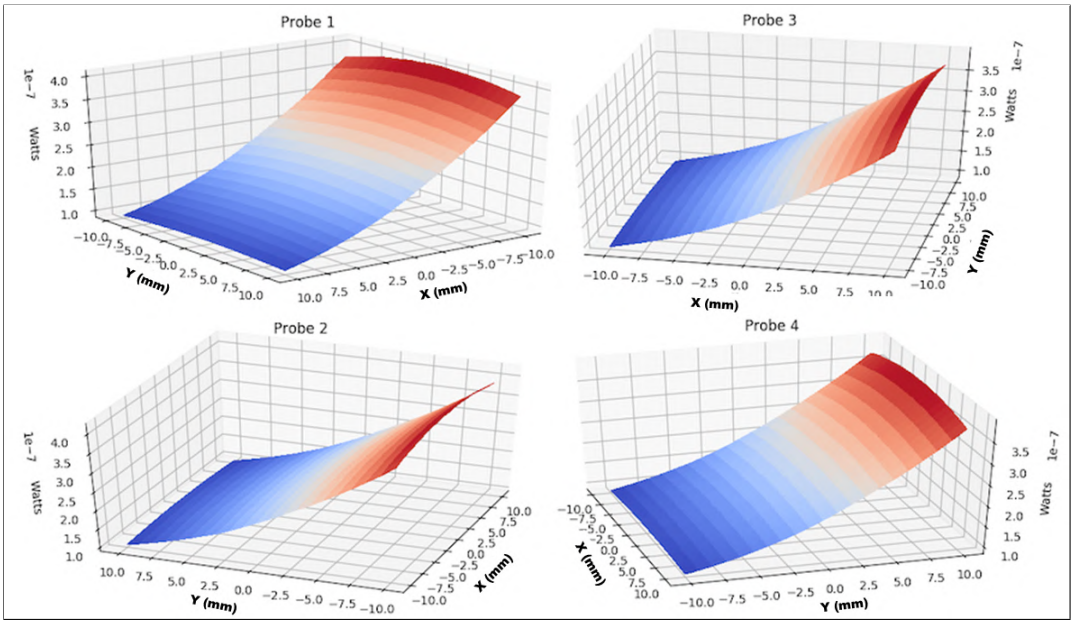

Figure 6.8: The individual probe's response as a function of RF antenna position in X-Y plane at RF generator frequency 10 MHz and amplitude 10 dBm .

position (see figure 6.10) is given below:

$$\text{Horizontal displacement, } X_{disp} = \frac{\text{probe 1 - probe 3}}{\text{probe 1 + probe 3}} \tag{6.2}$$

$$\text{Vertical displacement, } Y_{disp} = \frac{\text{probe 2 - probe 4}}{\text{probe 2 + probe 4}}$$

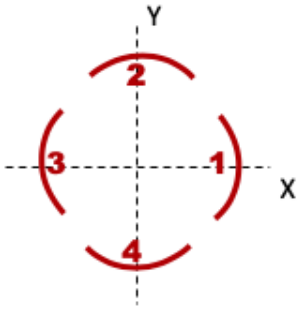

Figure 6.9: "BPM in operation" probes experimental configuration in X-Y plane.

As the linear relation has obtained. It is now possible to fit the data points with the equation of the line. Thus, the data is fitted with the Y=aX+b equation of line where a and b are the coefficients of the equation. Y is the predicted beam displacement in X or Y plane. This

is performed at three different frequencies and the amplitude of the RF antenna mentioned earlier. The value of the coefficients 'a' found is 30.6±4.2 and 'b' is 0.11±0.01 in X-plane and in Y-plane, 'a' is 30.5±3.5 and 'b' is 0.32±0.01. The coefficients do not vary significantly at different antenna settings (input RF frequency and amplitude). These coefficients show that the slope is varying according to frequency but the offset is quite stable. Therefore, better accuracy can be achieved at the origin of antenna position using these coefficients regardless of the frequency.

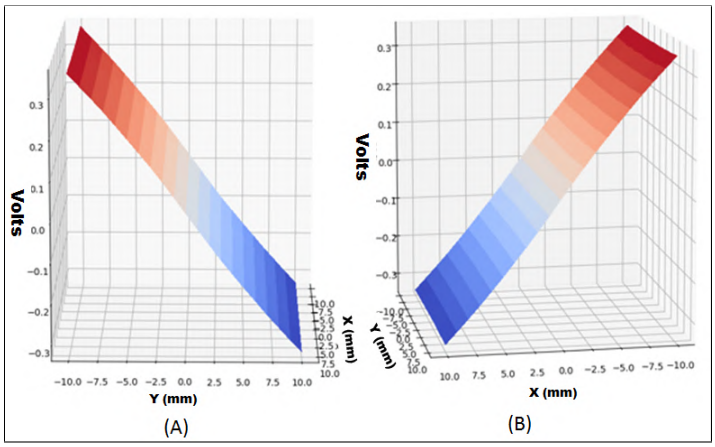

Figure 6.10: The normalized plots to predict the position of antenna in X plane (A) and Y plane (B) which are coming from the equation 6.2.

The errors are then calculated by subtracting actual antenna position and predicted position. It has been seen that the errors are not significantly changing at different RF antenna settings. Moreover, the high accuracy is being found in predicting the antenna position at the origin (when the antenna is positioned at the center). It is a good indication that the same coefficients can be used to predict the position of the antenna. It is also indicating that these coefficients are independent of beam current. For measurements in ±10 mm, the overall errors in prediction of antenna position (see figure 6.11) is ±0.4 mm in X and Y plane. However, the error at the origin is rather smaller which is ±0.15 mm in X and Y.

Later, the method of normalization has been studied for the old system iThemba was using over a decade for "BPM in operation". It is found that the normalization factor in the old system is different from what we are using in the calibration of "BPM in operation". The equation of line Y=aX has been implemented in the old system with the normalization factor given below:

$$\text{Horizontal displacement, } X_{disp} = \frac{\text{probe 1 - probe 3}}{\text{probe 1 + probe 2 + probe 3 + probe 4}} \tag{6.3}$$

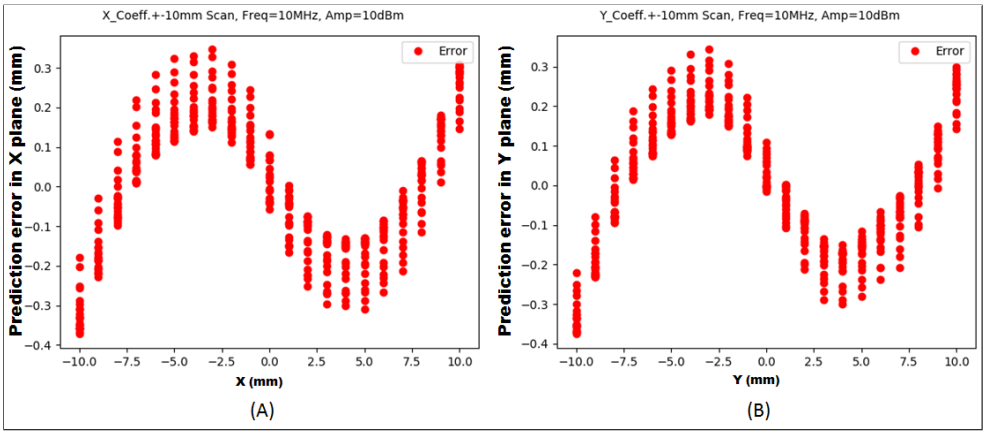

Figure 6.11: The prediction error in the antenna position in X plane (A) and Y plane (B).

$$\text{Vertical displacement, } Y_{disp} = \frac{\text{probe 2 - probe 4}}{\text{probe 1 + probe 2 + probe 3 + probe 4}}$$

The value of 'a' implemented was 56.6. Therefore, the data has been re-analyzed using the same normalization factor (see equation 6.3). The coefficient with the experimental setup found is 55.8±4.8 which is very close to the implemented coefficient at iThemba for decades. The calculated error found is ±0.8 mm which is larger than the case of the new normalized factor's obtained error. It is not only validating experimental setup rather also indicating that the new normalization factor can give better accuracy of beam position prediction out of the "BPM in operation".

For further investigation, Opera3D simulations is used. As shown in figure 6.12, first of all, the model body is prepared. BPM is mounted on a table in the simulation model similar to the experimental setup. The model body is then analyzed for flux calculations on the area of each probe. It is done in the post-processor of Opera3D. Responses from the simulated probes is found to be in good agreement with the experimental results: each probe response is non-linear as indicated earlier (Experiment with RF antenna) and with the normalization, linearity is observed similar to experiments. This also indicates that experimental setup is optimized to calibrate a BPM of such kind.

The RF generator provides input to an antenna. This input is the frequency (MHz) and amplitude (dBm) signals. It is found that the RF generator's amplitude and charge on the volume simulating beam are closely related. When one changes the charge of the volume then

the recorded flux on a probe changes proportionally in the simulations. Similarly in the experiments, any change in the amplitude of RF antenna signals reflects proportionally at the probe's response. This is due to a fact that fields are additive. The RF antenna signals is based on the frequency and amplitude provided by RF generator. This implies that the RF generator's amplitude is simulating the beam current and frequency is equivalent to the revolution frequency of a cyclotron.

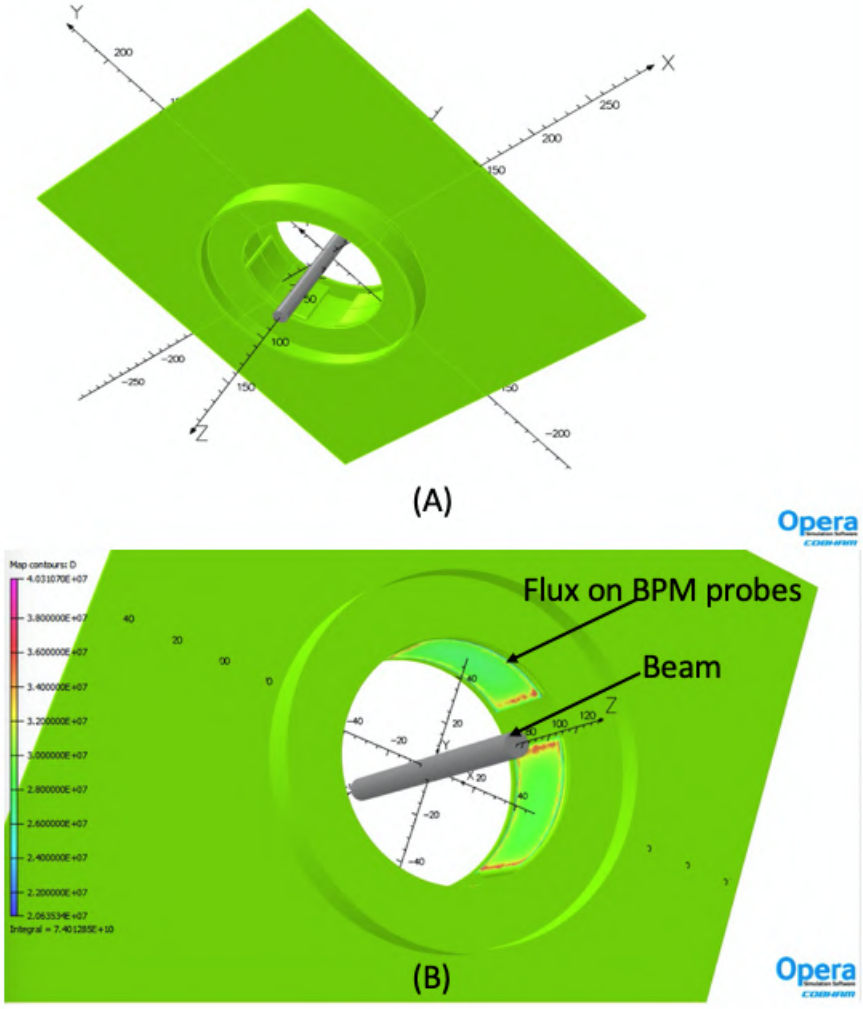

Figure 6.12: (A) Opera3D model of "BPM in operation". (B) Model analysis in post-processor.

6.3.4 Error discussion

During the experimental work, some of the sources of errors are being noticed and are addressed below:

- Antenna position in the X-Y plane with respect to the BPM has been done by using either a vernier caliper or with a 30 cm ruler. In such procedures, there is a very high chance

of committing human error due to a lack of specialized devices for calibration of antenna position. Therefore, the error in finding the origin of the antenna position is in the order of less than 1 mm.

- The aluminum and copper antenna is in-house made. It is like a thick wire and mounted on the X-Y table vertically. It should be perpendicular to the X-Y table and straight. It can cause an error in X-Y table coordinates and actual coordinates due to minor bend or non-uniformity. Ultimately that error will reflect in regression tests causing larger error in the prediction of the antenna position in the X-Y plane. We have corrected that issue by using a wire straightening machine roller, prior to the experiments.
- The coefficients used for the calibration are expected to be fixed and suitable for the entire range of frequency (5 to 30 MHz) of the RF antenna signal, studied above. A significant deviation of these coefficients to be used, has been observed according to the frequency, when one BPM probe was connected to one of the initial dedicated wires. The wire appeared to be shorter, by approximately 10 cm in length, than the other wires. Therefore, for the final experiments, several new wires were fabricated with strictly the same length and, additionally tested with a network analyzer to check each wire's capacitance and resistance. The wires with the same properties were then used. The assurance of exact same length and properties of the wires connecting BPM probes to the RF switch channels, resolved the deviations of the coefficients to be used.

6.4 Calibration of "BPM Proposed"

The experimental setup is almost the same for the calibration of the "BPM proposed". However, it needs a supporting structure for experimenting due to its mechanical design. Therefore, it is installed on a structure as shown in figure 6.13. The structure used is a replica of the diagnostic chamber in one of the beamlines at iThemba labs. This structure is then mounted on the EPICS enabled X-Y table. The flanges are used to weld both "BPM proposed" parts holding a pair of probes (see figure 6.4). The separation length between the two facing probes is 100 mm as shown in figure 6.4.

Initial studies have revealed that the probe's response is reduced usually by a factor four (amplitude) compared to "BPM in operation" probes. However, the mechanical dimensions and shapes of probes of both BPMs are different. As shown in figure 6.14, the result of measurement on a grid with the RF antenna, the calibration procedure is same as used for the "BPM in operation". The range of the measured power is much less than the measurements with the previous BPM (here 30 to 160 nW) i.e. indicating that the resolution power is going to be lower for the proposed BPM. But the slope trends are similar. A non-linear response of each probe in ± 10 mm X-Y plane with RF antenna at different frequencies and amplitudes is observed.

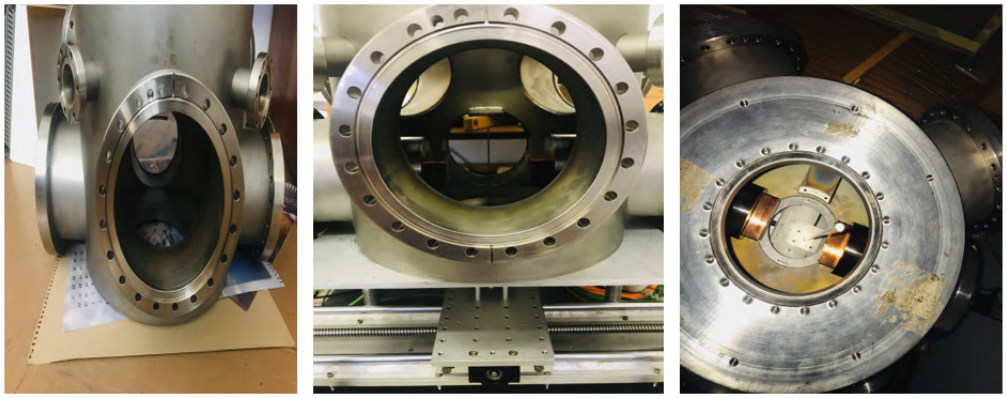

Figure 6.13: The experimental setup for the proposed BLM. (A) The structure to install BPM. (B) Side view with the installed BPM. (C) Top view with the installed BPM.

The mechanical shape of this BPM does not have any probe in the Y-plane. Therefore, the normalization factor is being used to recreate vertical probes (see figure 6.15) as well as to predict the antenna position in X and Y planes (see equation 6.4). The experimental configuration of the BPM probes is shown in figure 6.15 with probe 1 and 2 on the right side of the beam. The response of two adjacent probes is being added together to recreate virtual probes in all directions. A similar method has been used to calculate the normalization factor for regression analysis. The normalization factor is given in the equation 6.4.

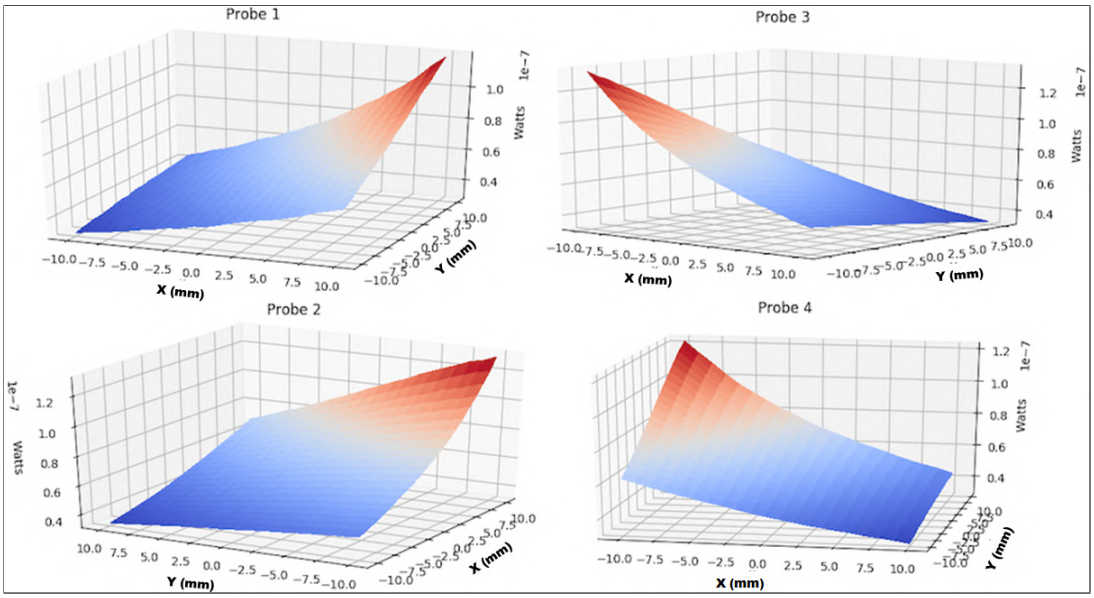

Figure 6.14: The probe's response as a function of RF antenna position in X-Y plane at RF generator frequency 10 MHz and amplitude 10 dBm.

$$\text{Horizontal displacement, } X_{disp} = \frac{\text{(probe 1 + probe 2) - (probe 3 + probe 4)}}{\text{probe 1 + probe 2 + probe 3 + probe 4}} \tag{6.4}$$

$$\text{Vertical displacement, } Y_{disp} = \frac{\text{(probe 1 + probe 4) - (probe 2 + probe 3)}}{\text{probe 1 + probe 2 + probe 3 + probe 4}}$$

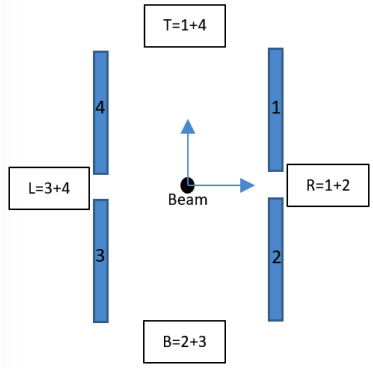

Figure 6.15: Proposed BPM probes experimental configuration in X-Y plane and the beam (RF antenna) is out of the paper.

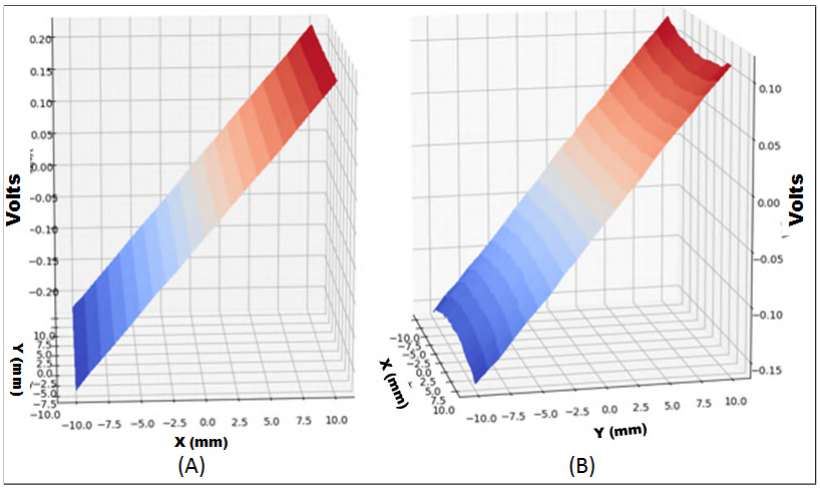

Figure 6.16: The normalized plots to predict the position of antenna in X (A) and Y (B) plane which are coming from the equation 6.4.

As shown in the figure 6.16, one can see that the normalized result is linear in X-Y plane. However, a non-linearity has observed in Y-plane but it is linear in $\pm$5 mm range. Therefore, it is possible to fit the data points with the equation of line. Thus, the data is fitted with the Y=aX+b equation of line where a and b are the coefficients of the equation. 'Y' is the predicted beam displacement in X or Y plane. This has been done similarly at three different frequencies

and the amplitude of the RF antenna mentioned earlier. The value of the coefficients 'a' found is 49.4±5.2 and 'b' is 0.12±0.01 in X-plane and in Y-plane, 'a' is 85.1±5.6 and 'b' is -0.26±0.01.

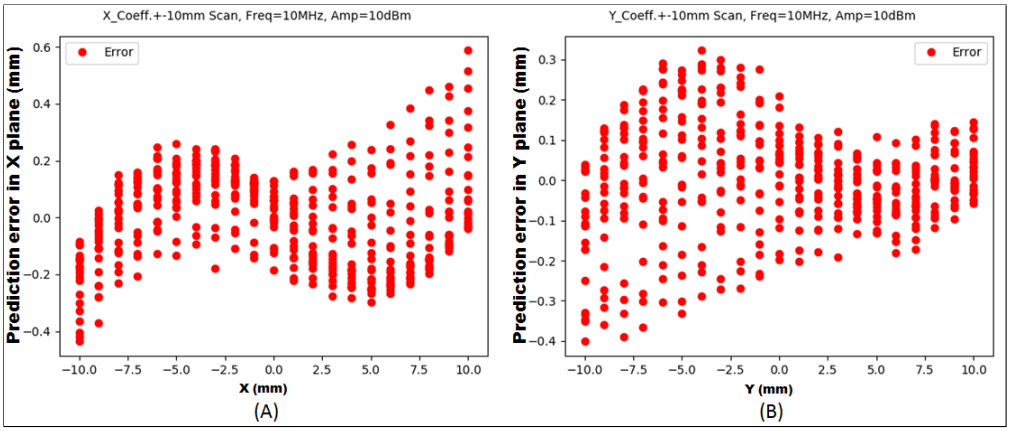

Figure 6.17: The prediction error in the antenna position in X plane (A) and Y plane (B).

The coefficients are not varying significantly at different RF antenna settings. When the errors are calculated by subtracting the actual antenna position and the predicted one, it has been seen that the errors are not significantly changing at different RF antenna settings. For measurements at a ±10 mm position, the errors in predicting the antenna position is ±0.4 mm in X and Y plane (see figure 6.17). The error at the origin is rather small i.e. ±0.2 mm in X and Y plane. High accuracy is being found in predicting the antenna position at the origin (when the antenna is positioned at the center). It is a good indication that the same coefficients can be used to predict the position of the antenna. It is also indicating that these coefficients are independent of the beam current.

All the experiments with the RF antenna indicated that the proposed BPM can be used in beamlines. For further investigation, the proposed BPM is modeled and simulated in Opera3D. Similar to the simulations of "BPM in operation", a volume of same dimension and charge is used to simulate the beam in the model (see figure 6.18(A)). The proposed BPM is modeled in opera3D with a diagnostic chamber identical to the one used in the experiments (see figure 6.18(B)). The model body prepared in the modeler is then analyzed in the post-processor. Similarly, the flux has been calculated in the area of each probe. Responses from the probes are found to be in good agreement with the experimental results. Each probe response is non-linear (see figure 6.19) and, with the normalization, a linearity (see figure 6.20) has observed similar to experiments.

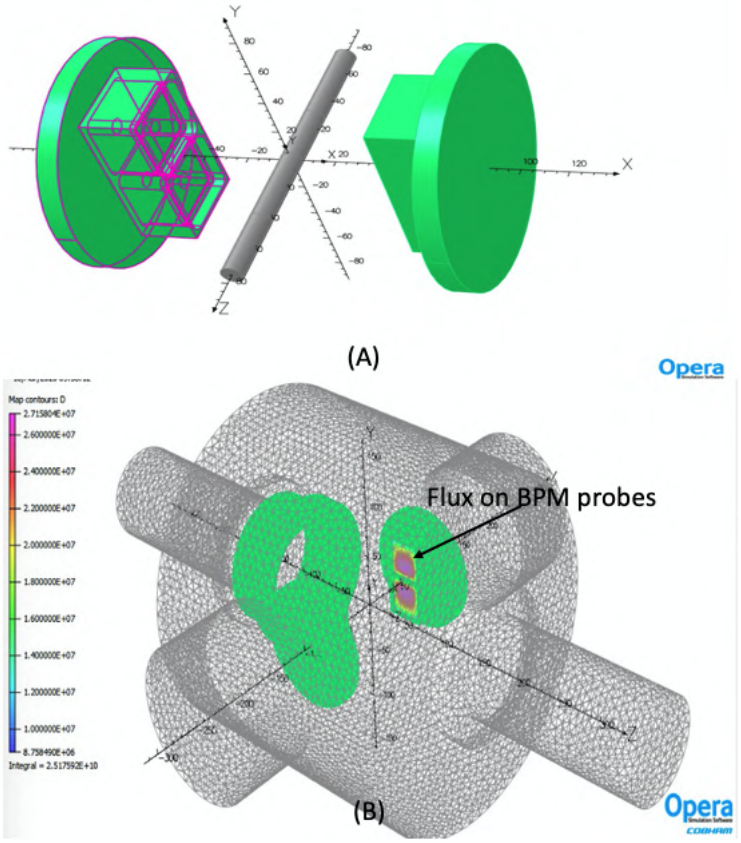

Figure 6.18: (A) Opera3D model of the proposed BPM. (B) Model analysis in post-processor. (All scales are in mm)

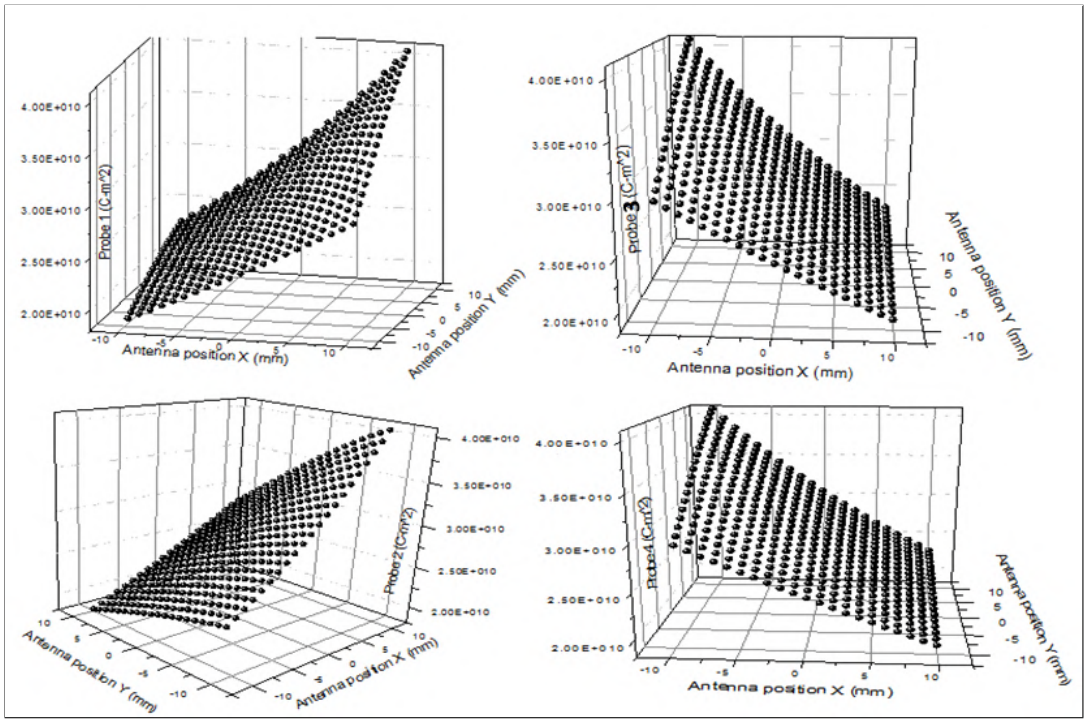

Figure 6.19: The probe's response (electric flux) as a function of charged volume position in X-Y plane in Opera3D.

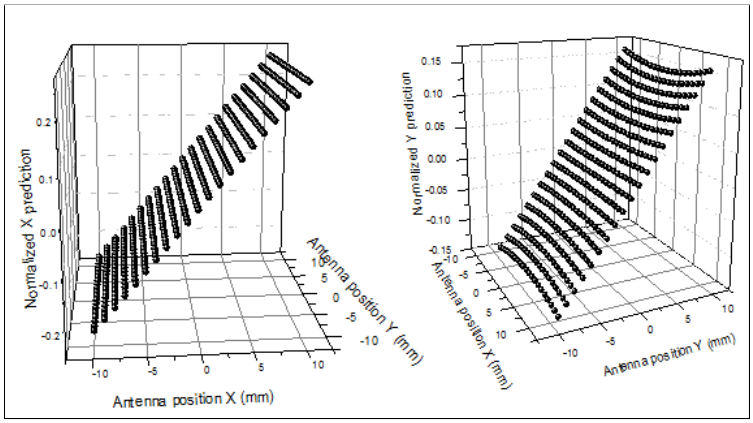

Figure 6.20: The normalized plots of probes response in X plane (left side) and Y plane (right side).

6.4.1 Discussion

In the experimental configuration, the separation length between two facing probes is 100 mm. All the above results are at 100 mm separation length. This separation length corresponds to the internal diameter at both the facilities. If we change the separation length then the flux response on probes should change. In Opera3D, the probe's response at different separation lengths has been studied. The RF antenna is kept at the origin for this study. The results of the probe's response with the same charged volume at three different separation length i.e. 100 mm, 110 mm, 120 mm, and 130 mm have been compared. It has been found that the "BPM proposed" response is getting lost by 25% of the total flux recorded on each probe with an increase of separation length by 30 mm. Therefore, the separation length can not be varied much.

The outcome of the BPM results are satisfactory and indicates that the proposed BPM can be used as online beam position measurement devices at both the facilities. As for BPM design, it does not have any protection system or cooling system. In case of any major mis-steering, the beam can interact with the BPM probes. If the beam intensity is too high, the beam can even melt the probes. Therefore, a cooling or radiation damage protection system has to be installed to protect the probes and its mounting assembly (BPM structure) in the future.

6.5 Conclusion

Preliminary studies, i.e. experimental investigation with a RF antenna and simulations with Opera3D of the new BPM prototype "BPM proposed" indicate its potential of determining the

position of the beam close to the center of the beam pipe. The error in predicting the RF antenna position, replicating a beam within ± 5 mm is around ± 0.2 mm. The results showed improved accuracy when the antenna is closer to the center of the pipe. Moreover, the BPM dimension is adequate to fit in the diagnostics chamber at the ARRONAX beamlines. As it is not possible to increase the separation length between facing probes due to electric flux loss at BPM probes, a probe protection system would to be developed in future. In other words, the BPM needs a cooling system because mis-steered high-intensity beam (150 μA) can damage its probe. One of the solutions could be the use of graphite lining on BPM probes. Another solution could be the use of cooled collimator as a probe protection system if mechanically possible.

Chapter 7

CONCLUSION

In this thesis, a detailed discussion on the 70 MeV proton transverse beam dynamics studies in a beamline and the development of beam diagnostics such as dedicated Beam Loss Monitor (BLM) and Beam Position Monitor (BPM) is presented. The main experimental explorations have been performed at high beam intensities (μA) and, when necessary for dedicated investigations or preliminary tests, at low (pA-nA) intensities. For the collection of experimental data, an EPICS data acquisition system is used where data is synchronized in time with the cyclotron's control system data. At the same time, various operator interfaces are developed in CS Studio (EPICS data monitoring user interface) for either online monitoring of these experiments presented in this thesis or to benefit the operators for the ease of BLM data monitoring. These interfaces played an important role in doing the experiments with sufficient information and also to quickly find the optimized setting prior to the start of an experiment.

Initially, the work has been done towards machine protection. For this purpose, BLMs testing work has been carried out which has lead to their installation on high-intensity lines. Prior to their installtion, four BLMs have been irradiated with a low-intensity proton beam for geometrical response and comparative studies. After satisfactory results, the BLMs have been installed in high-intensity lines and regularly monitored to check their operationality. Consecutively, a threshold of the intensity reading, as an indicator of the beam losses, was set to 50 nA (at 650 V supply voltage). This threshold helps to reduce potential and undesirable events such as damages of sensitive locations during irradiation runs. The BLMs, with 4 individual plates, have the potential of indicating beam positioning. This has been studied with a devised simulation and revealed the prospect of beam position measurements using the BLM placed upstream of the second pair of quadrupole in the high intensity lines. These BLMs are now being continuously used during irradiation runs for Sr^{82} isotopes productions and they have been in operation without any major issues for more than two years. In addition to being adapted to the beamlines of Arronax, the BLM is a durable solution. The potential to indicate beam position makes it a unique tool at ARRONAX in support of high intensity operations.

Transverse beam dynamics experiments have been carried out with the BLM and an instrumented four-finger collimator placed upstream of the target. For transverse beam dynamics studies, the beamline settings (stripper angle, dipole, and steerer) have been modified followed by a quadrupole current variation technique (quadrupole scan). This has been done to examine the impact on the beam at the end-line collimator. The main goal of these studies is to check beam dependencies such as beam alignment, losses, and transverse beam size according to various settings.

The estimation of the focal point plays a very important role because the focal points upstream of the target define the shape of the beam on the target. This knowledge of focal point, would ensure safer target irradiations. In this regard, a method has been developed to predict the focal point location with respect to the collimator position by a single quadrupole scan. This method is based on the focalizing-defocalizing effect of quadrupole in a transverse plane. For high intensity operations, it indicated the focal points, close to the target, are positioned behind the collimator leading to higher potential target damages. The method has also pointed out to the limitation of moving both focal points upstream the target. Thus, to minimize the damage on the target and to push further downstream the focal points, transverse emittance has to be minimized.

A quadrupole scan results at collimator lead to the definition of the Collimator Based Quad Scan Width (CBQSW). An inverse correlation has been established between CBQSW and the transverse beam emittance. The range of CBQSW (20 A to 30 A) has been found during irradiation runs over a span of 1.5 year and can be directly related to the beam quality at different times of irradiation. In addition, it has been found experimentally that the azimuthal angle of the stripper foil, used to perform the extraction, has a dominant impact on the beam's alignment, losses, and transverse size. These observed results are correlated with 'stripper displacement mechanism'. The single wire transverse beam emittance measurements have delivered more precise experimental confirmation of this effect at low intensity.

The statistical studies have been performed over several irradiation runs and pinpoints the variation of the results for regular operation with the same machine settings. This has also indicated a need of stripper foil current integration (μAh) studies in future work because it has a dominating effect on the beam divergence in a beamline. This can advocate to put a threshold (in terms of μAh) on stripper foil usage.

For further improvement of transverse beam dynamics and to steer the beam in a beamline, a BPM is envisaged. For this, BPM prototype calibration tests have also been performed in collaboration with iThemba labs facility in South Africa. For these tests, an experimental setup with a RF antenna, replicating a beam, has been implemented. The simulation tool Opera3D has been used to verify the experimental setup. These tests indicated that the BPM can be utilized for calibration of the beam centroid with the precision of $\pm$ 0.2 mm. BPM dimensions are adequate for commissioning in the diagnostics chambers of the ARRONAX beamline. This BPM is foreseen to be tested with the beam at the ARRONAX facility prior to their installations for operational use.

There are several findings discussed in this thesis which can lead to future work. We have discussed the operationality of BLMs installed in high-intensity beamlines. The BLM, placed near the target, is in a high radiation background region (12000 mSv/h). So there is a possibility that the response also includes background radiation measurements during irradiation runs. This can be tested by putting some shielding around it to prevent the chances of getting background radiation detection. Also, the transverse beam dynamics statistical studies have indicated a variation in the resulting beam with respect to a fixed machine setting on different days. We have discussed stripper foil degradation which is one of the reasons behind it. It is also indicating towards a need of beam dynamics studies in the injection line.

The work (quadrupole scan technique, devised BLM, single wire emittance measurement and developed CS Studio interfaces) presented in this thesis can be adapted to such accelerators used for isotopes production, as we have used very basic instrumentation to study transverse beam dynamics. The G4beamline is capable of simulating such magnetic elements (dipole and quadrupole magnet) and transverse beam dynamics studies with such beamline lattice. The development of new beam diagnostics (BLM and BPM) will give operators an extra tool for beamline tuning. These studies are giving information of downstream events and their impact on the beam before reaching the target. In addition, one can compare the beam quality on different days by comparing quadrupole scan results at collimator. These studies are steps forward towards higher beam intensities usage.

Appendix A

STOPPING POWER OF PROTONS IN AIR

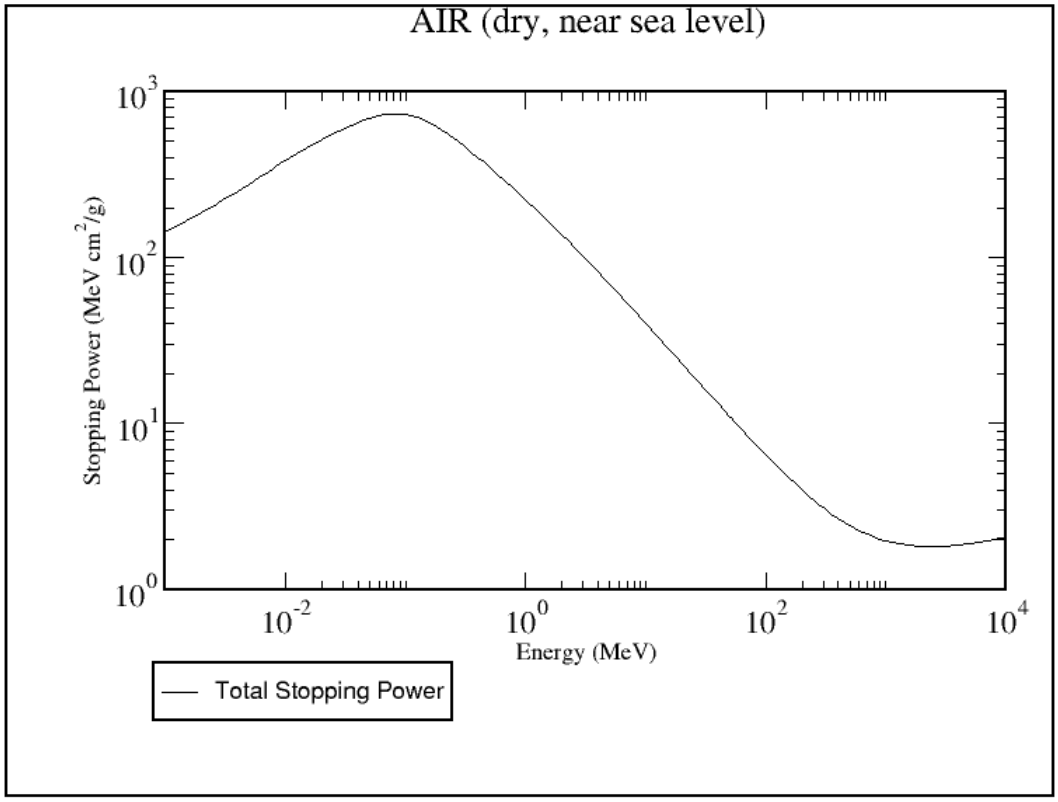

[97]

Appendix B

G4BEAMLINE SIMULATION CODE

B.1 Beamline simulation code

```
*   Beamline dimensioning and positioning.
*   a 70.3 MeV proton Gaussian beam

# QGSP is the "default" physics use-case for High Energy Physics
# but QGSP_BERT is better for low-energy simulations

physics QGSP_BERT

# Material Definition
material Inox Cr,0.19 Ni,0.11 Fe,0.7 density=8.03
material AIR C,0.000124 N,0.755268 O,0.231781 Ar,0.012827 state=g \
    density=0.00120479
material AIRtube C,0.000124 N,0.755268 O,0.231781 Ar,0.012827 state=g \
    density=0.00120479*1.6e-6
material tube Mg,0.0090 Si,0.0100 Mn,0.0070 Fe,0.0025 Al,0.9715 density=2.70


param worldMaterial=Vacuum

trackcuts keep=proton

# define the beam energy is 70.3 MeV kinetic energy, the mass of a proton is 938.272MeV/c
param M=938.272 KE=70.3
param P=sqrt(($M+$KE)*($M+$KE)-$M*$M)

# the beam is nominally headed in the +Z direction
beam gaussian nEvents=10000 particle=proton beamZ=-900 beamX=0 beamY=0 \
             sigmaX=1.911 sigmaY=1.762 sigmaZ=1 meanMomentum=$P sigmaP=0.26 sigmaT=0.0 meanT=0.0 \
             sigmaXp=0.00001 sigmaYp=0.0001 meanXp=0.001

# a reference particle
reference particle=proton referenceMomentum=$P


# BeamVis just shows where the beam comes from
box BeamVis width=100.0 height=100.0 length=0.500 \
            material=Vacuum color=1,0,0

place BeamVis z=-900

virtualdetector det radius=50 length=1 color=0,0,1 format=rootExtended kill=0 referenceParticle=1
virtualdetector detbig innerRadius=56 radius=120 length=1 color=0,0,1 format=rootExtended kill=0 referenceParticle=1

tubs pipebeforeswi innerRadius=50 outerRadius=55 length=305 material=tube color=0,0.6,0.6 kill=0

place pipebeforeswi z=-735
#switching magnet
param swicurrent=86

idealsectorbend switching angle=-40 By=0.0048*$swicurrent+0.9414 fieldCenterRadius=906.67\
                          fieldInnerRadius=856.67 fieldMaterial=AIRtube\
                         fieldOuterRadius=956.67 fieldHeight=110 ironInnerRadius=851.67\
                          ironOuterRadius=961.67 ironHeight=120 ironColor=1,1,0 ironMaterial=Fe kill=1
place switching z=-582.79 x=0 y=0
cornerarc angle=-40 z=-582.79 centerRadius=906.67

#  parameter of steer
param inputcurrent_steerX=-0.9
param inputcurrent_steerY=0.07


#  definition of steer

genericbend SteeringX fieldWidth=239.9 fieldHeight=239.9 fieldLength=490 \
    ironHeight=240 ironLength=300 ironWidth=240 By=0.0115*abs($inputcurrent_steerX)+0.0004 \
    ironColor=1,1,0 fringeFactor=0.2 kill=1 fieldColor=0.6,0.6,0

genericbend SteeringY fieldWidth=239.9 fieldHeight=239.9 fieldLength=490 \
    ironHeight=240 ironLength=300 ironWidth=240 By=-(0.0115*abs($inputcurrent_steerY)+0.0004)\
    ironColor=1,1,0 fringeFactor=0.2 kill=1 fieldColor=0.6,0.6,0

place SteeringX z=150 rotation=Z0
place SteeringY z=150 rotation=Z90

#  parameter of quadripole
param inputcurrent_QA=-0
param inputcurrent_QB=0
param inputcurrent_QC=-40
param inputcurrent_QD=0
```

```
genericquad Quad1 fieldLength=256 apertureRadius=55 ironRadius=70 \
    ironLength=205 coilRadius=18 coilHalfwidth=2 fringeFactor=0.1 \
        ironColor=1.0,1.0,1.0 gradient=0.0761*abs($inputcurrent_QA)+0.1981 kill=1

genericquad Quad2 fieldLength=256 apertureRadius=55 ironRadius=70 \
    ironLength=205 coilRadius=18 coilHalfwidth=2 fringeFactor=0.1 \
        ironColor=1.0,1.0,1.0 gradient=-(0.0761*$inputcurrent_QB+0.1981) kill=1

genericquad Quad3 fieldLength=256 apertureRadius=55 ironRadius=70 \
    ironLength=205 coilRadius=18 coilHalfwidth=2 fringeFactor=0.1 \
        ironColor=1.0,1.0,1.0 gradient=0.0761*abs($inputcurrent_QC)+0.1981 kill=1

genericquad Quad4 fieldLength=256 apertureRadius=55 ironRadius=70 \
    ironLength=205 coilRadius=18 coilHalfwidth=2 fringeFactor=0.1 \
        ironColor=1.0,1.0,1.0 gradient=-(0.0761*$inputcurrent_QD+0.1981) kill=1

place Quad1 z=537.5
place Quad2 z=841
place Quad3 z=6806.71
place Quad4 z=7212.71

#param histoFile=Std_Blmwall_QA($inputcurrent_QA)_QB($inputcurrent_QB)
param histofile=Std_ColX_QC_($inputcurrent_QC)QD_($inputcurrent_QD)

polycone wall innerRadius=51.5,51.5 outerRadius=1000,1000 z=0,3700 material=CONCRETE \
     kill=1 color=0,1,0

place wall z=2815.21

tubs pipebeforeQC innerRadius=50 outerRadius=55 length=300 material=tube color=0,0.6,0.6 kill=0
tubs pipeafterQD innerRadius=50 outerRadius=55 length=2000 material=tube color=0,0.6,0.6 kill=0
place pipebeforeQC z=6420
place pipeafterQD z=8515

# construct collimator
polycone Collimator_Left innerRadius=45,12 outerRadius=55,20 z=0,120 initialPhi=-45 finalPhi=45 \
                    material=Al color=1,0,0 kill=1

polycone Collimator_Right innerRadius=45,12 outerRadius=55,20 z=0,120 initialPhi=135 finalPhi=225 \
                    material=Al color=0,0,1 kill=1

polycone Collimator_Up innerRadius=45,12 outerRadius=55,20 z=0,120 initialPhi=45 finalPhi=135 \
                    material=Al color=1,1,0 kill=1

polycone Collimator_Down innerRadius=45,12 outerRadius=55,20 z=0,120 initialPhi=225 finalPhi=315 \
                    material=Al color=0,1,0 kill=1

#polycone Collimator_2 outerRadius=28.5,10 z=0,120 kill=0 \
                    color=0,1,1 material=Vacuum
place Collimator_Right z=9515.21
place Collimator_Left z=9515.21
place Collimator_Up z=9515.21
place Collimator_Down z=9515.21

zntuple beam1 zloop=9515:9635:5 format=rootExtended             #COL scan
#zntuple beam1 zloop=-500:9700:20 format=rootExtended
#zntuple beam1 zloop=969:6580:50 format=rootExtended
#zntuple beam1 zloop=6550:6650:4 referenceParticle=1 format=rootExtended

#place det z=8050 rename=detend

#Detectors
#place det z=430 rename=detbeforeQA
#place detbig z=430 rename=detbeforeQA
#place det z=950 rename=detafterQB
#place detbig z=950 rename=detafterQB
place det z=2800 rename=detbeforeWall
place detbig z=2800 rename=detbeforeWall
place det z=6585 rename=detbeforeQC
place detbig z=6588 rename=detbeforeQCbig
place det z=9500 rename=detbeforeCOLL
place detbig z=9500 rename=detbeforeCOLL



#profile zloop=-600:1600:10 particle=proton file=beam_width.txt

output $histofile.out
```

B.2 Beam positioning studies with BLM

```
#physics library
physics QGSP_BERT

# Material Definition
material Inox Cr,0.19 Ni,0.11 Fe,0.7 density=8.03
material AIR C,0.000124 N,0.755268 O,0.231781 Ar,0.012827 state=g \
    density=0.00120479
material AIRtube C,0.000124 N,0.755268 O,0.231781 Ar,0.012827 state=g \
    density=0.00120479*1.6e-6
material tube Mg,0.0090 Si,0.0100 Mn,0.0070 Fe,0.0025 Al,0.9715 density=2.70

param worldMaterial=Vacuum

param M=938.272 KE=70.3
param P=sqrt(($M+$KE)*($M+$KE)-$M*$M)
param xbeam=0          #beam_positioning_X
param ybeam=0          #beam_positioning_Y
beam gaussian nEvents=10000 particle=proton beamZ=-900 beamX=$xbeam beamY=$ybeam  \
             sigmaX=3.911 sigmaY=4.762 sigmaZ=1 meanMomentum=$P sigmaP=0.26 sigmaT=0.0 meanT=0.0 \
             sigmaXp=0.0015 sigmaYp=0.001 meanXp=0.001



reference particle=proton referenceMomentum=$P

box BeamVis width=100.0 height=100.0 length=0.500 \
            material=Vacuum color=1,0,0

place BeamVis z=-900


#switching magnet
param swicurrent=87.55

idealsectorbend switching angle=-40 By=0.0048*$swicurrent+0.9414 fieldCenterRadius=906.67 \
                          fieldInnerRadius=856.67 fieldMaterial=AIRtube\
                         fieldOuterRadius=956.67 fieldHeight=110 ironInnerRadius=851.67\
                          ironOuterRadius=961.67 ironHeight=120 ironColor=1,1,0 ironMaterial=Fe kill=0
place switching z=-582.79 x=0 y=0
cornerarc angle=-40 z=-582.79 centerRadius=906.67

#  parameter of steer
param inputcurrent_steerX=0
param inputcurrent_steerY=0
#  definition of steer

genericbend SteeringX fieldWidth=239.9 fieldHeight=239.9 fieldLength=490 \
    ironHeight=240 ironLength=300 ironWidth=240 By=0.0115*abs($inputcurrent_steerX)+0.0004 \
    ironColor=1,1,0 fringeFactor=0.2 kill=0 fieldColor=0.6,0.6,0

genericbend SteeringY fieldWidth=239.9 fieldHeight=239.9 fieldLength=490 \
    ironHeight=240 ironLength=300 ironWidth=240 By=-(0.0115*abs($inputcurrent_steerY)+0.0004)\
    ironColor=1,1,0 fringeFactor=0.2 kill=0 fieldColor=0.6,0.6,0

place SteeringX z=150 rotation=Z0
place SteeringY z=150 rotation=Z90


detector detY height=50 width=105 length=50 material=Cu maxStep=1 kill=0 color=0.1,1,0.6
detector detX height=105 width=50 length=50 material=Cu maxStep=1 kill=0 color=0.1,1,1
virtualdetector endbeamcurent radius=55 length=10 color=1,1,1 maxStep=1 format=rootExtended kill=1 \
                                                        referenceParticle=0

place detX z=6610 x=-70 rename=detright1
place detX z=6610 x=70 rename=detleft1
place detY z=6610 y=70 rename=dettop1
place detY z=6610 y=-70 rename=detbottom1
place detX z=9400 x=-70 rename=detright2
place detX z=9400 x=70 rename=detleft2
place detY z=9400 y=-70 rename=dettop2
place detY z=9400 y=70 rename=detbottom2
place endbeamcurent z=9900


tubs pipewalltocoll innerRadius=50 outerRadius=51.5 length=5500 material=tube color=0,0.6,0.6 kill=0

place pipewalltocoll z=6775

tubs pipedipoletowall innerRadius=50 outerRadius=51.5 length=570 material=tube color=0,0.6,0.6 kill=0

place pipedipoletowall z=3738

tubs pipedipoletowall innerRadius=50 outerRadius=51.5 length=3500 material=tube color=0,0.6,0.6 kill=0

place pipedipoletowall z=1700


param inputcurrent_QA=-20
param inputcurrent_QB=32
param inputcurrent_QC=-40
param inputcurrent_QD=20    #scan 20-65 step of 5 amps
```

```
genericquad Quad1 fieldLength=256 apertureRadius=55 ironRadius=70 \
    ironLength=205 coilRadius=18 coilHalfwidth=2 fringeFactor=0.1 \
        ironColor=1.0,1.0,1.0 gradient=0.0761*abs($inputcurrent_QA)+0.1981 kill=0

genericquad Quad2 fieldLength=256 apertureRadius=55 ironRadius=70 \
    ironLength=205 coilRadius=18 coilHalfwidth=2 fringeFactor=0.1 \
        ironColor=1.0,1.0,1.0 gradient=-(0.0761*$inputcurrent_QB+0.1981) kill=0

genericquad Quad3 fieldLength=256 apertureRadius=55 ironRadius=70 \
    ironLength=205 coilRadius=18 coilHalfwidth=2 fringeFactor=0.1 \
        ironColor=1.0,1.0,1.0 gradient=0.0761*abs($inputcurrent_QC)+0.1981 kill=0

genericquad Quad4 fieldLength=256 apertureRadius=55 ironRadius=70 \
    ironLength=205 coilRadius=18 coilHalfwidth=2 fringeFactor=0.1 \
        ironColor=1.0,1.0,1.0 gradient=-(0.0761*$inputcurrent_QD+0.1981) kill=0

place Quad1 z=537.5
place Quad2 z=841
place Quad3 z=6806.71
place Quad4 z=7212.71

param histoFile=genericsectorbend_QD_SCAN_($inputcurrent_QD)
param histofile=genericsectorbend_QD_SCAN_($inputcurrent_QD)

polycone wall innerRadius=56,56 outerRadius=1000,1000 z=0,3700 material=CONCRETE \
    kill=1 color=0,1,0
place wall z=2815.21

group colli2 radius=0.0 material=AIRtube
#construct collimator
#colli top
virtualdetector collimator width=15.53 length=110.82 height=0.1 format=rootExtended color=0,1,0
place collimator z=54.5 x=0 y=38.64 rename='+top-mid' rotation=Z0,X10.4
place collimator z=54.5 x=20 y=34.64 rename='+top-left' rotation=Z-30,X10.4
place collimator z=54.5 x=-20 y=34.64 rename='+top-right' rotation=Z30,X10.4
ntuple colli_top1 detectors=colli2top-mid,colli2top-left,colli2top-right union=1
#colli down
place collimator z=54.5 x=0 y=-38.64  rename='+down-mid' rotation=Z0,X-10.4
place collimator z=54.5 x=20 y=-34.64 rename='+down-left' rotation=Z30,X-10.4
place collimator z=54.5 x=-20 y=-34.64 rename='+down-right' rotation=Z-30,X-10.4
ntuple colli_down1 detectors=colli2down-mid,colli2down-left,colli2down-right union=1
#colli left
place collimator z=54.5 y=0 x=38.64  rename='+left-mid' rotation=Z90,Y-10.4
place collimator z=54.5 y=20 x=34.64 rename='+left-top' rotation=Z-60,Y-10.4
place collimator z=54.5 y=-20 x=34.64  rename='+left-down' rotation=Z60,Y-10.4
ntuple colli_left1 detectors=colli2left-mid,colli2left-top,colli2left-down union=1
#colli right
place collimator z=54.5 y=0 x=-38.64 rename='+right-mid' rotation=Z90,Y10.4
place collimator z=54.5 y=20 x=-34.64 rename='+right-top' rotation=Z60,Y10.4
place collimator z=54.5 y=-20 x=-34.64 rename='+right-down' rotation=Z-60,Y10.4
ntuple colli_right1 detectors=colli2right-mid,colli2right-top,colli2right-down union=1


#colli top
virtualdetector collimator2 width=5.18 length=110.82 height=0.1 format=rootExtended color=0,1,0
place collimator2 z=163.5 x=0 y=19.32 rename='+top-mid2' rotation=Z0,X10.4
place collimator2 z=163.5 x=10 y=17.32 rename='+top-left2' rotation=Z-30,X10.4
place collimator2 z=163.5 x=-10 y=17.32 rename='+top-right2' rotation=Z30,X10.4
ntuple colli_top2 detectors=colli2top-mid2,colli2top-left2,colli2top-right2 union=1
#colli down
place collimator2 z=163.5 x=0 y=-19.32  rename='+down-mid2' rotation=Z0,X-10.4
place collimator2 z=163.5 x=10 y=-17.32 rename='+down-left2' rotation=Z30,X-10.4
place collimator2 z=163.5 x=-10 y=-17.32 rename='+down-right2' rotation=Z-30,X-10.4
ntuple colli_down2 detectors=colli2down-mid2,colli2down-left2,colli2down-right2 union=1
#colli left
place collimator2 z=163.5 y=0 x=19.32  rename='+left-mid2' rotation=Z90,Y-10.4
place collimator2 z=163.5 y=10 x=17.32 rename='+left-top2' rotation=Z-60,Y-10.4
place collimator2 z=163.5 y=-10 x=17.32  rename='+left-down2' rotation=Z60,Y-10.4
ntuple colli_left2 detectors=colli2left-mid2,colli2left-top2,colli2left-down2 union=1
#colli right
place collimator2 z=163.5 y=0 x=-19.32 rename='+right-mid2' rotation=Z90,Y10.4
place collimator2 z=163.5 y=10 x=-17.32 rename='+right-top2' rotation=Z60,Y10.4
place collimator2 z=163.5 y=-10 x=-17.32 rename='+right-down2' rotation=Z-60,Y10.4
ntuple colli_right2 detectors=colli2right-mid2,colli2right-top2,colli2right-down2 union=1
ntuple colli_right detectors=colli2right-mid,colli2right-top,colli2right-down,\
                    colli2right-mid2,colli2right-top2,colli2right-down2 union=1
ntuple colli_left detectors=colli2left-mid,colli2left-top,colli2left-down,colli2left-mid2,\
                    colli2left-top2,colli2left-down2 union=1
ntuple colli_top detectors=colli2top-mid,colli2top-left,colli2top-right,colli2top-mid2,\
                    colli2top-left2,colli2top-right2 union=1
ntuple colli_down detectors=colli2down-mid,colli2down-left,colli2down-right,\
                    colli2down-mid2,colli2down-left2,colli2down-right2 union=1
ntuple colli_X detectors=colli2left-mid,colli2left-top,colli2left-down,colli2left-mid2,\
                    colli2left-top2,colli2left-down2,colli2right-mid,colli2right-top,colli2right-down,\
                    colli2right-mid2,colli2right-top2,colli2right-down2 union=1
ntuple colli_Y detectors=colli2down-mid,colli2down-left,colli2down-right,colli2down-mid2,\
                    colli2down-left2,colli2down-right2,colli2top-mid,colli2top-left,colli2top-right,\
                    colli2top-mid2,colli2top-left2,colli2top-right2 union=1
endgroup

place colli2 z=9635.21


output $histofile.out
```

Appendix C

STRIPPER FOIL AZIMUTH SETTINGS CONVERSION

The settings of the stripping sheet are measured in mm at ARRONAX. This has been converted to degrees. This is done to get a more physical feel of the stripper foil angle. This azimuthal angle of the stripper foil is measured relative to the central position of the cyclotron. The experimental data for the stripper foil azimuth is then converted to degrees which follow a linear relationship as shown in the figure below:

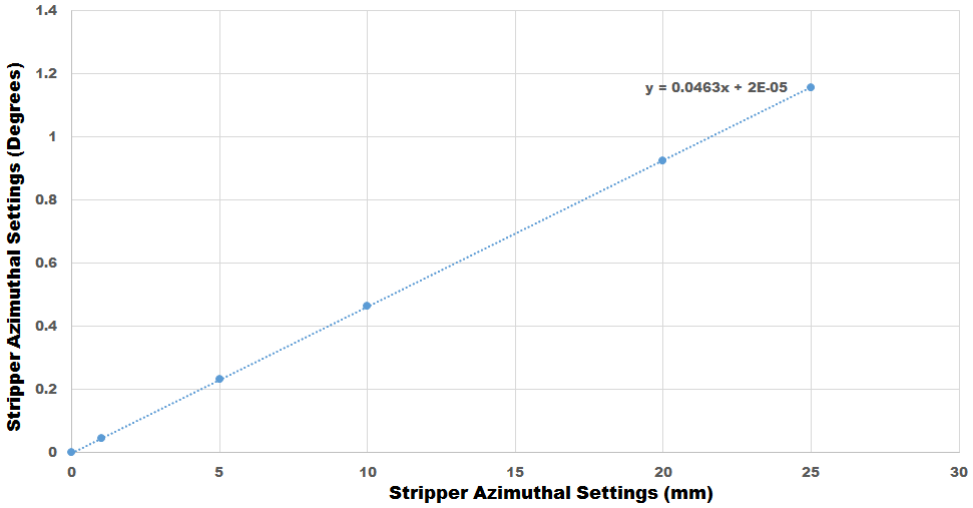

Appendix D

BPM CALIBRATION PYEPICS CODE

```
from epics import PV
from time import sleep, time
from numpy import arange
import numpy as np
import array as Arrlist
import epics
import datetime

calibrationGo = PV('XYTIOC:CALIBRATION:GO')

# MLR Coefficients based on data analysis
XP1 = PV('XYTIOC:XP1')  # X position probe 1 Coef
XP2 = PV('XYTIOC:XP2')  # X position probe 2 Coef
XP3 = PV('XYTIOC:XP3')  # X position probe 3 Coef
XP4 = PV('XYTIOC:XP4')  # X position probe 4 Coef
XINT = PV('XYTIOC:XINT')  # X position intercept Coef
YP1 = PV('XYTIOC:YP1')  # Y position probe 1 Coef
YP2 = PV('XYTIOC:YP2')  # Y position probe 2 Coef
YP3 = PV('XYTIOC:YP3')  # Y position probe 3 Coef
YP4 = PV('XYTIOC:YP4')  # Y position probe 4 Coef
YINT = PV('XYTIOC:YINT')  # Y position intercept Coef

XP1.value=0
XP2.value=0
XP3.value=0
XP4.value=0
XINT.value=0

YP1.value=0
YP2.value=0
YP3.value=0
YP4.value=0
YINT.value=0

# RF level And switching and sensing
RFLevel = PV('XYTIOC:CH1:power_W')
RFLevelArray = []
RFLevelArray.append(PV('XYTIOC:RF_LEVEL1'))
RFLevelArray.append(PV('XYTIOC:RF_LEVEL2'))
RFLevelArray.append(PV('XYTIOC:RF_LEVEL3'))
RFLevelArray.append(PV('XYTIOC:RF_LEVEL4'))
RFSwith1 = PV('XYTIOC:SWITCH1')
RFSwith2 = PV('XYTIOC:SWITCH2')
RFSwith3 = PV('XYTIOC:SWITCH3')
RFSwith4 = PV('XYTIOC:SWITCH4')
SENSE1 = PV('XYTIOC:SENSE1:INPUT')
SENSE2 = PV('XYTIOC:SENSE2:INPUT')
SENSE3 = PV('XYTIOC:SENSE3:INPUT')
SENSE4 = PV('XYTIOC:SENSE4:INPUT')
ESTOP = PV('XYTIOC:ESTOP:INPUT')
```

```
    # Set points and Readback
    motorSetpointY = PV('XYTIOC:Y:setpoint')
    motorSetpointX = PV('XYTIOC:X:setpoint')
    motorReadbackY = PV('XYTIOC:Y:readback')
    motorReadbackX = PV('XYTIOC:X:readback')
    predictedX = PV('XYTIOC:XPREDICT')
    predictedY = PV('XYTIOC:YPREDICT')
    rErrorX = PV('XYTIOC:XERROR')
    rErrorY = PV('XYTIOC:YERROR')
    # Motor Drive and Mode
    motorDriveEnableX = PV('XYTIOC:X:driveEnable')
    motorDriveEnableY = PV('XYTIOC:Y:driveEnable')
    motorDriveModeX = PV('XYTIOC:X:snlState')
    motorDriveModeY = PV('XYTIOC:Y:snlState')
    # Delays
    motordelay = 1  #Delay before everythings starts
    multiplexdelay = 0.1  #Delay is there not to kill computer
    estopDelay = 1  #Delay after stopping everything
    switchDelay = 0.01                                          #Delay for the rfsc
    # Motor Drive and Mode Switching
    motorDriveModeX.put(0, wait=True)
    motorDriveModeY.put(0, wait=True)
    motorDriveEnableX.put(0, wait=True)
    motorDriveEnableY.put(0, wait=True)
    sleep(motordelay)
    motorDriveModeX.put(1, wait=True)
    motorDriveModeY.put(1, wait=True)
    motorDriveEnableX.put(1, wait=True)
    motorDriveEnableY.put(1, wait=True)
    # Setpoints
    ymax = 10
    xmax = 10
    ymin = -10
    xmin = -10
    xstep = 1
    ystep = 1
    x = xmin
    y = ymin
    positionalErrorX = 0.001
    positionalErrorY = 0.001
    # Lists
    finalValue = []
    multiplexOUT = []
    errorXY = []
def RFSwitch(channel):
    RFSwith1.put(0, wait=True)
    RFSwith2.put(0, wait=True)
    RFSwith3.put(0, wait=True)
    RFSwith4.put(0, wait=True)
    if (channel == 1):
        RFSwith1.put(1, wait=True)
        while (not (SENSE1.value)):
            pass
    elif (channel == 2):
        RFSwith2.put(1, wait=True)
        while (not (SENSE2.value)):
            pass
    elif (channel == 3):
        RFSwith3.put(1, wait=True)
        while (not (SENSE3.value)):
            pass
    elif (channel == 4):
        RFSwith4.put(1, wait=True)
        while (not (SENSE4.value)):
            pass


motorSetpointY.put(y, wait=True)
motorSetpointX.put(x, wait=True)
sleep(motordelay)
finalValue.append([
    '#X:', 'Y:', 'errorX:', 'errorY:', 'rfch', 'rfvalue', 'rfch', 'rfvalue',
    'rfch', 'rfvalue', 'rfch', 'rfvalue'
])
print("Calculating")
```

```
try:
    for y in arange(ymax, ymin - ystep, -ystep):  #Y steps
        if (y < ymin):
            y = ymin

        motorSetpointY.put(y, wait=True, timeout=1000)
        sleep(multiplexdelay)
        if not (ESTOP.value):
            raise Exception('ESTOP pressed')  #ESTOP pressed
        print("Calculating Y")
        while (abs(motorReadbackY.value - motorSetpointY.value) >
               positionalErrorY):
            print("Calculating Y POS")  #Setting Position On The Y Axis
            sleep(multiplexdelay)  #Delay is there not to kill computer
            if not (ESTOP.value):
                raise Exception('ESTOP pressed')  #ESTOP pressed
        while (abs(motorReadbackX.value - motorSetpointX.value) >
               positionalErrorX):
            print("Calculating XR POS")  #Setting Position On The X Axis
            sleep(multiplexdelay)
            if not (ESTOP.value):
                raise Exception('ESTOP pressed')  #ESTOP pressed

        print("Calculating XR")
        sleep(1)
        for x in arange(xmin, xmax + xstep, xstep):
            if (x > xmax):
                x = xmax

                #X steps
            if not (ESTOP.value):
                raise Exception('ESTOP pressed')

            motorSetpointX.put(x, wait=True)
            sleep(multiplexdelay)
            while (abs(motorReadbackX.value - motorSetpointX.value) >
                   positionalErrorX):
                print("Calculating XR POS")
                sleep(multiplexdelay)
                if not (ESTOP.value):
                    raise Exception('ESTOP pressed')  #ESTOP pressed
            coodinates = [x, y]  #Setting Position On The X Axis
            errorX = abs(motorReadbackX.value -
                         motorSetpointX.value)  #Calculating errorX
            errorY = abs(motorReadbackY.value -
                         motorSetpointY.value)  #Calculating errorY
            errorXY = [errorX, errorY]

            del multiplexOUT[:]
            for i in range(1, 5, 1):
```

```
                if not (ESTOP.value):
                    raise Exception('ESTOP pressed')  #ESTOP pressed
                RFSwitch(i)
                sleep(switchDelay)  #Wait for RF to settle

                RFLevelArray[i - 1].put(RFLevel.value, wait=True)
                #sleep(0.25)

                multiplexOUT.extend([i, RFLevel.value])
            sleep(0.1)
            rErrorX.value = motorReadbackX.value - predictedX.value
            rErrorY.value = motorReadbackY.value - predictedY.value
            finalValue.append(coodinates + errorXY +
                              multiplexOUT)  #Putting in a list

        if (x >= xmax):  #Checking if the the x table is in the end
            print("Calculating XL")
            if not (ESTOP.value):
                raise Exception('ESTOP pressed')  #ESTOP pressed
            x = xmin
            motorSetpointX.put(
                xmin, wait=True
            )  #Setting Position Back To Original Place On The X Axis
            while (abs(motorReadbackX.value - motorSetpointX.value) >
                   positionalErrorX):
                print("Calculating XL POS")
                sleep(multiplexdelay)
                if not (ESTOP.value):
                    raise Exception('ESTOP pressed')  #ESTOP pressed

    # print(finalValue)

    for row in finalValue:
        print('   '.join([str(elem) for elem in row]))

    np.savetxt(
        "/home/ioctrain1/Python/atul/NewCode/NewBPMoutputAtul_1mm_30.45Mhz_5dBm+-10mm.txt",
        finalValue,
        fmt='%s',
        delimiter='\t')

    motorDriveEnableX.put(0, wait=True)
    motorDriveEnableY.put(0, wait=True)
    motorDriveModeX.put(0, wait=True)
    motorDriveModeY.put(0, wait=True)
    RFSwith1.put(0, wait=True)
    RFSwith2.put(0, wait=True)
    RFSwith3.put(0, wait=True)
    RFSwith4.put(0, wait=True)
except Exception as inst:
    print(inst)
    motorDriveEnableX.put(0, wait=True)
    motorDriveEnableY.put(0, wait=True)
    motorDriveModeX.put(0, wait=True)
    motorDriveModeY.put(0, wait=True)
    RFSwith1.put(0, wait=True)
    RFSwith2.put(0, wait=True)
    RFSwith3.put(0, wait=True)
    RFSwith4.put(0, wait=True)
    sleep(estopDelay)

except:
    print("exited abnormally")
    motorDriveEnableX.put(0, wait=True)
    motorDriveEnableY.put(0, wait=True)
    motorDriveModeX.put(0, wait=True)
    motorDriveModeY.put(0, wait=True)
    RFSwith1.put(0, wait=True)
    RFSwith2.put(0, wait=True)
    RFSwith3.put(0, wait=True)
    RFSwith4.put(0, wait=True)
    sleep(estopDelay)
```

Bibliography

[1] Particle Therapy Co Operative Group (PTCOG), facilities under construction/in planning stage, https://www.ptcog.ch/, data from the website as of November 2020.

[2] Conference Cyclotron and Applications 2019, several presentation therein, https://indico.jacow.org/event/14/

[3] L.Cabretta et al., Review of High Power Cyclotrons and their Applications, in Proc. 18th Int. Conf. on Cyclotrons and Their Applications (Cyclotrons'19), Sep 2019, Cape Town, South Africa, https://doi.org/10.18429/JACoW-Cyclotrons2019-THB01

[4] ARRONAX, https://www.ARRONAX-nantes.fr

[5] R.W. Hamm, "Review of industrial accelerators and their applications", IAEA, Vienna, Austria.

[6] H. Koziol, "Beam diagnostics for accelerators", CERN, Geneva, Switzerland.

[7] L. Medeiros Romao et al., Iba C70 Cyclotron Development, in Proc. 18th Int. Conf. on Cyclotrons and Their Applications (Cyclotrons'07), Giardini-Naxos, Italy, Oct. 2007, pp. 54–56.

[8] N. Angert, "Ion sources", GSI, Darmstadt, Germany.

[9] R. Trass, "Development of ECR ion source", IAMP, Universität Giessen, Germany.

[10] D. Leitner, D. Todd, D. Winklehner, "Fundamentals of ion sources", U.S. Particle Accelerator School (USPAS).

[11] W. Kleeven et al., Injection and Central Region Design For The Iba C70 Cyclotron, in Proc. 18th Int. Conf. on Cyclotrons and Their Applications (Cyclotrons'07), Giardini-Naxos, Italy, Oct. 2007, pp. 66–68.

[12] Mike Seidel, "Cyclotrons", CERN Accelerator School-Introductory Course, Constanta, Sep. 2018.

[13] W. Kleeven and S. Zaremba, "Cyclotrons: magnetic design and beam dynamics", Louvain-La-Neuve, Belgium, Sep. 2018.

[14] F. Poirier et al., On-Going Operations with the Cyclotron C70 ARRONAX, in Proc. 20th Int. Conf. on Cyclotrons and their Applications (Cyclotrons'13), Vancouver, Canada, Sep. 2013, paper MOPPT010, pp. 49–51.

[15] S. Zaremba et al., Magnetic Field Design and Calculations For The Iba C70 Cyclotron, in Proc. 18th Int. Conf. on Cyclotrons and Their Applications (Cyclotrons'07), Giardini-Naxos, Italy, Oct. 2007, pp. 75–77.

[16] LabVIEW for Measurement and Data Analysis,https://www.ni.com/fr-fr/innovations/white-papers/06/labview-for-measurement-and-data-analysis.html

[17] Olli Tarvainen, Studies of electron cyclotron resonance ion source plasma physics, Department of physics university of Jyavaskyla research Report No. 8/2005.

[18] Zaremba Simon et al., Cyclotrons: Magnetic Design and Beam Dynamics, in Proc, CAS-CERN Accelerator School: Accelerators for Medical Applications, Austria, Jun. 2015, pp. 177–239.

[19] W. Beeckman et al., Machining and Assembly Of The Iba C70 Cyclotron Magnet, in Proc. 18th Int. Conf. on Cyclotrons and Their Applications (Cyclotrons'07), Giardini-Naxos, Italy, Oct. 2007, pp. 81–83.

[20] Roland Trassl, Development of ECR ion source, IAMP, Universitat Giessen, Germany.

[21] W. Kleeven, Injection and extraction for cyclotrons, in Ion Beam Applications (IBA), Louvain-la-Neuve, Belgium, pp. 271–296.

[22] Ghithan et al., On-line measurements of proton beam current from a PET cyclotron using a thin aluminum foil, in Journal of Instrumentation- vol. 8, Jul. 2013, doi:10.1088/1748-0221/8/07/P07010.

[23] G. G. Gulbekyan, O. N. Borisov, and V. I. Kazacha and D, Extraction By Stripping Of Heavy Ion Beams From Avf Cyclotrons, in Proc. 18th Int. Conf. on Cyclotrons and Their Applications (Cyclotrons'07), Giardini-Naxos, Italy, Oct. 2007, pp. 308–313.

[24] Y. Bylinskii, R. A. Baartman, P. E. Dirksen, Y.-N. Rao, and V. A. Verzilov, Recent Developments for Cyclotron Extraction Foils at TRIUMF, in Proc. 9th Int. Particle Accelerator Conf. (IPAC'18), Vancouver, Canada, Apr.-May 2018, pp. 1159–1162. doi:10.18429/JACoW-IPAC2018-TUPAL062

[25] Uggerhøj et al., Diamond crystals for H- injection, in Physical Review Special Topics-accelerators and Beams - PHYS REV SPEC TOP-AC- vol. 5, Jul. 2002, doi: 10.1103/PhysRevSTAB.5.073501.

[26] D. Vandeplassche et al., Extraction Simulations For The Iba C70 Cyclotron, in Proc. 18th Int. Conf. on Cyclotrons and Their Applications (Cyclotrons'07), Giardini-Naxos, Italy, Oct. 2007, pp. 63–65.

[27] A. Adelmann, P. Arbenz, C. Kraus, and M. Wittberger, Comparison of h- and p- Refinement in a Finite Element Maxwell Time Domain Solver, in Proc. 9th Int. Computational Accelerator Physics Conf. (ICAP'06), Chamonix, Switzerland, Oct. 2006, paper WEA4IS04, pp. 288–288.

[28] A. Adelmann, P. Arbenz, C. Kraus, and M. Wittberger, Comparison of h- and p- Refinement in a Finite Element Maxwell Time Domain Solver, in Proc. 9th Int. Computational Accelerator Physics Conf. (ICAP'06), Chamonix, Switzerland, Oct. 2006, paper WEA4IS04, pp. 288–288.

[29] A. Fedorova and M. Zeitlin, Multiscale Representations for Solutions of Vlasov-Maxwell Equations for Intense Beam Propagation, in Proc. 7th European Particle Accelerator Conf. (EPAC'00), Vienna, Austria, Jun. 2000, paper TUP2B18.

[30] S. N. Andrianov and A. I. Dvoeglazov, Matrix Representation for the Vlasov-Maxwell Equation Solution, in Proc. 7th European Particle Accelerator Conf. (EPAC'00), Vienna, Austria, Jun. 2000, paper MOP4A14.

[31] Frank Hinterberger, Physics of particle accelerators and ion optics, Springer, 2008.

[32] F. Ruggiero et al., CAS basic course on general accelerator physics, CERN, Jun. 2005.

[33] D. Möhl, Sources of Emittance Growth, CERN, Geneva, Switzerland, pp 245-269.

[34] D. Edwards and M. Syphers, An Introduction to the Physics of High Energy Accelerators, Wiley, New York, 1993, Chapter 7: Emittance preservation.

[35] Particle Data Group, Review of particle physics, Eur. Phys. J. 3 (1998) 144. (Chapter 23, Passage of particles through matter).

[36] S. Hojo, A. Goto, T. Honma, K. Katagiri, and A. Sugiura, Observation of Longitudinal Space Charge Effects in the Injection Beam Line of NIRS-930 Cyclotron, in Proc. 3rd Int. Particle Accelerator Conf. (IPAC'12), New Orleans, LA, USA, May 2012, paper MOPPD028, pp. 427–429.

[37] D. J. Scott, D. Capista, I. K banis, K. Seiya, and M.-J. Yang, Single/Few Bunch Space Charge Effects at 8 GeV in the Fermilab Main Injector, in Proc. 3rd Int. Particle Accelerator Conf. (IPAC'12), New Orleans, LA, USA, May 2012, paper MOPPC018, pp. 163–165.

[38] Y. Shobuda, M. Yamamoto, Y. H. Chin, and F. Tamura, Mitigation of Beam Instability due to Space Charge Effects at 3 GeV RCS in J-PARC, in Proc. 2nd Int. Particle Accelerator Conf. (IPAC'11), San Sebastian, Spain, Sep. 2011, paper MOPS004, pp. 595–597.

[39] G. Hortig, A Beam Scanner for two Dimensional Scanning with one rotating Wire, in NIM 30 (1964), p. 355-356

[40] M.G. Minty and F. Zimmerman, Measurement and control of charged particle beams, Springer, 2003, Chap 4.

[41] Enrico Bravin, Transverse profile measurement, CERN Accelerator School on Beam Instrumentation, Tuusula, Finland, Jun. 2018.

[42] Min Zhang, Emittance formula for slits and pepper-pot measurement, FNAL, Illinois, US, Oct. 1996.

[43] J. Wenniinger Linear imperfection, CERN Accelerator School on Beam Instrumentation, Tuusula, Finland, Jun. 2018.

[44] K.L. Brown et al., Effect of beam line magnetic misalignments, Nucl. Instrum. Methods, Netherlands- vol. 141:3, Mar. 1977, doi:10.1016/0029-554X(77)90628-0

[45] Silvia Masciocchi, Interaction of particles with matter-1, GSI and University of Heidelberg, Germany, Apr. 2017.

[46] L. William, Techniques for Nuclear and Particle Physics Experiments, Springer, 1994, doi:10.1007/978-3-642-57920-2.

[47] Scintillator detectors, https://www.science.mcmaster.ca/radgrad/images/6R06CseResces/4R6Notes4_ScintillationDetectors.pdf

[48] Gas ionization detectors, https://www.nuclear-power.net/nuclear-engineering/radiation-detection/gaseous-ionization-detector/

[49] A. Zhukov, Beam Loss Monitors (BLMS): Physics Simulations and Applications in Accelerators, in Proceedings of BIW10, Santa Fe, New Mexico, US.

[50] Introduction to radiation monitors, https://www.equipcoservices.com/support/tutorials/introduction-to-radiation-monitors/

[51] Gas detectors, https://science.mcmaster.ca/radgrad/images/6R06CseResces/4R6Notes3_GasFilled_Detectors.pdf

[52] Robert.EShafer, A Tutorial on Beam Loss Monitoring, TechS ce, Inc. Santa Fe, NM.

[53] K. Satou, N. Kamikubota, T. Toyama, S. Yamada, and S. Y. Yoshida, Development of Wide Dynamic Range Beam Loss Monitor System for the J-PARC Main Ring, in Proc. 8th Int. Particle Accelerator Conf. (IPAC'17), Copenhagen, Denmark, May 2017, pp. 1248–1251. doi:10.18429/JACoW-IPAC2017-TUOAB3

[54] Toyama T et al., in 2008 Proc. Advanced Beam Dynamics Workshop on High-Intensity, High Brightness Hadron Beams, 25-29 Aug. 2008 (Nashville) pp. 450.

[55] V. Grishin et al., A FAMILY OF GAZ IONIZATION CHAMBERS and SEM FOR BEAM LOSS MONITORING OF LHC and OTHER ACCELERATORS, in Proc. 26th Russian Particle Accelerator Conf. (RUPAC'18), Protvino, Russia.

[56] K. Wittenburg, Beam loss monitors, DESY, Hamburg, Germany.

[57] A. A. Nosych and U. Iriso, Studies and Historical Analysis of ALBA Beam Loss Monitors, in Proc. 5th Int. Beam Instrumentation Conf. (IBIC'16), Barcelona, Spain, Sep. 2016, pp. 94–97. doi:10.18429/JACoW-IBIC2016-MOPG22

[58] F. Pérez, I. Birkel, K. Hertkorn, E. Huttel, A.-S. Müller, and M. Pont, Studies using Beam Loss Monitors at ANKA, in Proc. 9th European Particle Accelerator Conf. (EPAC'04), Lucerne, Switzerland, Jul. 2004, paper THPKF023.

[59] Lei Hou et al., Beam Loss Monitor System for SSRF Storage Ring, in Journal of NUCLEAR SCIENCE and TECHNOLOGY, Supplement 5, Jun. 2008, pp. 425–427.

[60] Kay Wittenburg, The PIN-Diode Beam Loss Monitor system at HERA, in 9th Beam Instrumentation Workshop, Boston, USA, Volume: AIP Conf. Proc. 546, 3 (2000).

[61] A.J. Kozubal et al., Run-time environment and application tools for the ground test accelerator control system, in Nuclear Instruments and Methods in Physics Research Section A: Accelerators, Spectrometers, Detectors and Associated Equipment, 293 (1–2): 288–291. doi:10.1016/0168-9002(90)91446-I

[62] Cosy Infinity, http://www.bt.pa.msu.edu/index_cosy.htm

[63] T. J. Roberts, http://g4beamline.muonsinc.com

[64] The Geant4 Collaboration, http://geant4.web.cern.ch/geant4/

[65] M. V. Shankar, L. F. Li, M. A. Davidsaver, and M. G. Konrad, The EPICS Archiver Appliance, in Proc. 15th Int. Conf. on Accelerator and Large Experimental Physics Control Systems (ICALEPCS'15), Melb ne, Australia, Oct. 2015, pp. 761–764. doi:10.18429/JACoW-ICALEPCS2015-WEPGF030

[66] EPICS website, https://epics.anl.gov/projects.php

[67] J.H. Kim, Numerical Simulation of a Multi-Cusp Ion source for High Current H- Cyclotron at RISP, Rare Isotope Science Project (RISP), Institute for Basic Science (IBS), 70 Yuseong-daero 1689-gil, Yusung-gu, Daejeon, 305-811 Korea.

[68] J.-O. Lill, Charge integration in external-beam PIXE, Nuclear Instruments and Methods in Physics Research B 150 (1999) 114-117.

[69] F. Poirier et al., Studies and Upgrades on the C70 Cyclotron ARRONAX, in Proc. 21th Int. Conf. on Cyclotrons and their Applications (Cyclotrons'16), Zurich, Switzerland, Sep. 2016, pp. 235–237. doi:10.18429/JACoW-Cyclotrons2016-TUD02

[70] Xiao LI, Study of beam losses and monitor for the A1 beamline of the cyclotron ARRONAX, IMT Atlantique, Nantes, France, Jun. 2014.

[71] Shuang NING, Beam Data Studies and Measurements for C70 High-intensity Operations in ARRONAX, IMT Atlantique, Nantes, France, Aug. 2017.

[72] iThemba Labs website, https://tlabs.ac.za/

[73] Peter Forck, Dmitry Liakin and Piotr Kowina, Beam Position Monitors, Gesellschaft fur Schwerionenforschung GSI, Darmstadt, German

[74] Opera3D, https://www.3ds.com/products-services/simulia/products/opera/

[75] D. T. F ie et al., Non-Destructive Beam Position Measurement in a Proton Therapy Beam Line, in Proc. 9th European Workshop on Beam Diagnostics and Instrumentation for Particle Accelerators (DIPAC'09), Basel, Switzerland, May 2009, paper MOPD01, pp. 41–43.

[76] PyEpics, https://pypi.org/project/pyepics/

[77] React Automation studio, https://github.com/wduckitt/React-Automation-Studio

[78] Monopole Antenna, https://www.sciencedirect.com/topics/computer-science/monopole-antenna

[79] J. Dietrich, A. H. Botha, J. L. Conradie, J. L. G. Delsink, I. Mohos, and P. F. Rohwer, Beam Position Monitor Development for the IThemba LABS Cyclotron Beamlines, in Proc. 9th European Particle Accelerator Conf. (EPAC'04), Lucerne, Switzerland, Jul. 2004, paper THPLT047.

[80] https://www.ipellejero.es/hf/antenas/monopolo/english.php

[81] K.-U. Kasemir, Control System Studio (CSS) Data Browser, in Proc. 7th Int. Workshop on Personal Computers and Particle Accelerator Controls (PCaPAC'08), Ljbuljana, Slovenia, Oct. 2008, paper TUP009, pp. 99–101.

[82] K. Shroff et al, New Java Frameworks for Building Next Generation EPICS Applications, in Proceedings of ICALEPCS2019, New York, NY, USA.

[83] Vector Fields Limited, 24 Bankside, Kidlington, Oxford OX51JE, England.

[84] W.Tan, Mise en place G4Beamline pour la dynamique des faisceaux de la Ligne P1, IMT Atlantique, Nantes, France, Feb. 2011.

[85] A.Sengar, Studies towards Emittance Measurements for High Operations Intensity of C70 ARRONAX, IMT Atlantique, Nantes, France, Sep. 2016.

[86] S. G. Lebedev et al, Calculation of the lifetimes of thin stripper targets under bombardment of intense pulsed ions, in Physical review special topics - Accelerators and Beam 11, 020401 (2008), 11 Feb 2008. DOI:10.1103/PhysRevSTAB.11.020401

[87] Albert Yuen et al, Scattering effects in passive foil focusing of ion beams, in Physical review special topics - Accelerators and Beam 18, 091301 (2015), 11 Sep 2015. DOI: 10.1103/PhysRevSTAB.18.091301

[88] F.Poirier, Studies and Upgrades on the cyclotron C70 ARRONAX ppt, in Accelerator group meeting at ARRONAX, Sep 2016.

[89] Tomcat, http://tomcat.apache.org/

[90] K.L Brown, D.C. Carey et al, Transport, A computer program for designing charged particle beam transport systems, Geneva, 1973.

[91] http://www.srim.org/SRIM/SRIM2011.htm

[92] https://physics.nist.gov/cgi-bin/Star/ap_table.pl

[93] N. Pichoff, Beam dynamics basics in RF linacs, in Proc. CERN Accelerator School: Small Accelerators, Zeegse, The Netherlands, 2005, CERN-2006-012.

[94] D.G. Seely et al, Rotating dual-wire beam profile monitor optimized for use in merged-beams experiments, in Nuclear Instruments and Methods in Physics Research A 585 (2008) 69–75.

[95] D. Brandit, CERN Accelerator school on Beam diagnostics, Dourdan, France, 2008.

[96] M.Aiba (PSI), C.Carli, B.Goddard, W.Weterings, Stripping foils for the PSB H^- injection system, sLHC Project Note 0005, Nov 2009.

[97] P. Forck et al, A Scintillator based Halo-Detector for Beam Position Monitoring.

[98] Shivaramu, Scintillation Detector 1 presentation lecture, Department of Nuclear Science, UPES Dehradun, India.

UNIVERSITE MATIERE BRETAGNE MOLECULES LOIRE ET MATERIAUX

UNIVERSITÉ DE NANTES

Titre : Développement de diagnostics faisceaux et études de dynamique de faisceaux transverse pour les opérations hautes intensités au cyclotron C70XP d'ARRONAX.

Mots clés : faisceau de protons, dynamique du faisceau transversal, diagnostic du faisceau

Résumé : Les accélérateurs industriels s'appuient sur quelques nombres limités de diagnostic standard pour effectuer leurs tâches, et généralement ces limitations ne couvrent pas la connaissance précise du faisceau frappant la cible après divers événements en amont. Ceci constitue une contrainte sur la capacité de l'installation à produire les caractéristiques de poutre souhaitées mais aussi à faire face aux nouveaux développements de poutres nécessaires.
En ce sens, plusieurs caractéristiques du faisceau ont été étudiées. Dans un premier temps, des travaux ont été menés pour protéger les points faibles où les pertes de faisceau élevé peuvent entraîner une perte de vide. À cette fin, des moniteurs de perte de faisceau basés sur une chambre d'ionisation non destructive sont testés et comparés. Ces BLM ont ensuite été installés dans des lignes de lumière à haute intensité et régulièrement surveillés.
Une étude dynamique de faisceau transversal de protons de 70 MeV réalisée au BLM et au collimateur instrumenté à quatre doigts où une technique de modulation de gradient quadripolaire standard a été largement utilisée avec la modification des paramètres de la ligne de lumière. De plus, l'outil unique de simulation de suivi de particules basé sur G4Beamline geant4 a été utilisé pour étudier la dynamique des faisceaux dans des conditions idéales. Ces études ont exploré diverses caractéristiques du faisceau telles que le point focal, les causes des pertes du faisceau et l'émittance du faisceau transversal à différents jours.
Pour améliorer encore la dynamique du faisceau et évoluer vers des intensités plus élevées, un nouveau prototype de moniteur de position du faisceau (BPM) proposé par iThemba labs, Afrique du Sud, a été testé et étalonné avec une configuration d'antenne RF. répliquant un faisceau. Les résultats sont également comparés à la simulation opera3D. Ces premières études indiquent que ce BPM peut être utilisé pour calibrer un faisceau au centre. Ce BPM devrait être testé avec le faisceau de protons dans les laboratoires Arronax ou iThemba à l'avenir.

Title : Development of beam diagnostics and studies of transverse beam dynamics towards high-intensity operations in the beamlines of the C70XP cyclotron at ARRONAX.

Keywords : proton beam, transverse beam dynamics, beam diagnostics

Abstract: Industrial accelerators rely on a few limited numbers of standard diagnostics to perform their duties, and generally, this limitation does not cover precise knowledge of the beam hitting the target after various upstream events. This is a constraint for the facility's capacity in making the desired beam characteristics but also to deal with new necessary beam developments.
In this sense, several beam characteristics have been studied. Initially, the work has been done to safeguard weak locations where high beam losses can result in the loss of vacuum. For that purpose, a non-destructive ionization chamber based beam loss monitors are tested and compared. These BLMs were then installed in high-intensity beamlines and regularly monitored.
A 70 MeV proton transverse beam dynamics studies carried out at BLM and instrumented four-finger collimator levels where a standard quadrupole current variation technique has widely used with beamline settings modification. Moreover, G4Beamline geant4 based single-particle tracking simulation tool has been used to study beam dynamics in ideal conditions. These studies explored various beam characteristics such as focal point, causes of beam losses, and transverse beam emittance on different days.
For further improvement of beam dynamics and to go towards higher intensities, a new prototype of beam position monitor (BPM) proposed by iThemba labs, South Africa has been tested and calibrated with an RF antenna setup replicating a beam. The results are also compared with the opera3D simulation. These initial studies indicated that this BPM can be used for calibrating a beam at the center. This BPM is foreseen to be tested with the proton beam at Arronax or iThemba labs in the future.